CZECH TECHNICAL UNIVERSITY IN PRAGUE

Faculty of Nuclear Sciences and Physical Engineering

Department of Physics
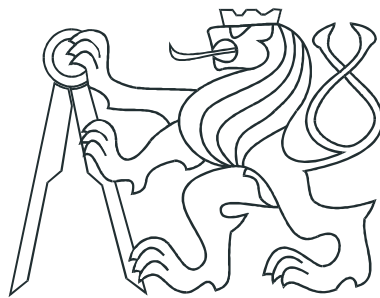
Diploma thesis

Non-identical kaon femtoscopy at STAR experiment

Jindřich Lidrych

Supervisor: RNDr. Petr Chaloupka, Ph.D.

Prague, 2016

ČESKÉ VYSOKÉ UČENÍ TECHNICKÉ V PRAZE

Fakulta jaderná a fyzikálně inženýrská

Katedra fyziky
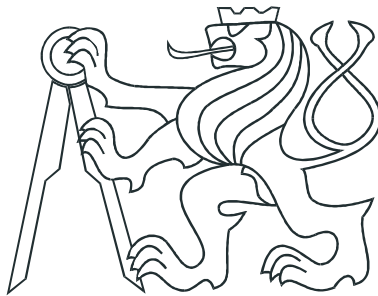
Diplomová práce

Femtoskopie neidentických kaonů na experimentu STAR

Jindřich Lidrych

Vedoucí práce: RNDr. Petr Chaloupka, Ph.D.

Praha, 2016

Prohlášení:

Prohlašuji, že jsem svoji diplomovou práci vypracoval samostatně a použil jsem pouze podklady (literaturu, software, atd.) uvedené v přiloženém seznamu.

Nemám závažný duvod proti užití tohoto školního díla ve smyslu 60 Zákona .121/2000 Sb., o právu autorském, o právech souvisejících s právem autorským a o změně některých zákonu (autorský zákon).

V Praze dne 6. května 2016

Jindřich Lidrych

Title:

Non-identical kaon femtoscopy at STAR experiment

Author: Jindřich Lidrych

Specialization: Experimental nuclear and particle physics

Sort of project: Diploma thesis

Supervisor: RNDr. Petr Chaloupka, Ph.D.

Abstract: Femtoscopic measurements of two-particle correlations at small relative momenta provide means to study space-time extents of the system created in high-energy heavy-ion collisions. The correlations result from quantum statistics and from interaction in the final state (Coulomb and strong). The strenght of the correlation depends on the size of the particle-emitting region. It has been predicted that correlations due to the strong final-state interaction in a system with a narrow near-threshold resonance will be especially sensitive to the source size in the region of the resonance. Pair of unlike-sign kaons are ideally suited for such a measurement, since the system contains a narrow $\phi(1020)$ resonance. This work presents first systematic study of unlike-sign kaon correlation function, including the region of the resonance, using STAR data from Au+Au collisions at $\sqrt{s_{\mathrm{NN}}} = 200$ GeV. The experimental results are compared to a theoretical calculations which include the treatment of resonance formation due to the final-state interaction. Additional insight in to the interpretation of results is provided by a comparison with predictions from hydrodynamic-based models.

Key words: Correlation femtoscopy, unlike-sign kaon correlation function, STAR experiment, blast-wave model.

Název práce:

Femtoskopie neidentických kaonů na experimentu STAR

Autor: Jindřich Lidrych

Abstrakt: Femtoskopická měření dvoučásticových korelací v oblasti malých relativních hybností umožňují studium časoprostorových rozměrů systému vytvořeného při vysokoenergetických srážkách těžkých iontů. Korelace jsou výsledkem kvantové statistiky a interakce částic v koncovém stavu (Coulombická a silná interakce). Síla korelace je úměrná velikosti oblasti, ze které byl daný pár částic emitován.

Bylo předpovězeno, že v systému s resonancí, která se nachází blízko kinetického prahu, budou korelace způsobené silnou interakcí působící skrz resonanci obzvláště citlivé na velikosti zdroje právě v této oblasti. Vzhledem k tomu, že systém neidentických kaonů obsahuje $\phi(1020)$ resonanci, jsou páry kaonů vhodnými kandidáty pro tato měření.

V této práci je představena první systematická studie korelačních funkcí neidentických kaonů, které obsahují oblast resonance. Pro měření byla použita data ze srážek Au+Au při $\sqrt{s_{\mathrm{NN}}}$=200 GeV na experimentu STAR. Výsledky jsou porovnány s teoretickými výpočty obsahující $\phi(1020)$ resonanci díky interakci v koncovém stavu. Výpočty založené na hydrodynamických modelech poskytují detailnější pohled na interpretaci výsledků.

Klíčová slova: Korelační femtoskopie, korelační funkce neidentických kaonů, STAR experiment, blast-wave model.

Acknowledgement

Contents

Preface

Ultrarelativistic heavy-ion collisions provide means to study properties of nuclear matter under extreme conditions. It is expected that a new state of nuclear matter called Quark-gluon plasma is created in the initial stages of the collisions. However this system exists only for a very brief period of time with typical space-time extents on the order of 10^{-14} m. Femtoscopic measurements of two-particle correlations at small relative momenta reveal information about the space-time characteristics of the system at the moment of particle emission.

It has been predicted that correlation due to the strong final state interaction in a system where a narrow, near threshold, resonance is present will be sensitive, in the region of the resonance, to the source size and momentum-space correlations. Such measurements can provide complementary information to the measurements at very low relative momenta. This thesis introduces femtoscopic analysis of unlike-sign kaon correlations in Au+Au collisions from STAR experiment at a center-of-mass energy of 200 GeV. The system of non-identical kaon is of interest since it contains $\phi(1020)$ resonance.

A brief introduction in the physics of heavy-ion collisions is given in Chapter 1. The observables related to the formation of the Quark-gluon Plasma are discussed in the context of recent experimental results from the STAR experiment. Chapter 2 introduces the STAR detector, one of the experiments at RHIC.

Theoretical backgrounds of femtoscopic measurements are discussed in Chapter 3. The derivation of the two-particle correlation function as well as construction of th experimental correlation function is shown. Then the extraction of space-time extents from the experimental correlation function together with model treatment of space-time evolution of the considered system is present. Experimental results from systematic femtoscopic measurements are briefly discussed.

The rest of the thesis is dedicated to my own femtoscopic analysis of unlike-sign kaon correlations. While the used data set and applied selection criteria for construction of correlation functions are discussed in Chapter 4. The most important corrections applied in the presented analysis are introduced in Chapter 5. Here the correction for misidentification of particles and momentum resolution have been used. In order to compare the experimental unlike-sign correlation functions to model predictions, the space-time extents of the source were extracted from like-sign one-dimensional as well as three-dimensional correlation functions. The measured HBT radii and kaon spectra were fitted by blastwave model obtaining parameters which describe the kaon source at the freeze-out. This parametrization of the source was afterwards used for calculation of the theoretical correlation function by theoretical model that includes the treatment of the resonance formation due to the final-state interaction. The measured unlike-sign correlation functions were also compare to hydrodynamic model predictions, namely to HYDJET++ and THERMINATOR 2. Such model comparison provides additional insight into the interpretation of the results. Finally, the obtained results are summarized in the last chapter of this thesis.

CHAPTER
ONE

HEAVY-ION COLLISIONS AND QUARK-GLUON PLASMA

Experiments with high-energy heavy-ion collisions provide means to study properties of nuclear matter under the extreme conditions and its transition from hadrons to a state of deconfined quarks and gluons called the Quark-gluon plasma. This chapter introduces a brief overview of the particle physics focusing mainly on heavy-ion collisions which are a promising tool for the creation of the Quark-gluon plasma.

1.1 Standard Model

The Standard Model (SM) [1] is a quantum field theory classifying all known particles and summarizing their interaction.

1.1.1 Fundamental particles

There are three classes of elementary particles in the SM. The group of particles, which have a spin of $1/2$ and respect the Pauli exclusion principle, are noted as fermions. According to the their interaction, the fermions can be further divided into two groups - quarks and leptons. There are six quarks and six leptons.

The quarks are distinguished according their flavor as up (u), down (d), strange (s), c (charm), b (bottom) and top (t) and can be grouped into 3 generations. Each quark carries a fraction of the elementary charge, specifically $Q = 2/3$ or $Q = -1/3$ and one of the three colors: red, green or blue. In nature the quarks have never been observed individually, but only inside bounded colorless strongly interacting particles called hadrons. The hadrons consisting of a quark-antiquark are mesons and baryons are the bounded states of three quarks. The latest experimental results from the Large Hadron Collider (LHC) and the Fermilab Tevatron collider indicate existence of pentaquark [2], bounded state of four quarks and one antiquark and the tetraquark, hadronic state with valence quarks of four different flavors [3], respectively.

The leptons form, similarly as the quarks, 3 generations. Each generation consists of lepton and its corresponding neutrino, i.e. electron (e^-), electron neutrino (ν_e), mion (μ), mion neutrino(ν_μ), tau (τ) and tau neutrino (ν_τ). Each quark and lepton have a corresponding antiparticle, the particle with the same mass and opposite charge.

Another class of elementary particles contains gauge bosons, namely gluon (g), photon (γ), Z boson (Z) and W boson ($W^\pm$). These vector particles with a spin of 1 are mediators of the fundamental interactions. The massive electrically neutral Z boson and electrically charged $W^\pm$ bosons mediate the weak interaction, while the massless electrically neutral photon is associated with the electromagnetic interaction. The gluons carrying the color charge are mediators of the strong interaction.

The last fundamental particle which remains is a recently discovered Higgs boson H [4], [5]. This scalar particle gives mass to other fundamental particles.

Figure 1.1 shows the overview of all previously discussed fundamental particles and their properties.
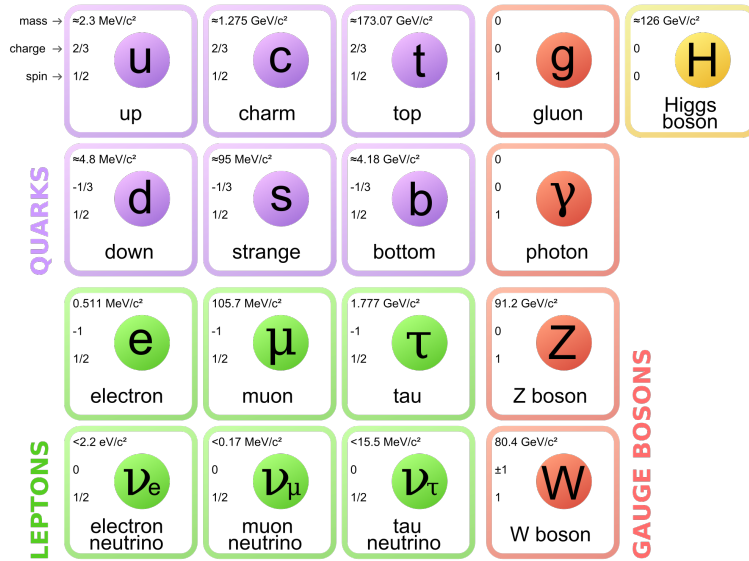
Figure 1.1: Fundamental particles in the Standard model and their properties. Taken from [6].

1.1.2 Fundamental interaction

The SM contains three fundamental interactions, namely strong, weak and electromagnetic. Each of these interactions is characterized by the corresponding gauge theory with a symmetry group and can be explained as exchange of mediators, the already discussed gauge bosons. Table 6.1 shows the summary of the fundamental interactions, their mediators, the range and the relative force with respect to the strong interaction.

Interaction	Mediator	Range	Relative force
electromagnetic	photon	$+\infty$	10^{-2}
weak	$W^\pm$ and Z bosons	10^{-18}m	10^{-7}
strong	gluon	10^{-10}m	1

Table 1.1: Fundamental interactions in the Standard model and their properties.

The mediator of the electromagnetic interaction is the photon and this interaction is described by the Quantum Electrodynamics. Since the photon has zero mass, the range of this force is infinity. On

the other hand, the weak interaction is mediated by the massive $W^{\pm}$ and Z bosons, and therefore the the range of this force is very short. These two forces can be united into the electroweak interaction. The mass difference of their mediators is caused by the spontaneous symmetry breaking, O(4)$\rightarrow$ U(2)$\times$U(1), when Z and $W^{\pm}$ bosons obtain masses by the interaction with the Higgs boson.

The last fundamental force, which is contained in the SM, is the strong interaction with gluons as the mediators. Although the gluons are also massless particles like the photons, the strong interaction can reach up only units of fermi - 10^{-15} m. This behavior is quite interesting and can be explained by the Quantum Chromodynamics (QCD), which will be discussed in detail in the following section.

Although the SM does not contain the gravitation force and its mediator, the graviton, and can not give an explanation of some phenomena, such as the non-zero mass of neutrino, it is one of the most widely accepted theoretical models in the particle physics.

1.2   Quantum Chromodynamics

The QCD is the gauge theory describing the strong interaction with the corresponding SU(3) symmetry group. The mediators of this force are the massless gluons that carry color charge. As already said, the corresponding symmetry group for the QCD is SU(3) with eight generators, hence there are eight different gluons. Unlike photons, gluons can interact among themselves. Such a property of gluons leads to interesting behavior of the strong interaction.

1.2.1   Asymptotic freedom

The running coupling constant α_s describes the strength of the force between quarks. David Gross, David Politzer and Frank Wilczek predicted in 1973 [7] that the α_s depends on the four momentum transfer q and changes like [7]

$$\alpha_s(q) \sim \frac{1}{\ln \frac{q^2}{\Lambda_{QCD}^2}},\tag{1.1}$$

where the Λ_{QCD} is a constant introduced by the renormalization process and is approximately equal to 200 MeV. The left panel of Figure 1.2 shows overview of measurements of the running coupling constant α_s as a function of q from electron-positron, electron-proton, and proton–(anti)proton collider experiments [8]. The four momentum transfer q is inversely proportional to distance r and therefore at very short distances r and at large transverse momentum q respectively, the coupling constant decreases and it leads to weakened of the strength of the interaction. For a sufficiently very small α_s, quarks start to behave almost as the free particles. This phenomenon is known as asymptotic freedom [7]. In such region of value of q the perturbative QCD (pQCD) calculation can be used.

1.2.2   Color confinement

While in the previous case, for short distance the QCD predicts asymptotic freedom, in normal conditions the strength of the strong interaction is so high that quarks and antiquarks are bound in colorless strongly-interacting objects. The effective quark-antiquark potential is described by [10]

$$V(r) = -\frac{\alpha_s}{r} + kr,\tag{1.2}$$

where α_s is the coupling constant, r is the distance between quarks and k is the string tensor representing the strength of the quark confinement force. As can be seen, the potential has two parts. The
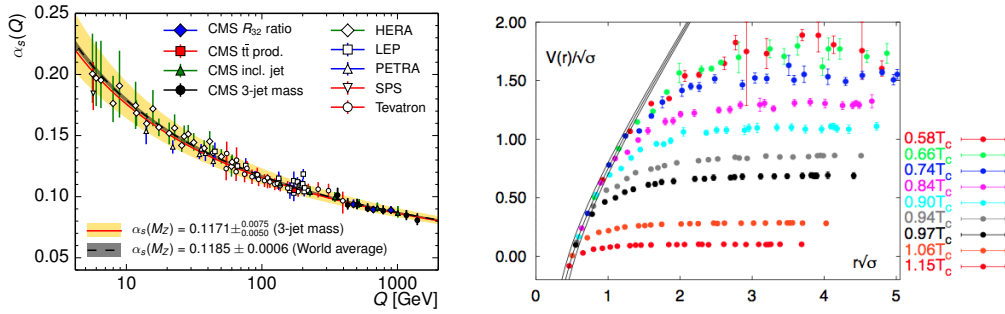
Figure 1.2: Left: The overview of measurements of the running coupling constant α_s as a function of transverse momentum q. Taken from [8]. Right: Temperature dependence of quark-antiquatk potential scaled by the string tensor $\sqrt{\sigma}$. Taken from [9].

first part evokes the well-known Coulomb potential depending on $1/r$. The second part is a string potential and it can explain the fact that quarks are never seen in isolation under normal conditions, but only bound with hadrons. The right panel of Figure 1.3 shows the comparison of the potential between a quark and an antiquark as a function of their distance and the Coulomb potential. While the Coulomb potential is almost constant for the large distance r and can be neglected, thanks to the linear term kr, the potential energy between a quark and an antiquark increases linearly until the moment, when the energy is so high that the pair of quark-antiquark is created from vacuum. Immediately they are bound together with previous quark and antiquark. Thus finally there are two quark-antiquark pairs. This feature is shown schematically in the right panel of Figure 1.3.
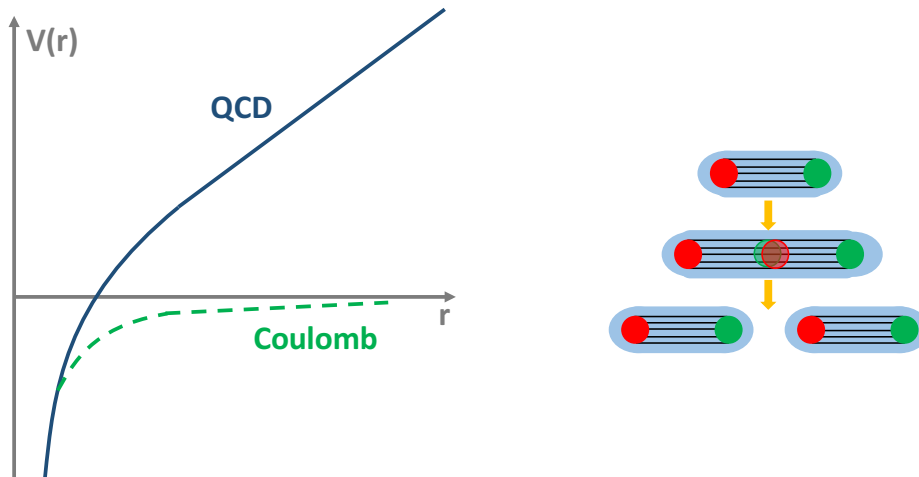
Figure 1.3: Left: The comparison of potential between a quark and an antiquark as a function of their distance (blue line) and Coulomb potential (green line). Right: Illustration of color confinement. Red and green cycle represent a quark and an antiquark, respectively.

1.3 Quark-gluon plasma

Based on the asymptotic freedom, the QCD predicts a phase transition from a confined matter into a new state of matter, in which the quarks and gluons are deconfined. This novel state of nuclear matter is the so-called Quark-gluon plasma (QGP) [10]. There are two possible methods, how it can be formed - by high temperature T or by high baryon chemical potential μ_B corresponding a net baryon density.

With increasing temperature, the system can reach up the certain values of energy density ϵ, when the hadronic matter dissociate and the QGP is established. This fact is also predicted by the calculation of the lattice QCD as shown in Figure 1.2. The effective quark-antiquark potential changes with increasing temperature and in the vicinity the critical temperature the linear term in the potential, which is responsible for confinement of quarks in hadrons, vanished. The temperature of the systems that is related to this phase transition is referred as a critical temperature T_c.

Earlier theoretical calculation based on thermodynamic and hydrodynamics predicted the initial energy density $\epsilon \approx 1 - 10$ GeV/fm^3 [11] and that any phase transition will take place for the temperature around the $T \approx 150 - 200$ MeV [11]. These values were put more precisely by the lattice QCD and nowadays it is expected for the critical temperature to be around the $T_c \approx 170$ MeV.

The other possibility how the QGP can be established is during the adiabatic compression of nuclear matter at the temperature $T \approx 0$ MeV. Since it is believed that the system can reach such a high baryon chemical density μ_B, where the binding between the quarks will be broken up and the QGP will be formed.

It is expected that in early Universe, a few microseconds after the Big Bang, the temperature and the density of matter were so high, that the QGP was formed. Nowadays these extreme conditions allowing the formation of the QGP are very hard to find in nature, but there are still places, where the QGP should exist. One of these places is the center of the neutron and compact stars. However more suitable tool for studying the properties of the QGP are the ultra relativistic heavy-ion collisions. Here it is expected that the QGP is early of the collisions.

1.3.1 Phase diagram of hadronic matter

The schematic drawing of the phase diagram of the QCD matter is presented in Figure 1.4 in the plane of temperature T and the baryon chemical potential μ_B.

At moderate temperature and baryon chemical potential μ_B, the quarks are confined in hadrons. At very high temperature, the mesons and the baryons "melt" and hadron matter undergoes phase transition into the QGP. The actual type of the phase transition depends on where we are in the phase diagram.

Both the temperature T and the baryon chemical potential μ_B vary as function of the collision energy $\sqrt{s_{NN}}$ and therefore experimentally different regions of the phase diagram can be accessed by changing the beam energy. This is the strategy adopted in the Beam Energy Scan (BES) [13] program at the Relativistic Heavy Ion Collider (RHIC) where scan with Au+Au collisions over beam energy in range of $7.7 \leq \sqrt{s_{NN}} \leq 200$ GeV was employed in 2010, 2011 and 2014. Table 1.2 shows the overview of the RHIC BES energies with corresponding T and μ_B. The lowest energies, specifically 3.0, 3.5 and 3.9 GeV were obtained from the beam and beam-pipe collisions during the RHIC BES run. This data set was extended by the 3.9 GeV collisions from the STAR Fixed Experiment performed in 2014 when the the gold target was inserted into the beam pipe during the 14.5 GeV run.
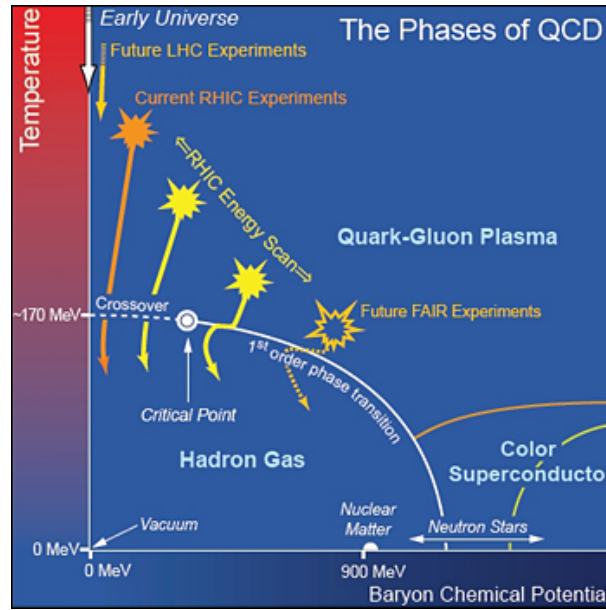
Figure 1.4: Phase diagram of QCD with boundaries that define various state of QCD matter. Taken from [12].

The purpose of the RHIC BES program is to search for threshold energies for the QGP formation, since it is known that the QGP is already well established at the top RHIC energy - 200 GeV. Another main goal is to investigate signatures of the order phase transition and to find the critical point.

$\sqrt{s_{\mathrm{NN}}}$ [GeV]	μ [MeV]	T [MeV]	$\sqrt{s_{\mathrm{NN}}}$ [GeV]	μ [MeV]	T[MeV]
200.0	24	165.9	11.5	316	151.6
130.0	36	165.8	7.7	422	139.6
62.4	73	165.3	4.9	562	118
39.0	112	164.2	4.5	589	111
27.0	156	162.6	3.9	633	101
19.6	206	160.0	3.5	666	93
14.5	262	156.2	3.0	721	76

Table 1.2: BES energies and corresponding temperature and baryon chemical potential. Taken from [13].

1.4   Heavy-ion Collisions

In this section, heavy-ion collisions will be introduced since it is the only way how to create and study the QGP in the laboratory. In ultrarelativistic heavy-ion colliders, two nuclei are accelerated to speed close to that of light. Therefore these nuclei are Lorentz contracted in the direction of their motion and the thickness of them is $2R/\gamma$, where R is the radius of nucleus and γ is the Lorentz factor as is shown in Figure 1.5.

1.4.1 Geometry of heavy-ion collision

The dynamic properties of the created system are strongly affected by the initial geometry of the colliding nuclei. The most important variable characterizing the collisions is the centrality, which is defined [14] as

$$c = \frac{\int_0^b \frac{d\sigma}{db'} db'}{\int_0^\infty \frac{d\sigma}{db'} db'} = \frac{1}{\sigma_{AA}} \int_0^b \frac{d\sigma}{db'} db', \tag{1.3}$$

where σ_{AA} is the nucleus-nucleus cross-section and the b is the impact parameter.

The impact parameter b indicates the distance of the centers of two nuclei in the transverse plane during the collisions. If $b \approx 0$, the collisions are head on and all nucleons participate in the collision. While for $0 < b < 2R$ the peripheral collisions take place. In this case, the number of participant of the collision, which consequently create a new system is equal to $N_{part} = 2A - N_{spec}$, where A is the total number of nucleons in the nucleus and N_{spec} is the number of nucleons, which do not participate in the collision. These nucleons are noted as the spectators. The extreme case of collision is for $b > 2R$, when two colliding nuclei do not overlapped and interact just via electromagnetic force. These collisions are called as ultra-peripheral.

Figure 1.5 schematically describes heavy-ion collisions, where the participants are colored by yellow, while the blue nucleons are the spectators. As can be seen, the volume of overlapped region depends on the number of participants and spectators, respectively.
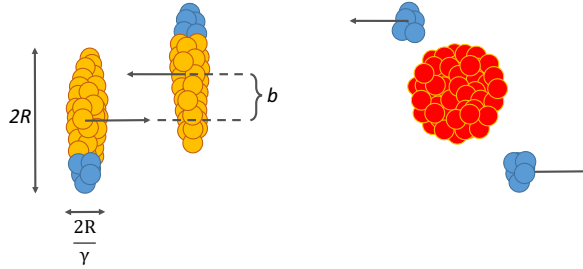
Figure 1.5: High-energy collisions of two Lorentz contracted nuclei with the impact parameter b. The participants are colored by yellow and non-interacting spectators are blue.

The impact parameter b can not be directly measured and the experimental observables related to the centrality are the multiplicity of the charged particle and the energy carried by the spectators, that are detected by the zero degree calorimeters. To obtain information about the geometry of the collisions such as the impact parameter and the centrality, the Monte Carlo simulators have to be employed. One of the widely used Monte Carlo simulator for determination of the geometry of the collisions is the Glauber model [15] which works on a simple principle - decomposition of the collisions of two nuclei into many nucleus-nucleus collisions.

1.4.2 Space-time evolution of the collision

Figure 1.6 illustrates the heavy-ion collisions and different moments of the space-time evolution of the created system. The Lorentz contracted nuclei collide and the pre-equilibrium stage starts [10].

During this phase, the nucleons of incoming nuclei scatter several times and loose part of their energy. Quarks and gluons are created from the vacuum excitation. After a very short time, $t \leq 1\text{fm}/c$,
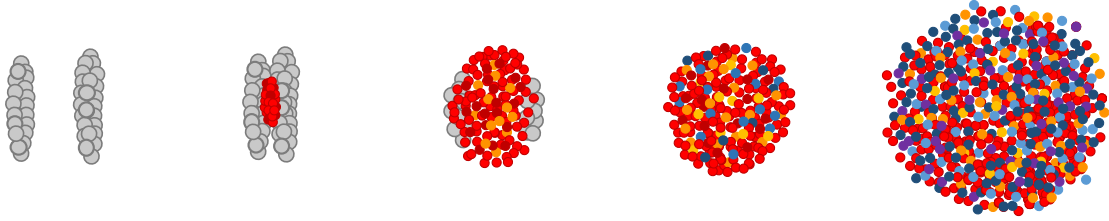
Figure 1.6: Schematic diagram of the space-time evolution of the heavy-ion collision.

the system reaches thermal equilibrium by the re-scattering of the quarks and the gluons. In case that the collision energy $\sqrt{s_{NN}}$ was sufficiently high, the quarks and gluon are liberated and QGP is established [10].

Since then the created system starts to behave collectively and can be described by the hydrodynamics. This behavior depends on collision energy $\sqrt{s_{NN}}$ and with increasing energy, the properties of the formed medium look more and more like the behavior of the perfect liquid.

While the system expands, it cools down until the moment, when it undergoes the phase transition from the de-confined stage of matter to hadrons. The temperature of such a system is now around the critical temperature T_c [16]. At this temperature, the quarks and the gluons can not exist as the free particle anymore and start to return in the confined phase of hadronic matter. This moment of the space-time evolution is called the hadronization and takes place $t \approx 5\mathrm{fm}/c$ [17] after the heavy-ion collisions.

The expansion and cooling down of the system continue, but the temperature is still so high, that the hadron species can change by the inelastic collisions. The system further cools until it reaches the chemical freeze-out ($t \approx 10\mathrm{fm}/c$) [17], the number of hadrons is fixed. After the chemical freeze-out, the particles interact only elastic until the thermal freeze-out, when the emission of the particle starts.

As can be seen, the created system exists for a very short time to our time-scale. However in comparison to typical physical process of the strong interaction it is long-lived system. The information about the space-time evolution of the system can be inferred only from the measured particles, which fly out from the system and are measured by the detector.

The above mentioned time and temperature can be extracted from the hydrodynamic and the statistical model, which are able to describe the particle spectra and ratio.

1.5   Signatures of the Quark-gluon plasma

As already said, the heavy-ion collisions are a promising tool for creation of the QGP. The ultra-relativistic heavy ion collisions and their evolution are dynamic processes with typical space-time extends of order tens fm and the QGP exists in the initial stages of the collisions for a very short time. Therefore, the QGP cannot be studied directly, but only via so-called the QGP signatures. In the following subsections, the QGP signatures and their relation to results from BES [13], [18] will be discussed.

1.5.1 Jet quenching

One of the most promising QGP signatures is the phenomenon known as the jet quenching. In heavy ion collisions, partons with the large transverse momentum p_T are created in the hard scattering of nucleons constituents in the initial stage of the collisions. These high momentum partons traverse through a dense hot medium formed in heavy-ion collision and because of that they start to loose energy and can be absorbed. The energy loss should be proportional to the initial gluon density and the lifetime of the system. To quantify the high-p_T suppression, a comparison of the particle yields in central $\mathrm{d}^3 N_{AA}^{cen}/\mathrm{d}\eta\mathrm{d}^2 p_T$ and peripheral $\mathrm{d}^3 N_{AA}^{peri}/\mathrm{d}\eta\mathrm{d}^2 p_T$ collisions presented in terms of a nuclear modification factor, which is defined as

$$R_{CP} = \frac{\left\langle N_{bin}^{peri}\right\rangle \mathrm{d}^3 N_{AA}^{cen}/\mathrm{d}\eta\mathrm{d}^2 p_T}{\langle N_{bin}^{cen}\rangle \mathrm{d}^3 N_{AA}^{peri}/\mathrm{d}\eta\mathrm{d}^2 p_T} \tag{1.4}$$

is done. The number of hard processes should rise linearly with the number of binary collisions $\langle N_{bin}\rangle$. Hence each particle yield is scaled by corresponding number of collision. More precise comparison can be done when the particle yields in peripheral collisions in denominator are replaced by the particle yields from proton+proton collisions. In such cases the R_{AA} is constructed. The importance of such a comparison when the R_{AA} factor is constructed arising from the presence of the cold nuclear effects that can still play crucial role in the peripheral collisions. However reference proton+proton collisions for corresponding BES energies are not available, thus the R_{CP} was studied.

Figure 1.7 shows the nuclear modification factor for charged hadrons for different BES energies [19]. As can be seen, while at high beam energies the strong suppression is observed, at low beam energies the situation is opposite and the strong enhancement exhibits. The suppression of high-p_T partons can be interpreted by the presence of the QGP. On the other hand, the measured enhancement at low beam energies has ambiguous explanations and the origin of the enhancement can be Cronin effect [20], cold matter effects and/or strong radial flow [13].
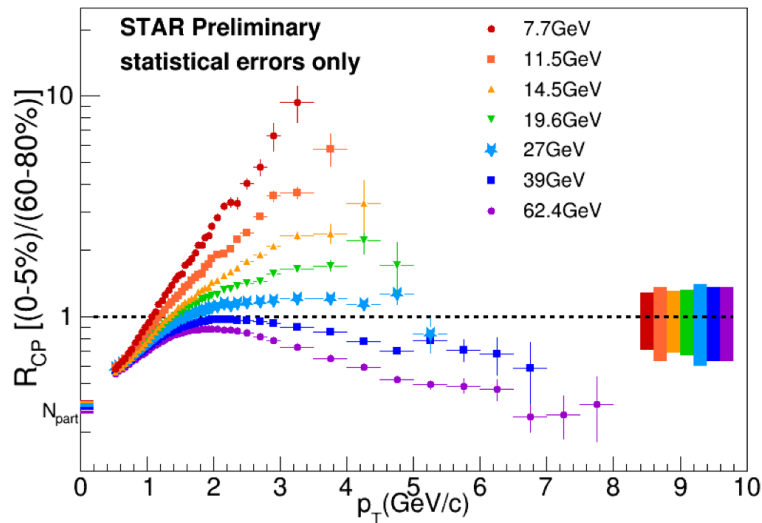
Figure 1.7: Charged hadron R_{CP} for RHIC BES energies. Taken from [19].

1.5.2   Strangeness enhancement

In elementary particle collisions, the effect of associated production of the hadrons containing strange quark is suppressed due to relatively high mass of the strange quark. In case that the QGP is formed, the pairs of strange and anti-strange quarks may be also produced the gluon fusion, since the threshold for such a reaction is about 200 MeV and the strangeness enhancement should be observed [10]. Therefore, the important QGP signatures are the particle yields and ratio of strange mesons and baryons at different beam energies. The particle yield at chemical freeze-out T_{ch} can be calculated by the statistical model and the number of particle species N_i in a system of volume V is given by following formula [10]

$$N_i/V = \frac{g_i}{(2\pi)^3}\gamma_S^{S_i}\int\frac{1}{\exp\left(\frac{E_i - \mu_B B_i - \mu_S S_i}{T_{ch}}\right)\pm 1}\mathrm{d}^3p, \tag{1.5}$$

where g_i is the spin degeneracy, B_i is the baryon number, S_i is the strangeness number, E_i is the particle energy, μ_B is the baryon chemical potential, μ_S is the strangeness chemical potantial and γ_S is the strangeness suppression factor. The values of T_{ch} and μ_B can be obtained from the experimentally measured particle yields.

The previous theoretical prediction will be now compared with results on ϕ mesons which is of particular interest for this work. The $\phi(1020)$ consists of pair of the strange and anti-strange quarks. Figure 1.8 shows results [21] on the ϕ meson yield per number of participants as a function of the number of participants N_{part} for 5 different collisions system and the ϕ/π^- ratio also for five different collisions energies. Both results exhibit energy and system size dependence. As can be seen, the ϕ yields increase slightly with collision energy for the same N_{part}. The yield ratio ϕ/π^- also rises with the collision energy in $Au + Au$ collisions and $p + p$ collisions. These results show that the yield of the ϕ mesons increases faster than the yield of the π^- mesons. The measured enhanced production of the ϕ meson in heavy-ion collision can indicate the QGP formation.
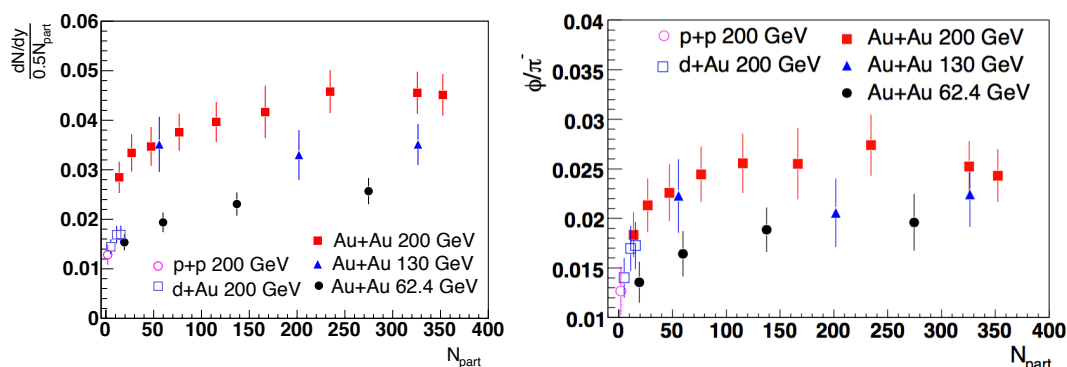
Figure 1.8: L: The ϕ meson yield per number of participants as a function of the number of participant N_{part} for 5 different collisions systems. R: the ϕ/π^- ratio for five different collisions energies as a function of the number of participants. Taken from [21].

1.5.3 Elliptic flow

Another QGP signature which will be discussed is the elliptic flow [22]. In non-central collisions, the formed system has asymmetric shape elongated in the out-of-plane direction. As demonstrated by the hydrodynamic calculations, if the system thermalizes quickly, the initial spatial anisotropy and interactions among the constituent result in pressure gradients that are larger in the direction of the reaction plane. This leads to subgradient expansion and results in the elliptical azimuthal particle distribution. Since the pressure gradient is related to the equation of state (EoS), the elliptic flow can provide information about the QGP pressure in the early state.

Experimentally, the elliptic flow can be obtained from the Fourier expansion of the azimuthal distribution of particle, which is expressed by

$$E\frac{d^3N}{d^3p} = \frac{d^2N}{2\pi p_T dp_T dy}\left(1 + \sum_{n=1}^{\infty} 2v_n \cos\left[n\left(\phi - \Phi_r\right)\right]\right),$$ (1.6)

where ϕ is the azimuthal angle of the particle and the Φ_r is the azimuthal angle of the reaction plane in the laboratory frame. The coefficients v_i in the Fourier expansion are related to flow. While the first coefficient, v_1 is called the direct flow and quantifies the strength of direct flow, the second coefficient, v_2 is the already discussed the elliptic flow.

Systematic study of v_2 of hadrons as the function of the transverse mass for 6 different BES energies are presented on Figure 1.9. This measurement was performed for the most abundant hadrons like pions and kaons as well as for the multi-strange particles like ϕ ($s\bar{s}$), Ω^- (sss) and Ξ^- (dss).
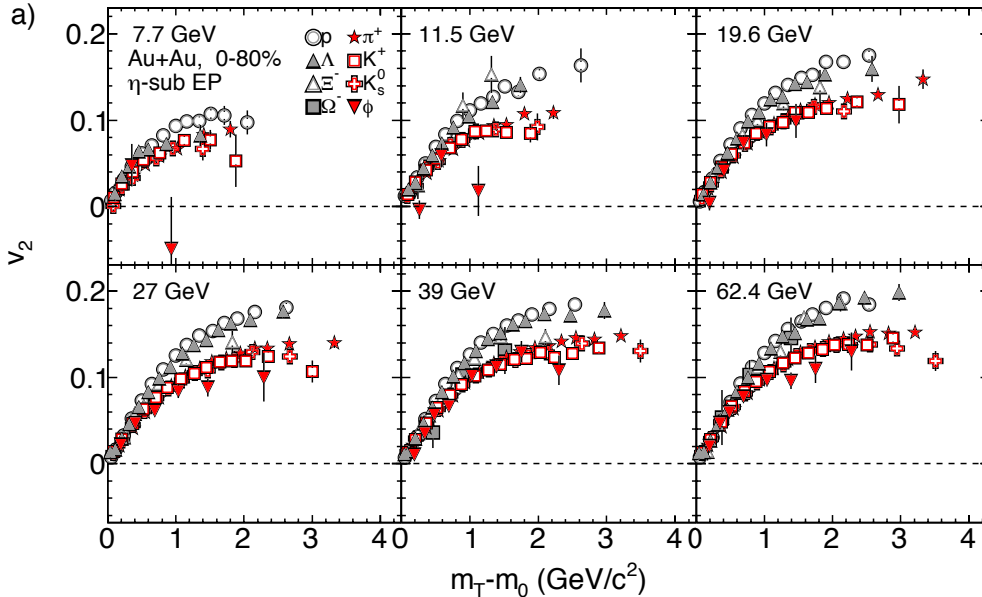
Figure 1.9: The results of the identified hadron elliptic flow from BES energies. Taken from [23].

Figure 1.9 shows that the v_2 coefficients are ordered according to hadron mass. The lighter hadrons have a larger v_2 in comparison to heavier hadrons. While for the low p_T, the values of v_2 of hadrons are almost the same, for the values above $p_T \approx 2$ GeV/c significant difference in v_2 of lighter mesons and

baryons can be observed. Such characteristic baryon-meson splitting is explained by a hadronization via recombination and it is connected to the existence of partonic collectivity and the formation of the QGP.

There are a lot of other signatures, which serve as a probe for the formation of QGP in ultra-relativistic heavy-ion collisions. These signatures will not be discussed in more detail, but some of them are listed in following summary [10] [24].

- Space-time characteristic of the system at the kinetic freeze-out measured by the two-particle correlation

- Quarkonia (J/ψ, Υ and their excited states) suppresion due to the Debye screening in the QGP [25]

- Enhanced production of anti-particle in the QGP

- Enhancement of direct photons and dileptons due to the QGP thermal radiation

As can be seen from the previous discussion, the properties of nuclear matter such as the equation of state, the order of the phase transition, the value of critical temperature etc. are not known well and they are still intensively studied by many experiments focusing on heavy-ion physics.

CHAPTER

TWO

RHIC AND THE STAR EXPERIMENT

In this chapter, the Relativistic Heavy Ion Collider, facility dedicated to the high-energy heavy-ion collisions, is introduced. The STAR detector, one of the experiments at RHIC, will be also described.

2.1 Relativistic Heavy Ion Collider

The Relativistic Heavy Ion Collider (RHIC) located at Brookhaven National Laboratory (BNL) in Upton, New York, is the second most powerful heavy-ion collider in the world. The primary goal of the physics program at RHIC is to produce and to study a deconfined state of nuclear matter, Quark-gluon Plasma by the high-energy heavy-ion collisions.

RHIC has the capability to accelerate a variety of particle species to ultrarelativistic speed and since its commission in 2000 RHIC has successfully collided $Au + Au$, $p + Au$, $d + Au$, $^3He + Au$, $Cu + Au$, $Cu + Cu$, $U + U$, $p + Al$ and $p + p$. In particular, the most important for the study of phase-space diagram of nuclear matter is the RHIC's capability to accelerate to and collide ions at different energies. This has been applied in the RHIC Beam Energy Scan, when scan with Au+Au collisions over beam energy in a range of $7.7 \leq \sqrt{s_{NN}} \leq 200$ GeV was performed in 2010, 2011 and 2014. In addition to the heavy-ion program, RHIC can also collide polarized protons and hence provides opportunity to study the nucleon spin structure.

RHIC consists of two 3.8 km intersecting superconducting storage rings with six interaction points. Nowadays two of them are occupied by the STAR and PHENIX experiments, but in the past, there were also BRAMS [27] and PHOBOS [27] detectors on other interaction points. BRAMS and PHOBOS experiment operated from 2000 and successfully completed their physic programs in 2006 and 2005, respectively.

Protons and heavy-ions can not be injected directly into the RHIC, and therefore they are preaccelerated by the supporting accelerators. The acceleration of proton starts in the linear accelerator (LINAC), where they obtain energy of 200 MeV and then they are sent through the Booster into the Alternating Gradient Synchrotron (AGS). The heavy-nuclei are first of all partially stripped of their electrons and then injected into Booster by the Electron Beam Ion Source (EBIS). The remaining electrons are stripped in Booster and AGS, where the ions or protons are bunched together and consequently they are sent into RHIC with energy of 10 GeV per nucleon. RHIC can be completely filled within one minute. The typical beam in Run11 consisted of 111 bunches and each bunch contained $1.45 \cdot 10^9$ ions [28].
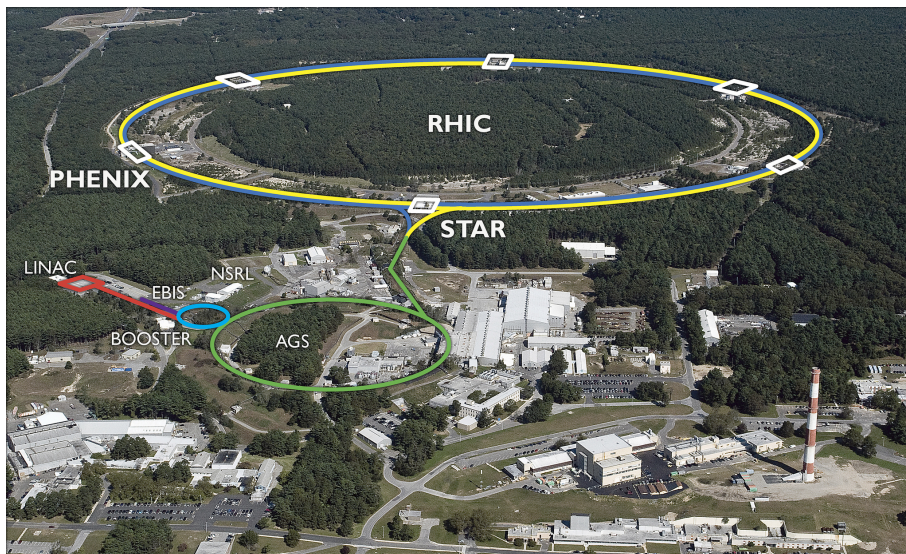
Figure 2.1: The Relativistic Heavy Ion Collider. Taken from [26] .

In RHIC storage rings, two circulating beams are focused and accelerated by the superconducting magnets. When the beams achieve the required energy, they are crossed in the interaction points where collision occurs. The maximum collision energy for heavy-ions is $\sqrt{s_{NN}} = 200$ GeV, while protons are accelerated to $\sqrt{s} = 500$ GeV.

2.2 STAR Experiment

The Solenoidal Tracker at RHIC (STAR) [29] is a multi-purpose detector, which excels in tracking and identification of charged particles at two units of pseudorapidity around mid-rapidity $(-1 < \eta < 1)$ with full coverage in azimuthal angle $(0 < \phi < 2\pi)$. Figure 2.2 shows schematic picture of STAR detector. As can be seen, STAR detector contains various subsystems.

The innermost detector of STAR is the Heavy Flavor Tracker (HFT) [30] installed in 2014. It consists of four layers of silicon detectors divided into three subsystems: a double sided strip detector (SSD) and a silicon pad detector (IST). The last subsystems of HFT are two layers of pixel detectors based on the monolithic active pixel sensors technology (MAPS). It is expected that the HFT will provide excellent primary and secondary vertex position measurements and provide opportunity to measure more precisely the charm mesons like $D^{\pm}, D^0$, etc. [31]

The heart of the STAR detector is the Time Projection Chamber (TPC), which is surrounded by the Time of Flight detector (ToF) and the Barrel Electromagnetic Calorimeter (BEMC). These subdetectors cover full azimuthal angle at mid-rapidity. There are also forward detectors, such as the Beam-Beam Counter (BBC) and the Endcap Electromagnetic Calorimeter (EEMC). The central subsystems sit in the STAR magnet, which has an outer radius of 3.66 m and a length of 6.85 m and is capable to produce a uniform magnetic field of 0.5 T along the beam axis. The Muon Telescope Detector (MTD) is situated around the STAR magnet and covers 45% of azimuthal angle with $(-0.5 < \eta < 0.5)$.

The MTD, the primary Vertex Position Detector (pVDP) and the Zero Degree Calorimeter (ZDC) are located outside of the magnetic field.
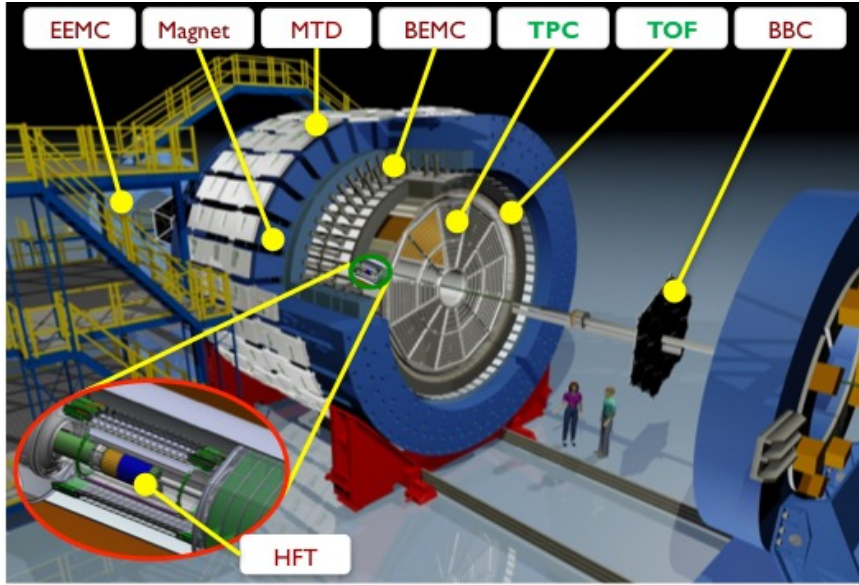
Figure 2.2: The STAR detector. Taken from [26] .

The most important subdetectors for analysis presented in this thesis are the TPC and ToF. The trigger system used for event selection was based on the pVPD and ZDC. These detectors are detailed discussed in the following subsections.

2.2.1   Time Projection Chamber

The TPC, 4.2 m long cylinder with 4 m in diameter, is the primary tracking detector in the STAR. It records tracks, measures momentum and identifies charged particles via the ionization energy loss in full azimuthal angle $0 < \phi < 2\pi$ and it covers pseudorapidity at $-1.8 < \eta < 1.8$.

The schematic picture of the TPC is shown in Figure 2.3. The thin conductive central membrane which is held at a voltage of -28kV separates the east and the west halves of the TPC. In combination with the grounded readout endcap system, there is a well-defined uniform electric field of 135 V/cm, which is required for precise tracking.

The readout endcap system is based on Multi-Wire Proportional Chambers (MWPC) and consists of 12 sectors. Each sector is divided into the inner and outer subsector with 13 and 32 pad rows, respectively. While the outer subsection has continuous pad coverage for better dE/dx resolution and contains in total of 3942 pads with dimensions 6.2×19.5 mm, the inner subsection is designed for precise tracking and consists of 1750 pads with size of 2.85×11.50 mm. The inner subsection has small pads arranged in widely spaced rows, since each pad in row 1 through 8 and in row 8 through 13, respectively is separated by the 48 mm and 52 mm space. The detailed schema can be found in the Figure 2.4, which shows one sector.

The TPC is filled with the P10 gas, a mixture of 10% methane and 90% argon. The pressure of the gas is 2 mbar above the atmospheric pressure and the gas circulates with rate of 36,000 l/h (full volume of the TPC is 50,000 l). Since a stable and fast drift velocity is required, the TPC has to operate on such value of the electric potential where the curve describing dependence of the drift velocity on the electric potential has required properties. In case of the STAR's TPC, it operates on the peak value which is broad, flat and situated at the low electric potential. Such a value makes the
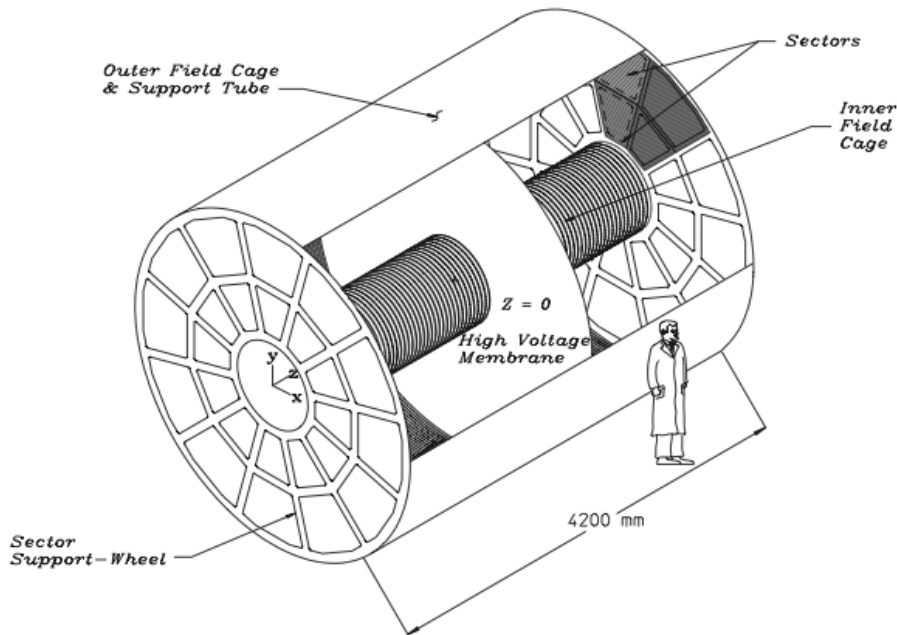
Figure 2.3: The Time Projection Chamber. Taken from [32] .

drift velocity stable and insensitive to small variations in temperature and pressure.

When the charged particles traverse the volume of the gas, they ionize atoms in the P10 gas. The ionization electron drifts towards the endcaps at a constant velocity of ~ 5.45 cm/μs and hence maximum drift time in the TPC is $\sim 40\,\mu$s. The signal from ionization electrons is amplified in front of the anode on the readout endcap system by the electron avalanches. It is created by the high electric field that is at distance of the 20 μm in front of the anode on the readout endcap system and enable to amplify the signal by the factor of 1000-3000. The induced charges from the avalanche are then collected by the several read-on pads.
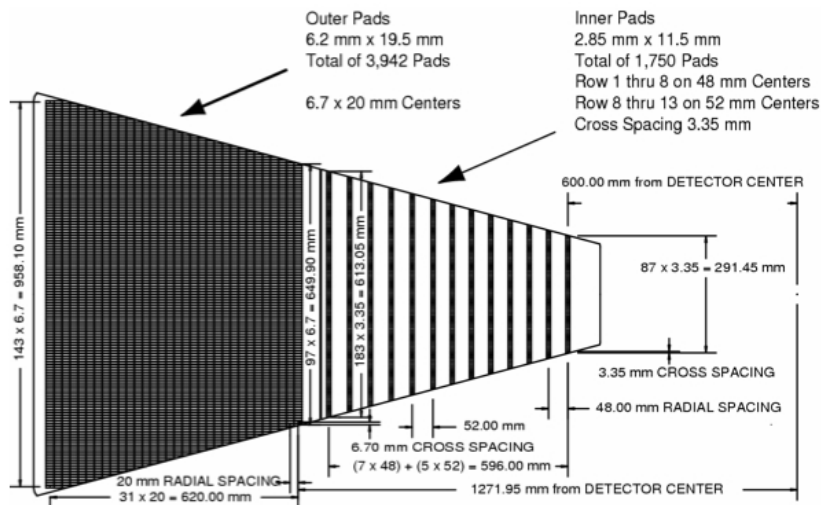
Figure 2.4: A full sector of the anode pad plane from the TPC. Taken from [32] .

Tracking

The position of hits from the pads are used for the tracking. The (x, y) position of the track is determined by the charge measured on the pads, while the z position is obtained by measuring the drift time of ionization electrons relative to the start of the collision divided by the drift velocity, which is very precise measured. To remove uncertainties arising from fluctuations of the value of the drift velocity, the drift velocity is monitored every hour by the laser calibration system [33].

The STAR uses the Kalman filter that starts from the outermost layers of the TPC where hits density is smaller. Figure 2.5 shows a distribution of the last hits of the reconstructed track in the TPC from Au+Au collisions at $\sqrt{s_{NN}} = 200$ GeV.
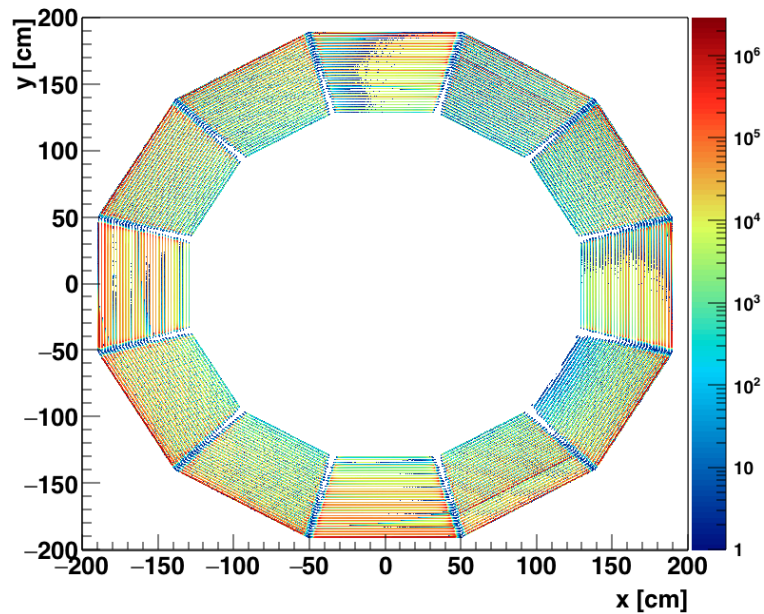
Figure 2.5: The spatial distribution of last hits in the TPC which were used to track reconstruction.

First, the Kalman filter begins with a track seed, which is identified as a collection of a few hits and consequently extrapolates inwards along the approximate direction and curvature. Nearby hits are associated with the track, if they pass the χ^2 test. The tracking algorithm ends, when the innermost layer is reached. In case that the information from the inner tracking system is available, the hits from the TPC are combined with them. Figure 2.7 shows reconstructed Au+Au collisions at $\sqrt{s_{NN}} = 200$ GeV recorded by the STAR detector. The blue lines represent measured tracks by the TPC.

After the initial tracking is completed, the filter refits tracks again and tries to reduce effects of track splitting, track merging and ghost tracks. Newly resulting tracks are denoted as global tracks and determine the vertex primary position. This is done by extrapolating the global tracks to the point with the distance of the closest approach (DCA) to the beam pipe. The tracks with the DCA smaller than 3 cm are connected with the primary vertex and refitted. These tracks are denoted as primary tracks.

Maximum possible number of hits of one track can leave in TPC is 45. However, in practice, this value is smaller, since the maximum of hits depends on the transverse momentum and pseudorapidity of the track as well as on the detector effects. Therefore, for precise tracking reconstruction and
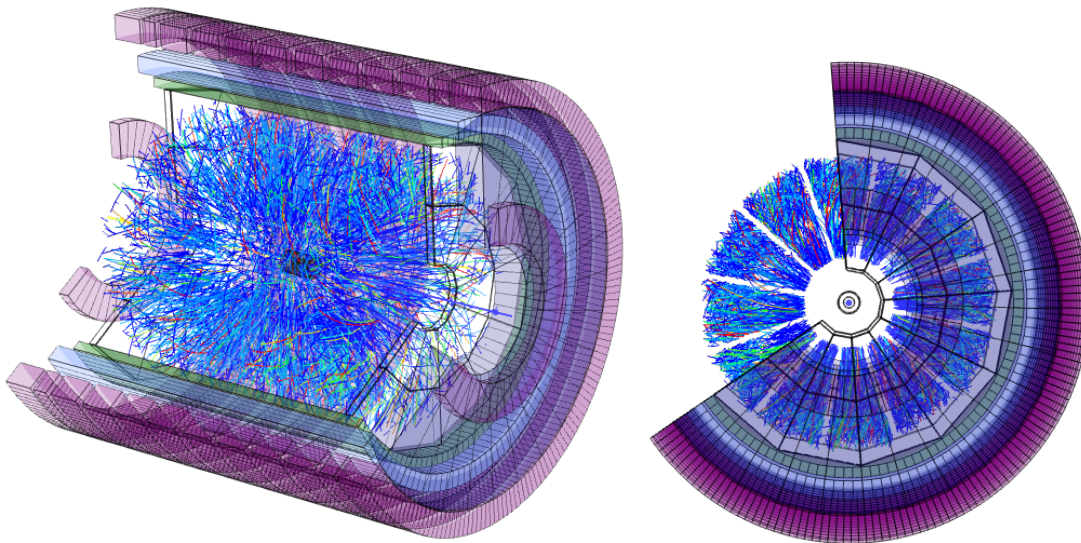
Figure 2.6: The trajectories of particles, which was reconstructed by TPC. Taken from [26] .

relatively high efficiency, tracks with at least 10 hits are required.

The transverse momentum p_T of a track is obtained by fitting a helix through the (x, y) coordinate. In combination with the azimuthal angle φ and the polar angle θ that are determined from track motion with respect to the z-direction, the total momentum can be then calculated.

Particle Identification

The particle identification is based on measurement of the ionization energy loss $\mathrm{d}E/\mathrm{d}x$ determined from the charge collected by the TPC pad rows. The energy loss for charged particles as a function of momentum is shown in Figure 2.9. As can be seen in Figure 2.9, for hadrons the energy loss decreases with increasing momentum until it reaches a minimum and then it starts to slightly increase. The energy loss is also mass ordered i.e. the heavier hadrons lost more energy in comparison to lighter hadrons with the same momentum.

The energy loss of charged particle by ionization is calculated by the Bethe-Bloch formula [34]

$$\left\langle -\frac{\mathrm{d}E}{\mathrm{d}x} \right\rangle = 2\pi N_A r_e^2 mc^2 \rho \frac{Z}{A} \frac{z^2}{\beta^2} \left[\ln\left(\frac{2mc^2\gamma^2\beta^2 W_{MAX}}{I^2} \right) - \beta^2 - \frac{\delta^2}{2} \right], \tag{2.1}$$

where N_A is Avogadro's number, r_e is classical electron radius, m is mass of particle, c is speed of light in vacuum, ρ is density of material, Z and A are atomic number and weight of material, W_{MAX} is maximum energy transfer in a single collision, I is mean excitation energy and δ is density correction. In practice, the Bichsel function [34], which is modified version of the Bethe-Bloch formula and predicts the most probably energy loss, is being used. This function is shown in Figure 2.7, where the expected energy loss for various particle species are represented by the lines of different colors.
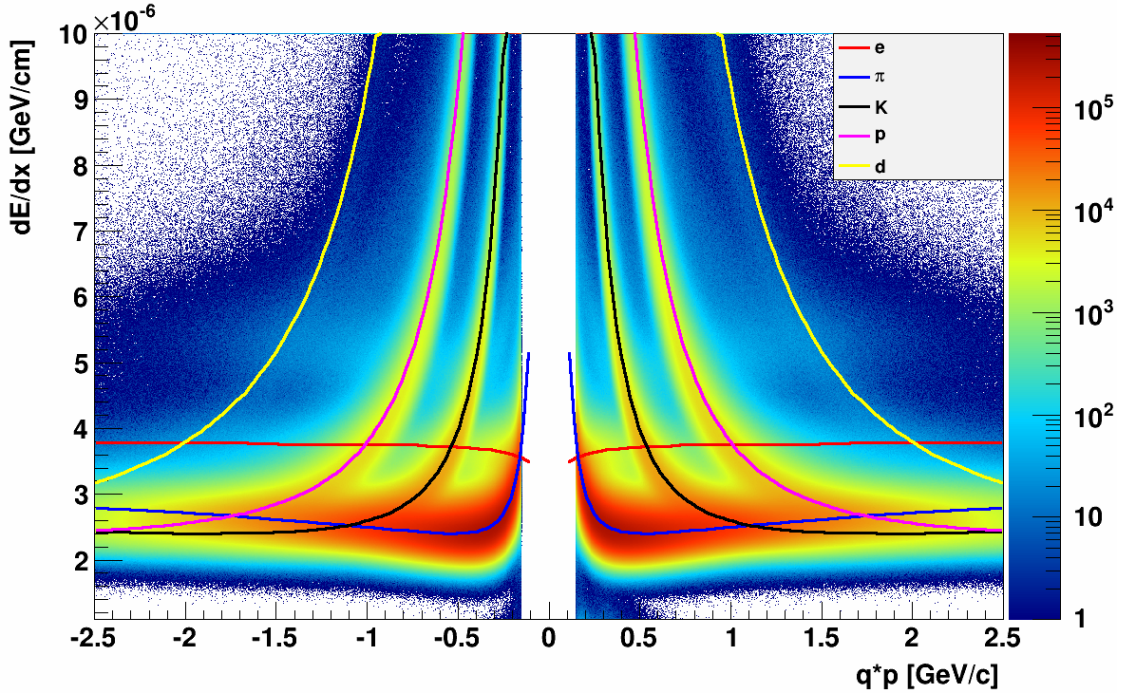
Figure 2.7: The TPC dE/dx versus momentum p and charge q. The colored lines represents the expected value for various particle species from the Bichsel function.

2.2.2 Time of Flight detector

The ToF was developed to improve particle identification and was fully installed in 2010. The detector is based on Multi-gap Resistive Plate Chamber (MRPC) technology. Each tray, which has dimensions of $95 \times 8.5 \times 3.5$ inches, contains 32 MRPC modules and covers 6 degrees in azimuthal angle and one unit in pseudorapidity. In total, the ToF consists of 120 trays that cover full azimuthal angle at $-1 < \eta < 1$. The ToF uses event timing information from the VPD and hit timing in tray to calculate the time of flight for the measured particles.

Particle Identification

Information from TPC and ToF can be combined in order to identify charge particles up to ~ 3 GeV/c momentum. Firstly, only tracks reconstructed in the TPC, have to pass following track quality cut [35]

- $0 < flag < 1000$, where *flag* indicates the fit quality of the track

- number of TPC fit points ≥ 15

- number of TPC fit points / number of possible TPC fit points ≥ 0.52,

to be able to be connected with the hits in the ToF. The information from the ToF is stored in `StMuBTofPidTraits` class containing among others matchFlag function. This function takes four integer values: 0, 1, 2 or 3. If a track is not associated with any hit in the ToF, the matchFlag is equal to 0. While for a track connected with one hit, the matchFlag is equal to 1. It can also happen,

that one hit in the ToF is associated with two or three tracks. For such cases, the matchFlag is equal to 2 or 3, respectively.

Based on the information from ToF relative particle speed β is calculated as

$$\beta_{ToF} = \frac{L}{c\tau}, \tag{2.2}$$

where L is the track length from the primary vertex position to the matched ToF channel and τ is the time of flight. Then from the relation for particle momentum

$$p_{TPC}^2 = \frac{m^2 c^2 \beta_{ToF}^2}{1 - \beta_{ToF}^2}, \tag{2.3}$$

where p_{TPC} is momentum measured by the TPC, the only unknown parameter, particle mass m, can be expressed as

$$m = \frac{p_{TPC}}{c} \sqrt{\left(\frac{1}{\beta_{ToF}} \right)^2 - 1}. \tag{2.4}$$

The ToF excels in particle identification of charged hadrons as illustrated in Figure 2.8, where the $1/\beta$ distribution is presented for charged hadrons. Figure 2.8 shows, that the ToF provides very good identification of charged hadron, pions, kaons and protons up to $p \sim 1.5$ GeV/c and separates protons from other hadrons up to $p \sim 2.9 - 3.1$GeV/c. It also improves electron identification at $p = 0 - 1$ GeV/c.
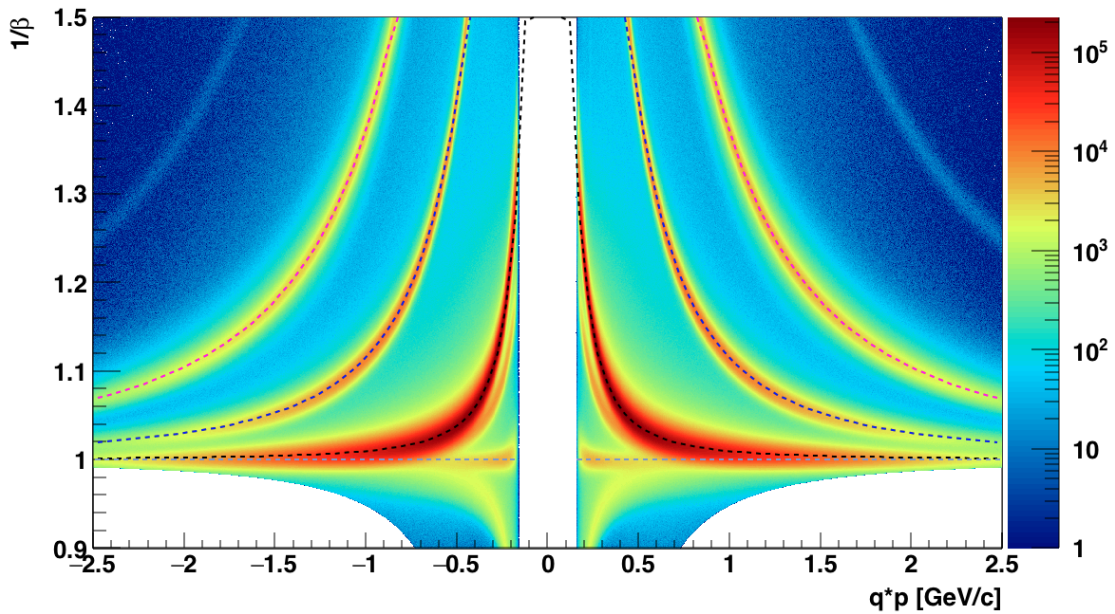
Figure 2.8: The ToF $1/\beta$ versus momentum p and charge q. The dotted lines illustrate the theoretical value for various particle species

2.2.3 Trigger System

The STAR trigger system [36] is based on the fast detectors to control the event selection and makes decision about whether to record the given collision. It can be divided into four layers - Level 0 up

to Level 3. While the Level 0 is the fastest and is based on signal from the ZDC, the BBC and the VDP, the Level 1 and Level 2 are more complex and therefore they take more time. The final Level 3 performs simplified online reconstruction of the events. The minimum bias collisions used in this analysis are collected with trigger based on the ZDC and the VPD. Hence they will be briefly described below.

Zero Degree Calorimeter

The ZDC detectors [36] are located at distance of 18.25 m on the East and West sides from the collisions region, outside of the RHIC dipole magnets. Since the charged particles are deflected by the dipole magnets from the zero degree region, they are not measured in the ZDCs. Therefore ZDCs measure the energy of the neutral particle, mainly the spectator neutrons, which travel in the forwards direction from the collisions. Left panel of Figure 2.9 shows the signal coincidence from the East and West ZDC. With increasing centrality of the collisions, the measured energy in the ZDCs decreases. The measured energy corresponds to the number of neutrons. In case of the peripheral collisions, the measured energy in the ZDC is small due to the fact that the spectator neutrons are bound with protons in the fragments, which are consequently bend by the dipole magnets.

Each ZDC contains three modules and each of them consists of the tungsten layers with the scintillator wave shifter, which direct the Čerenkov light to a photo multiplier.
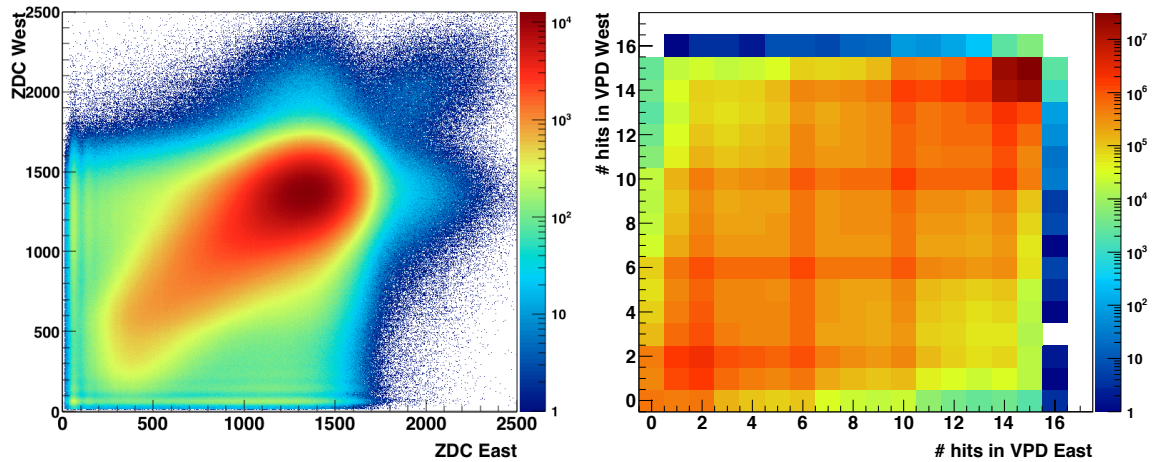
Figure 2.9: Left: The coincidence of the signal from the signal from the East and West ZDCs. Right: The distribution of the hits in the East and West VPDs.

Vertex Position Detector

The VPD detectors [37] are situated at a distance of 5.7 m from the center of the STAR detector. Each VPD detector uses nineteen subdetectors composed of the Pb converter with the plastic scintillator followed by the read out photomultiplier tube. The VPDs detect photons from the π^0 decays, which travel from the primary vertex position at the speed of light and very close to the beam pipe. The arrival times are used to determine the z-components of the primary vertex position via the equation

$$V_z = \frac{1}{2}c(T_{east} - T_{west}),$$

(2.5)

where T_{east} and T_{west} are the arrival times measured by the East and West VPD, respectively. The right panel of Figure 2.9 shows the distribution of the hits in the East and West VPD in Au+Au collisions at $\sqrt{s_{NN}} = 200$ GeV. The resolution of the primary vertex location measured by the VPDs is ~ 1 cm.

The VPD detectors are also important for the particle identification since they provide a starting time t_{start} for the ToF and MTD detectors. The starting time is given via the relation

$$t_{start} = (T_{east} + T_{west})/2 - L/c, \tag{2.6}$$

where L is the distance the VPD subdetectors to the center of the STAR detector. Consequently, the time of flight measured particle is given by

$$\tau = t_{stop} - t_{start}, \tag{2.7}$$

where t_{stop} is measured by ToF or MTD.

2.2.4 Future Upgrade of STAR detector

Since 2000, when the RHIC has started to operate, thanks to progress in accelerator and detector technologies, the average achieved luminosity is almost fifteen times higher than designed and the STAR detector has provided excellent data for analysis covering a wide range of physics topics such as heavy flavor physics, jets, spectra, correlations, flow and event-by-event fluctuation. In the following years, the STAR physics program will be focused on heavy flavor physics, since the newly installed HFT and MTD detectors in combination with increasing statistics allow more precise measurements for heavy flavour physics.

Nowadays the STAR is being upgraded and prepared for the RHIC Beam Energy Scan II planned in 2019-2020. The inner sector of the TPC will be rebuilt and equipped with a continuous coverage of the read-out pads for better dE/dx resolution. The acceptance of the TPC will be extended to $-1.5 < \eta < 1.5$. For better identification, the Endcap Time of Flight (EToF) will be also installed which will provide excellent PID at the forward rapidity. Together with the upgrade of the TPC, STAR will be able to identify the particle with $p_T > 60$ MeV/c, instead of current 150 MeV/c.

Event Plane Detector (EPD), which is going to replace BBC, will allow a better and independent reaction plane measurement, which are critical to BES physics.

The remote future of the RHIC facilities is the upgrade on the electron-ion collider, which is being planned and known as eRHIC [38] with the main physics program focused on study of the structure of the gluon-dominated matter.

CHAPTER
THREE

FEMTOSCOPY

Femtoscopy, measurements of two particle correlations at small relative momenta, is a unique tool for measuring the space-time characteristics of the particle emitting source. In this chapter, the theoretical background of this technique known as femtoscopy and its application in heavy ion collisions will be introduced.

3.1   Historical background of femtoscopy

In 1950's Robert Hanbury Brown and Richard Q. Twiss invented a novel technique based on the photon intensity interferometry [39], which allowed to measure space characteristics of stellar objects. It was alternative to Michelson interferometry, which was one of the most popular and widely used techniques in astronomy. This novel method was tested [40] in Australia during summer 1955, where Brown and Twiss setup two telescopes facilities as shown in the left panel of Figure 3.1. Each of them consisted of the mirror with diameter of 156 cm, which focused light from the measured star to the cathodes of the photomultipliers.
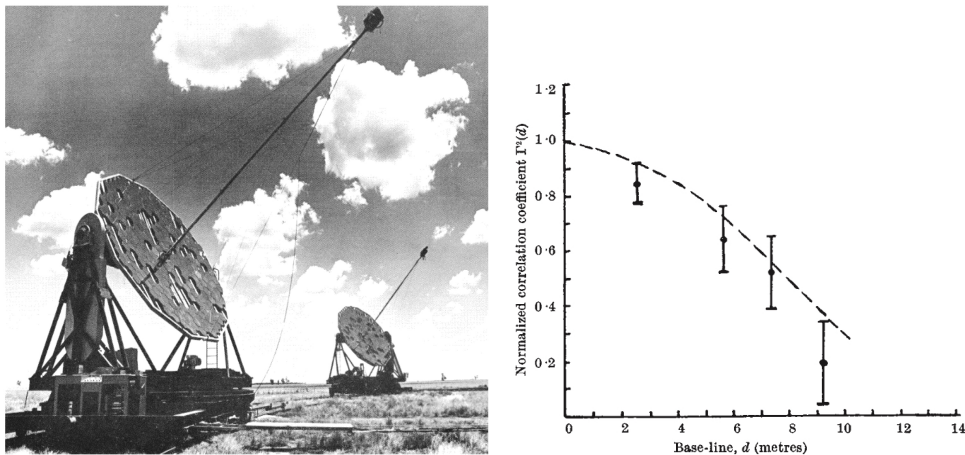
Figure 3.1: Left: Two-telescopes facility used for photon intensity interferometry. Right: Results from the measurement of the photon correlation performed for four various distances of the telescopes. The dotted line represents the theoretical calculation. Taken from [40].

The output signals from both of the multipliers were amplified together in the linear mixer and then the readout system directly measured the correlation between the intensity of the photons received at the both mirrors.

The first measurement was performed with Sirius, a star of spectral type A1 and photovisual magnitude -1.43 [40], which had never been measured directly at that time. The performance of the experiment was divided into two stages. During the first stage of the measurement, the distance of the mirrors was fixed and the experimentalist tried to ensure that observed correlation had not been due to noise in the equipments and to estimate contributions from the night-sky background and other stellar objects. In the second stage of the experiment, the observations were performed for different values of the distance of the telescopes.

Their precise measurement took four months, however a total observation time of 18 hours was achieved. The right panel of Figure 3.1 shows results from their pioneering measurements. The dotted line represents predicted value from the astrophysical theory for star with angular diameter $0.0063''$. As can be seen, the experimental values does not significantly differ from the theoretical calculations.

As a reference to R. Hanbury Brown and R. Q. Twiss and their pioneering measurement, the terms like "HBT" and "HBT radii" are being used in femtoscopy, however their observation, photon intensity interference, is not of a quantum origin and has nothing to do with the correlations in particle physics. The measured correlations in their experiments came from the interference of the two classical electromagnetic fields and persist the limit of quantum mechanics, when $\hbar \to 0$.

A few years later, in 1960, a similar technique was used in particle physics by G.Goldhaber, S. Goldhaber, W.-Y. Lee and A. Pais [41]. They observed in proton-antiproton annihilations an excess of pairs of identical pions produced at small relative momenta,

$$\bar{p} + p \to \pi^\pm + \pi^\pm + n\pi^0 + \ldots . \tag{3.1}$$

They showed that the probability of like-sing pairs emitted at small angles were larger than for unlike-sign pions as shown in Figure 3.2. The observed correlations, as they correctly asserted, came from a quantum statistics.
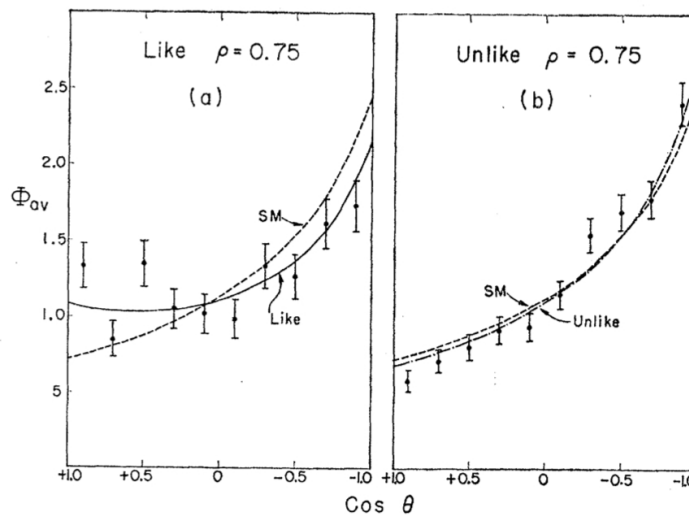
Figure 3.2: The excess of pairs of identical and non-identical pions at small relative momenta in $p + \bar{p}$ collisions. Taken from [41] .

Based on this observation the theoretical background of two particle correlation was developed by G.I. Kopylov and M.I.Podgoretsky in the 1970s [42] who developed mathematical formalism and introduced a new term: correlation functions. They also demonstrated that the correlation function provides information on the phase-space distribution of the emitted particles from the source with a typical space and time extents of order tens fermi. Because of these characteristic sizes, two particle interferometry is very often called femtoscopy, the name introduced by Richard Lednický.

As it is usually presented by Lednický, the Fermi function was the first function, which provided excess to spacial extents of the source in particle physics. Already in 1934 [43], when the β^+ decay was discovered, it was observed that the Coulomb final-state interaction modifies the relative momentum distribution k of $e^{\pm}$ and nucleus in the β-decay. Hence almost 40 years earlier than Kopylov and Podgoretsky defined the correlation function, there were the Fermi function $F(k, R, Z)$ that was sensitive to nucleus radius R, if its charge $Z \gg 1$.

3.2   Two-particle correlation function

The two-particle correlation function in the most general case, as used for non-identical interacting particles, is expressed as

$$CF\left(\boldsymbol{p_1}, \boldsymbol{p_2}\right) = \int \mathrm{d}^3 \boldsymbol{r} S\left(\boldsymbol{r}, \boldsymbol{k^*}\right) \left|\psi_{1,2}\left(\boldsymbol{r}, \boldsymbol{k^*}\right)\right|^2, \tag{3.2}$$

where $S\left(\boldsymbol{r}, \boldsymbol{k}\right)$ is source function describing emission of two particles at a relative distance $\boldsymbol{r}$ with a relative momentum $\boldsymbol{q} = \boldsymbol{p_1} - \boldsymbol{p_2} = \boldsymbol{2k^*}$. The interaction of these particle is encoded into two-particle wave function $\psi_{1,2}\left(\boldsymbol{r}, \boldsymbol{k^*}\right)$. The basic derivation of two-particle correlation function will be present below [17].

The probability of the detection of single particle with four-momentum $p = (E, \boldsymbol{p})$ emitted from a position $x = (t, \boldsymbol{x})$ is related to a single particle emission function $S(x, p)$. The total probability $P\left(\boldsymbol{p}\right)$ arises from integration over the whole source

$$P(\boldsymbol{p}) = \int \mathrm{d}^4 x S(x, p) \left.\right|_{p_0 = E_p}. \tag{3.3}$$

where the emission function is evaluated on-shell, i.e. $p_0 = E_p = \sqrt{m^2 + \boldsymbol{p}^2}$. The probability of detecting two particles can not be simply written as a product of single-particle probabilities, because are not independent processes. The likelihood of detecting the first particle emitted with momentum p_1 from position x_1 is modified by the second emitted particle with momentum p_2 from the position x_2. Hence the total probability of emission of two particle is expressed as

$$P\left(\boldsymbol{p_1}, \boldsymbol{p_2}\right) = \int \mathrm{d}^4 x_1 \mathrm{d}^4 x_2 S(x_1, p_1) S(x_2, p_2) \left|\psi\left(q, r\right)\right|^2, \tag{3.4}$$

where the $\psi\left(q, r\right)$ is the wave function for the two particles reflecting their interaction.

Then the two-particle correlation function can be defined as a ratio of the probability of the emission of two particles to the product of the single-particle emission probabilities. Experimentally, the correlation function is constructed as a ratio of the measured two-particle inclusive spectra to the single-particle inclusive spectra [44]. Mathematically, these two definitions can be written as

$$\begin{aligned} CF\left(\boldsymbol{p_1}, \boldsymbol{p_2}\right) &= \frac{P\left(\boldsymbol{p_1}, \boldsymbol{p_2}\right)}{P\left(\boldsymbol{p_1}\right) P\left(\boldsymbol{p_2}\right)} = \frac{\int \mathrm{d}^4 x_1 \mathrm{d}^4 x_2 S(x_1, p_1) S(x_2, p_2) \left|\psi\left(q, r\right)\right|^2}{\int \mathrm{d}^4 x_1 S(x_1, p_1) \int \mathrm{d}^4 x_2 S\left(x_2, p_2\right)} = \\ &= \frac{\mathrm{d}N^{12} / \left(\mathrm{d}^3 p_1 \mathrm{d}^3 p_2\right)}{\left(\mathrm{d}N^1 / \mathrm{d}^3 p_1\right) \left(\mathrm{d}N^2 / \mathrm{d}^3 p_2\right)}. \end{aligned} \tag{3.5}$$

3.2.1 Identical non-interacting particles

The first femtoscopic measurements were performed with the identical pions because they are the most abundant particle produced in the heavy-ion collisions. Although pions interact by a Coulomb and the strong force, for the first order of approximation, these interactions can be neglected and only quantum statistics can be used for a description of their interaction. In such cases, the relative wave function is express as

$$\psi = \frac{1}{\sqrt{2}} \left[e^{i\left(x_1{}' - x_1\right)p_1} e^{i\left(x_2{}' - x_2\right)p_2} \pm e^{i\left(x_1{}' - x_2\right)p_1} e^{i\left(x_2{}' - x_1\right)p_2} \right], \tag{3.6}$$

where x_i are the emission points and x_i' are the points where the particles were detected. The fact that they are identical particles implies that they are also indistinguishable. Therefore, the emitted particle from the position x_1 can be detected at x_1' or it can be equally likely measured at x_2'. This situation is illustrated by Figure 3.3, where the source emits two particles from the position x_1 and x_2, which are consequently detected at x_1' and x_2', respectively.
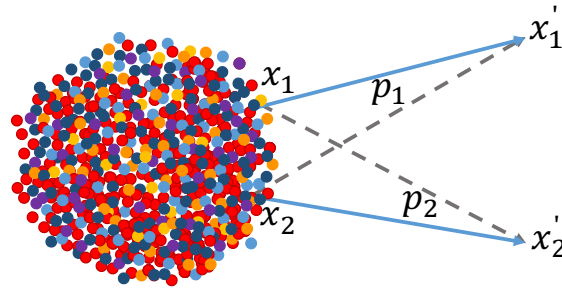
Figure 3.3: The basic principle of the femtoscopy with identical particles. The source emits two particles with momenta p_1 and p_2 from the position x_1 and x_2, respectively. Since the particles are indistinguishable, the first/second particle can be detected at x_1' as well as x_1'.

Hence the wave function has to be either symmetric or antisymmetric. Since the pions are bosons and they do not obey the Pauli exclusion principle, their interaction is characterized by the Bose-Einstein statistics and the wave function Eq 3.6 has to be symmetric (+ sign). While fermions are particles with half-integer spin obeying the Pauli exclusion principle, the Fermi-Dirac statistic is used for their description (- sign in Eq 3.6).

By squaring the wave function and applying relations for the relative pair momentum q and the relative distance r, the following relation is obtained

$$\begin{aligned} |\psi|^2 = \psi\psi^* &= \frac{1}{2} \left(2 \pm 2\cos\left((p_1 - p_2)(x_1 - x_2)\right)\right) = \\ &= 1 \pm \cos\left((p_1 - p_2)(x_1 - x_2)\right) = 1 \pm \cos\left(q \cdot r\right). \end{aligned} \tag{3.7}$$

Putting Eq. 3.7 in Eq. 3.4,

$$
\begin{aligned}
P\left(\boldsymbol{p_1}, \boldsymbol{p_2}\right) &= \int \mathrm{d}^4 x_1 S\left(x_1, p_1\right) \mathrm{d}^4 x_2 S\left(x_2, p_2\right)\left|\psi\left(q, r\right)\right|^2 = \\
&= \int \mathrm{d}^4 x_1 \mathrm{d}^4 x_2 S\left(x_1, p_1\right) S\left(x_2, p_2\right)\left(1 \pm \cos\left(q \cdot r\right)\right) = \\
&= \int \mathrm{d}^4 x_1 \mathrm{d}^4 x_2 S\left(x_1, p_1\right) S\left(x_2, p_2\right) \pm \int \mathrm{d}^4 x_1 \mathrm{d}^4 x_2 S\left(x_1, p_1\right) S\left(x_2, p_2\right) \cos\left(q \cdot r\right) = \\
&= P\left(\boldsymbol{p_1}\right) P\left(\boldsymbol{p_2}\right) \pm \int \mathrm{d}^4 x \mathrm{d}^4 r S\left(x+\frac{r}{2}, K+\frac{q}{2}\right) S\left(x-\frac{r}{2}, K-\frac{q}{2}\right) \cos\left(q \cdot r\right) = \\
&= P\left(\boldsymbol{p_1}\right) P\left(\boldsymbol{p_2}\right) \pm \int \mathrm{d}^4 r \cos\left(q, r\right) \int \mathrm{d}^4 x S\left(x+\frac{r}{2}, K+\frac{q}{2}\right) S\left(x-\frac{r}{2}, K-\frac{q}{2}\right),
\end{aligned}
\tag{3.8}
$$

where the relations for the average pair momentum

$$
K = \frac{p_1 + p_2}{2} = \frac{P}{2}.
\tag{3.9}
$$

and the average pair position

$$
x = \frac{1}{2}\left(x_1 + x_2\right)
\tag{3.10}
$$

were used. Now one of the most common approximation in femtoscopy, *the smoothness assumption*, is applied here. The smoothness assumption is based on the expectation that the emission function has a smooth dependence on the relative momentum and therefore it is possible to rewrite it as

$$
S\left(x+\frac{r}{2}, K+\frac{q}{2}\right) S\left(x-\frac{r}{2}, K-\frac{q}{2}\right) \approx S\left(x+\frac{r}{2}, K\right) S\left(x-\frac{r}{2}, K\right).
\tag{3.11}
$$

This approximation is valid only for small relative momentum q.

Since two emitted particles are on-shell, the components of the four vector q are not independent, but they are related by

$$
q^0 = \boldsymbol{\beta} \cdot \boldsymbol{q},
\tag{3.12}
$$

where

$$
\boldsymbol{\beta} = \frac{\boldsymbol{K}}{K_0} \approx \frac{\boldsymbol{K}}{E_k} = \frac{\boldsymbol{K}}{\sqrt{m^2 + \boldsymbol{K}^2}}.
\tag{3.13}
$$

Hence, Eq. 3.8 can be modified as

$$
\begin{aligned}
&\int \mathrm{d}^4 r \cos\left(qr\right) \int \mathrm{d}^4 x S\left(x+\frac{r}{2}, K\right) S\left(x-\frac{r}{2}, K\right) = \\
&= \int \mathrm{d}^3 \boldsymbol{r} \cos\left(\boldsymbol{q} \cdot \boldsymbol{r}\right) \int \mathrm{d}t \int \mathrm{d}^4 x S\left(x+\frac{r+\boldsymbol{\beta}t}{2}, K\right) S\left(x-\frac{r+\boldsymbol{\beta}t}{2}, K\right)
\end{aligned}
\tag{3.14}
$$

and the relative two-particle source function can be defined as

$$
S_{\boldsymbol{K}}\left(\boldsymbol{r}\right) = \int \mathrm{d}t \int \mathrm{d}^4 x S\left(x+\frac{r+\boldsymbol{\beta}t}{2}, K\right) S\left(x-\frac{r+\boldsymbol{\beta}t}{2}, K\right)
\tag{3.15}
$$

describing emission of two particles at relative distance $\boldsymbol{r}$. Finally, introducing Eq. 3.8 and Eq. 3.14 into Eq. 3.5, two-particle correlation function can be written as

$$
CF\left(\boldsymbol{P}, \boldsymbol{q}\right) = 1 \pm \frac{\int \mathrm{d}^3 \boldsymbol{r} \cos\left(\boldsymbol{q} \cdot \boldsymbol{r}\right) S_{\boldsymbol{K}}\left(\boldsymbol{r}\right)}{\left|\int \mathrm{d}^4 x S\left(x, K\right)\right|^2}.
\tag{3.16}
$$

In a case, when the total probability defined by Eq. 3.3 is normalized to the unity, the previous relation simplifies to

$$
CF\left(\boldsymbol{P}, \boldsymbol{q}\right) = 1 \pm \int \mathrm{d}^3 \boldsymbol{r} \cos\left(\boldsymbol{q} \cdot \boldsymbol{r}\right) S_{\boldsymbol{K}}\left(\boldsymbol{r}\right).
\tag{3.17}
$$

As can be seen, the correlation function for identical non-interacting particles is a Fourier transformation of the relative source function, into which the time information is convoluted. The deconvolution of the t and $\boldsymbol{r}$ can only be done by employing a model describing four-dimensional particle emission. Hence, the experimental measurements of the correlation function goes hand in hand with model treatment of space-time evolution of the considered system.

Since the correlation function is a Fourier transformation of the relative source function, it is very useful to parametrize the source by a function for which its Fourier transform has an analytic form. One of the most common parametrization is by a Gaussian,

$$S\left(x,p\right) = \frac{1}{\pi^2 R_{inv}^3} e^{-\left(\frac{r}{R_{inv}}\right)^2},$$

(3.18)

where R_{inv} is the source radius. In such a case the Fourier transform exists and it is an analytical function

$$CF\left(\boldsymbol{q}\right) = 1 \pm e^{-\boldsymbol{q}^2 R^2}.$$

(3.19)

Figure 3.4 presents a correlation function for which the source has been parametrized by a Gaussian according to Eq. 3.18. As can be seen, the correlation function is sensitive to the source size. In the case of large source the particles are emitted at larger average distance and therefore the correlation is weaker in comparison with the smaller source.
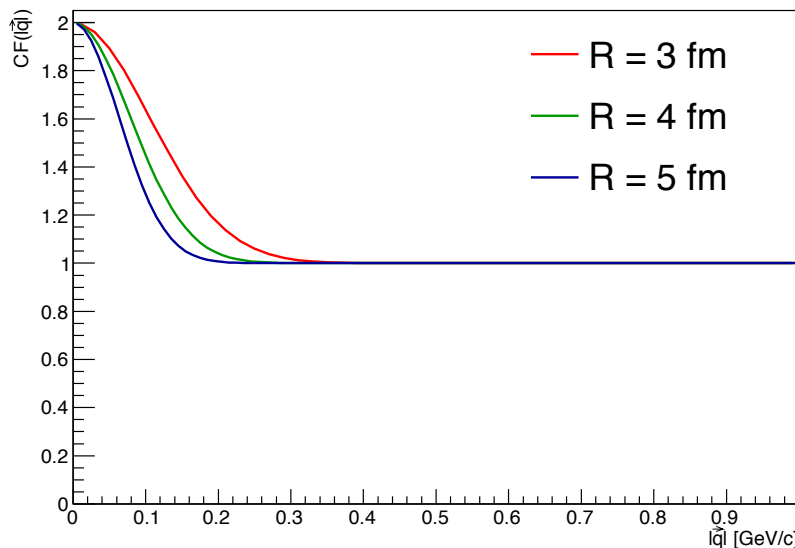
Figure 3.4: The correlation function constructed according to Eq. 3.19 for three values of the source radius.

3.2.2   Identical interacting particles

The previous derivation dealt with non-interacting particles. Pair of identical pions can be, to a certain degree, treated as pair of identical non-interacting particles. However this approximation cannot be used when Coulomb and possibly even strong interaction has to be taken into account.

While for like-sign particles, the Coulomb force is repulsive and causes a suppression of the measured correlation function at low q, the unlike-sign particles are being attracted by the Coulomb

interaction and an enhancement of the experimentally constructed correlation function at low q can be observed. The particles can interact also via a strong final-state interaction. In some cases such as for identical pions and kaons, the strong interaction can be neglected. However, for unlike-sign kaons or proton-antiproton correlation the strong interaction plays important role and can not be neglected.

Both interactions affect the correlation function at low q. Figure 3.5 shows the theoretically calculated like-sign kaons correlation function of identical kaon with individual contribution from the quantum statistics, Coulomb FSI and strong FSI, respectively. The strong interaction is also present at the low q, but in our cases it is beyond our scale of y-axis. Experimentally, the correlation function, which is a combination of these functions, is measured. This function is also presented in Figure 3.5.
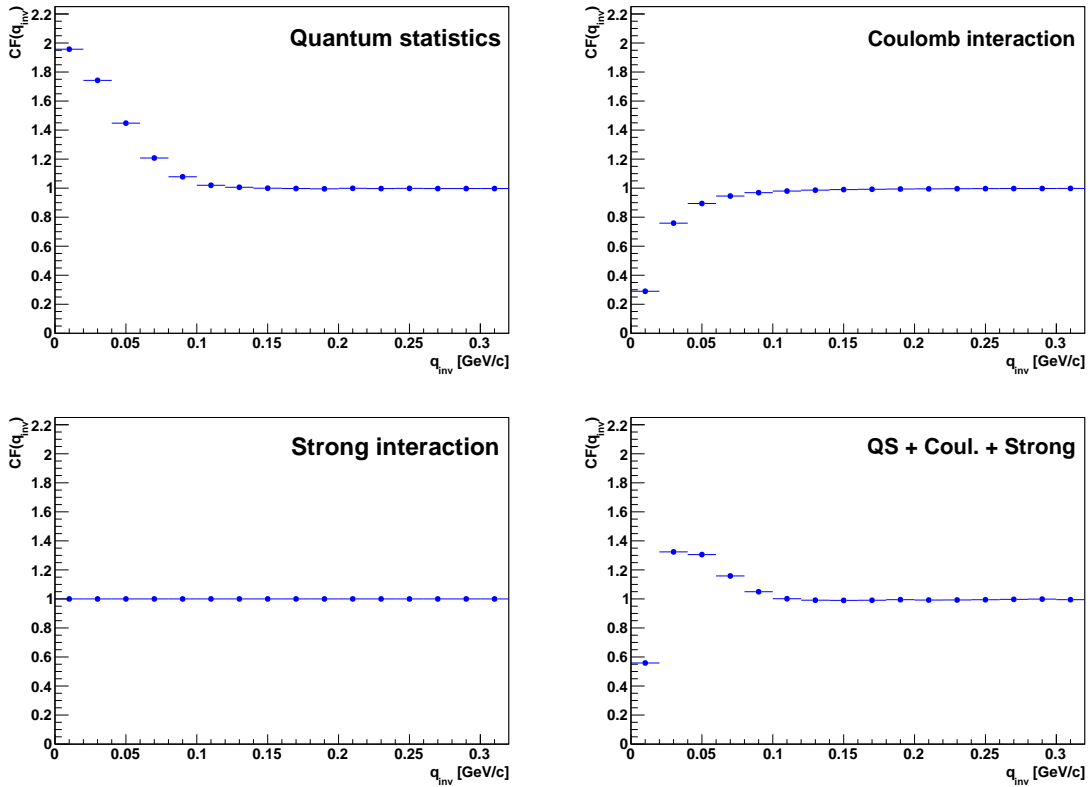
Figure 3.5: The theoretical like-sign kaon correlation function constructed with the wave function which describes Quantum statistics, Coulomb interaction and/or Strong interaction.

In order to take into account the Coulomb and strong FSI, the interaction should be introduced into the wave function, as used in the theoretical calculation. The detailed description, how to introduced FSI into the wave function and how to derive the correlation function with such a wave function can be found in [45].

Another was how to tak care of the Coulomb FSI is to seperately evaluate its contribution using so called Coulomb factor $K_{Coul}(q_{inv})$

The Coulomb wave function, as a solution of the Schrödinger equation [17], can be written in terms of the confluent hypergeometric function F as

$$\psi_c(\boldsymbol{q}, \boldsymbol{r}) = \Gamma(1 + i\eta_\pm)\mathrm{e}^{-\frac{1}{2}\boldsymbol{q}\cdot\boldsymbol{r}}F\left(-i\eta, 1, z_\pm\right), \tag{3.20}$$

where

$$z_{\pm} = \frac{1}{2} \left(qr \pm \boldsymbol{q} \cdot \boldsymbol{r} \right) = \frac{1}{2} qr \left(1 \pm \cos\theta \right). \tag{3.21}$$

Here θ it the angle between $\boldsymbol{q}$ and $\boldsymbol{r}$. The $\eta_{\pm}$ are the Sommerfeld parameters depending on the particle mass m and charge e as

$$\eta_{\pm} = \pm \frac{me^2}{4\pi q}, \tag{3.22}$$

where the minus sign is for like-sign pairs, while the plus sign is for unlike-sign particles. Then the symmetrized Coulomb wave function can be written as

$$\psi_r \left(\boldsymbol{q}, \boldsymbol{r} \right) = \frac{1}{\sqrt{2}} \left(\psi_c \left(\boldsymbol{q}, \boldsymbol{r} \right) + \psi_c \left(\boldsymbol{q}, -\boldsymbol{r} \right) \right). \tag{3.23}$$

Now, by putting square of Eq. 3.23 into Eq. 3.4, the Coulomb contribution to the probability of the emission of two particles can be calculated as

$$P_c \left(\boldsymbol{p_1}, \boldsymbol{p_2} \right) = \frac{1}{2} \int \mathrm{d}^4 x_1 \mathrm{d}^4 x_2 S(x_1, p_1) S(x_2, p_2) \left| \psi_r \left(\boldsymbol{q}, \boldsymbol{r} \right) \right|^2. \tag{3.24}$$

Finally, the Coulomb factor will be defined as the integrated Coulomb wave function over a Gaussian source

$$K_{coul} \left(q_{inv} \right) = \int \mathrm{d}^3 r \rho \left(\boldsymbol{r} \right) \left| \psi_r \left(\boldsymbol{r}, \boldsymbol{q} \right) \right|^2. \tag{3.25}$$

It has been shown in [46] that the Coulomb factor depends on source size R_{inv} as R_{inv}^{-1} and vanish with increasing q_{inv} as

$$\left(1 - \frac{2}{aR_{inv} \left(q_{inv}/2 \right)^2} \right)^{1/2} \approx 1 - \frac{1}{aR_{inv} \left(q_{inv}/2 \right)^2}, \tag{3.26}$$

where a is the pair Bohr radius [46].

As it will be shown in the following chapter, a correction using the Coulomb factor can be used during the fitting procedure of the experimentally measured correlation function.

3.2.3 Coordinate system and parametrization

Considering the typical symmetries of nucleon collisions and resulting emission functions, the standard Cartesian system is not optimal. The most common system for femtoscopic measurement is the so called Bertsch-Pratt coordinate system [44], often known as the "out-side-long system". This coordinate system is connected with emitted pair of particles and is characterized by three axis, namely longitudinal, outward and sideward axis, which are defined the following way. The longitudinal axis is parallel to the beam direction which typically coincides with z-axis (or beam directon) as shown in Figure 3.6. The direction of the outward axis is parallel to pair transverse momentum k_T. The last axis, the sideward axis, is chosen so that it is perpendicular to the longitudinal and outward axes. As can be seen from the choice of the outward axis, the Bertsch-Pratt coordinate system is unique for each pair of particles. The components of any vector $\boldsymbol{V}$ are projected as

$$\begin{aligned} V_{long} &= V_z \\ V_{out} &= \left(P_x V_x + P_y V_y \right) / P_T \\ V_{side} &= \left(P_x V_y - P_y V_x \right) / P_T, \end{aligned} \tag{3.27}$$

where $P = \left(P_0, P_x, P_y, P_z \right)$ is pair momentum and $P_T^2 = P_x^2 + P_y^2$.
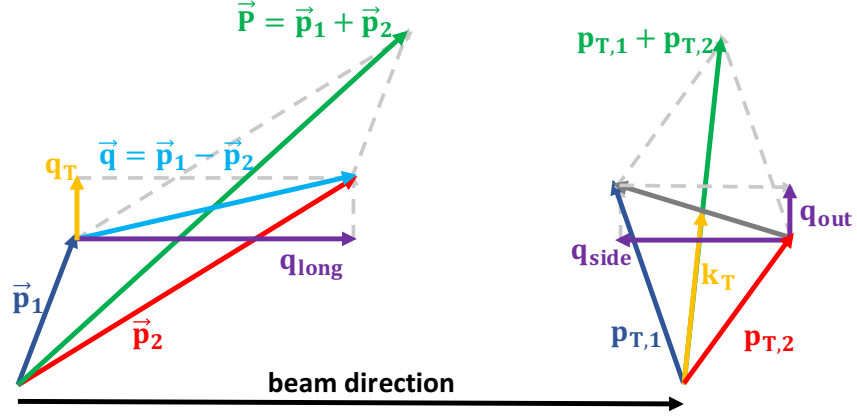
Figure 3.6: The decomposition of $\boldsymbol{q}$ vector in Bertsch-Pratt coordinates system.

While the femtoscopy with identical particles is most commonly performed in the longitudinally co-moving system (LCMS) of the emitted pair where the components of pair momentum in long direction vanishes, the correlations of non-identical particles are studied in the pair's rest frame (PRF).The LCMS frame can be obtained by the boost from the laboratory frame along the longitudinal axis (beam direction). Additional boost of the LCMS frame in the out direction provides the PRF. In the PRF, both particles have the same momentum

$$\boldsymbol{k^*} = \boldsymbol{k_1} = -\boldsymbol{k_2} \tag{3.28}$$

and hence the relative pair momentum is

$$\boldsymbol{q} = 2\boldsymbol{k^*}. \tag{3.29}$$

To extract physical understanding of the space-time structure of the measured source, it is useful to describe the source with a few a parameters. The simplest parametrization of the single particle emission function, as shown by Eq. 3.18, is a Gaussian. The Gaussian is most commonly used parametrizaton Although it is known that realistic sources, especially pion source, deviate from Gaussian. The observed deviations were studied by the sophisticated method known as source imaging [47] and it was shown that the relative source function deviates from the Gaussian. This can be ascribed to resonance decays.

The simplest correlation function is constructed only in one dimension as a function of q_{inv} which is defined

$$q_{inv} = \sqrt{(E_1 - E_2)^2 - (\boldsymbol{p_1} - \boldsymbol{p_2})^2}. \tag{3.30}$$

Then the most common parametrization of the source is via parameter R_{inv} and the one-dimensional correlation function can be written as

$$CF(q_{inv}, \boldsymbol{K}) = 1 + \lambda(\boldsymbol{K}) \exp\left(-q_{inv}^2 R_{inv}^2(\boldsymbol{K})\right), \tag{3.31}$$

where λ is the lambda parameter and R_{inv} is the Gassian source radius. Disadvantage of such a parametrization is the fact that all spacial and temporal information are convulated into R_{inv}. On the other hand for low-statistics measurements this can be the only way how to extract space-time extents.

Three-dimensional correlation function in LCMS is often parametrized by

$$C(\boldsymbol{q}, \boldsymbol{K}) = 1 + \lambda(\boldsymbol{K}) \exp\left(-R_o^2(\boldsymbol{K})q_o^2 - R_s^2(\boldsymbol{K})q_s^2 - R_l^2(\boldsymbol{K})q_l^2\right), \tag{3.32}$$

where the interpretaion of the HBT radii is following [48]:

$$\begin{aligned}
R_o^2(\boldsymbol{K}) &= \left\langle \left(\widetilde{x} - \beta_T \widetilde{t}\right)^2 \right\rangle \\
R_s^2(\boldsymbol{K}) &= \left\langle \widetilde{y}^2 \right\rangle \\
R_l^2(\boldsymbol{K}) &= \left\langle \left(\widetilde{z} - \beta_l \widetilde{t}\right)^2 \right\rangle.
\end{aligned} \tag{3.33}$$

Here, β_l and β_T are the components of the pair velocity. The symbol $\widetilde{x}$ denotes the $\langle \Delta x \rangle$ and $\langle \rangle$ denotes an average. An important observation resulting from this parametrization, which was extensively experimentally studied, is that the ratio of R_o^2/R_s^2 is sensitive to the lifetime β_T of the measured source. The lifetime is also often studied via a difference [48]

$$R_{\text{diff}}^2 = R_o^2 - R_s^2 = \beta_T^2 \left\langle \widetilde{t}^2 \right\rangle - 2\beta_T \left\langle \widetilde{x}\widetilde{t} \right\rangle + \left(\left\langle \widetilde{x}^2 \right\rangle - \left\langle \widetilde{y}^2 \right\rangle\right), \tag{3.34}$$

where the first term representing the lifetime of the source is dominant [49].

Thanks to increasing statistics in combination with improving detectors which enable to measure event-plane the correlation function can be parameterized in the most general cases by

$$CF(\boldsymbol{q}, \boldsymbol{K}) = 1 + \lambda(\boldsymbol{K}) \exp\left(-\sum_{i,j=o,s,l} R_{ij}^2(\boldsymbol{K}) q_i q_j\right). \tag{3.35}$$

Here the correlation function depends on the 6 HBT radii, R_{ij}^2 and allows azimuthal-sensitive femtoscopic measurements.

λ parameter

During parametrization of the correlation function, the λ parameter has been introduced. Its importance arises from the fact that the experimentally measured correlation functions are significantly smaller then the theoretical ones. The λ parameter controls the magnitude of the measured correlation function. The λ factor was initially introduced to account for the partially coherent emission of particles, but it has been shown that the particle source is completely chaotic. The reason for λ being smaller than the unity is a contamination of the studied particles with misidentified particles. It is also influend by decay of long-lived resonance.

3.2.4 Non-identical interacting particles

Femtoscopy with non-identical particles provides additional information about the source, emission asymmetries [50]. The asymmetries are results of the dynamic evolution of the created system and can be of both spacial and temporal origin. This is especially interesting for multi-strange baryons which can be emitted earlier than other hadrons and baryons due to their relatively small cross section with hadronic matter.

In the case of non-identical particles, the correlation occurs due to Coulomb FSI and/or Strong FSI. The technique used here to construct the correlation function is the same as in the previous case except for one difference. According to the value of the k^*, the pairs are divided in two groups. While the first group contains pairs with positive k_{out}^*, the pairs with negative k_{out}^* are in the second

ground. The case when k_{out}^* is positive correspond to situation when the slower particle is emitted closer to the edge of the source and the faster particle catch up with the slower particle. Also earlier emission of the slower particle and consequently catching up with the faster particle can results in positive k_{out}^*. In these two cases, the correlation effect is stronger and the duration of the interaction is longer. Hence the constructed correlation function for positive k_{out}^* are denoted as CF_+. The situation when the faster particle is emitted earlier and/or closer to the edge of the system is characterized by negative k_{out}^*. Since one particle flies away from the other, the correlation is weaker and the time of the interaction is shorter. Hence the correlation function are denoted as CF_-.

Then these asymmetries can be studied by the "double-ratio" defined as CF_+/CF_-. In case of the azimuthal symmetry and symmetry about mid-rapidity, the asymmetries in long and side-direction should be equal to unity i.e.

$$\langle \Delta r_{side} \rangle = \langle \Delta r_{long} \rangle = 0. \tag{3.36}$$

Thus CF_+/CF_- defined with respect to the signs of k_{side}^* and k_{long}^* should not deviate from unity. This fact can be employed as a quality-check of the non-identical correlation function.

Only asymmetries which can be observed is in out-direction as a result of [51]

$$\langle r_{out}^* \rangle = \langle \gamma \left(\langle \Delta r_{out} \rangle - \beta_\perp \langle \Delta t \rangle \right) \rangle . \tag{3.37}$$

As can be seen the observed asymmetry is a superposition of the spacial and temporal asymmetry.
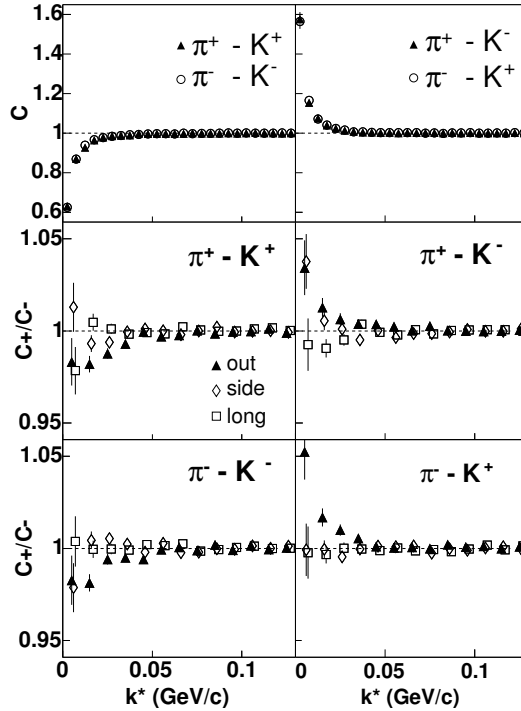
Figure 3.7: Results on measured pion-kaon correlations. Top panel: correlation function $C(\vec{k^*})$ for various pair combinations. Middle and botton panel: double ratio of correlation function $C_+(\vec{k^*})$ and $C_-(\vec{k^*})$. Taken from [52].

Good example of the femtoscopic measurements with non-identical particles are pion-kaon correlations [52] shown in Figure 3.7. Within statistics errors, the double ratios of the correlation function defined with respect to the signs of k_{side}^* and k_{long}^* are equal to unity. The observed deviation of the

double-ratio for out-direction at low k^* indicates the spacial and/or temporal asymmetry in emission of kaons and pions which is a typical consequence of collective transverse expansion.

3.3   Hydrodynamic models and femtoscopy

The measured HBT radii, as it was mentioned in the previous subsection, non-trivially mix spatial and temporal information on the studied source. In addition, the correlation function is sensitive to the relative source function $S_{\boldsymbol{K}}\left(\boldsymbol{r}\right)$ depending on the relative distance of two measured particles $\boldsymbol{r}$. If there exists a correlation between emission points and particle momenta then it is important to understand that the measured radii can not be simply identified as the size of the whole system. The two-particle correlations provide information about the region of the source from which pair of particles with given relative momentum can be emitted. This region is called the homogeneity region and its size is the homogeneity length.

The sizes of the homogeneity regions are influenced by the expansion and space-time evolution of the measured source. As a results of the collective flow, there is the correlation of the total pair momentum and position of the emission, noted as x-p correlations. Therefore HBT radii, the homogeneity lengths, depend on the pair momentum and carry information about the dynamical properties of the source. The dependence of the HBT radii on the pair momentum is illustrated in Figure 3.8 showing homogeneity regions for different magnitudes of pair momenta.
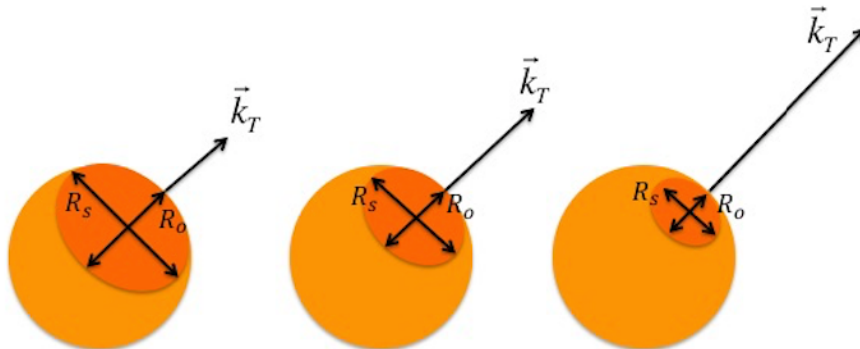
Figure 3.8: Homogeneity regions for different pair transverse momenta.

For this reason, to obtain complete insight into space-time evolution of studied source, it is necessary to compare experimental results to models of the heavy-ion collisions which are able to produce the particles with space-time coordinates at the moment of their freeze-out. Hydrodynamical calculations are able to satisfactorily describe the evolution of the created system during heavy-ion collisions. However it is more common and easier to use a family of simplified models which work with hydro-inspired parametrization of the particle emitting source. There are many such models. Some of them can be quite sophisticated, including such effect as resonances and particle decays. Example of this model can be a HYDJET++ [53] or THERMINATOR 2 [54].

3.3.1   Blast-wave parametrization

One of the most commonly used model in femtoscopy is the blast-wave parametrization [55]. The blast-wave parametrization is based on the hydrodynamic calculations aiming to describe the system

at the freeze-out with a minimal set of parameters. This parametrization allows to calculate at the same time bulk properties such as spectra, elliptic flow as well as HBT radii. In contrast with the full hydrodynamics calculations, the blast-wave model is very fast thus it can be effectively used for simultaneous fitting of experimentally measured observable which are connected with the configuration of the bulk of the system.

In this thesis, the blast-wave parametrization [55] developed by Retiere and Lisa will be used. The model employs eight independent parameters to characterize the source. These parameters are T, ρ_0, ρ_2, R_y, R_x, a_s, τ_0 and $\Delta\tau$ and their physical meaning will be given below. As can be seen, the parameterization provides insight into the final configuration of the system, rather than the initial conditions and evolution of the studied system.

The source is parametrized in the Cartesian coordinate system, where the $x - z$ plane is the reaction plane. The model assumes infinite freeze-out configuration in the z(beam) direction, while in the transverse $(x - y)$ plane there is elliptical distribution controlled by the radii R_x and R_y. The system is divided into the source elements and their spatial weighting is given by

$$\Omega\left(r, \phi_s\right) = \Omega\left(\widetilde{r}\right) = \frac{1}{1 + e^{(\widetilde{r}-1)/a_s}},$$ (3.38)

where the normalized elliptical radius is defined as

$$\widetilde{r}\left(r, \phi_s\right) \equiv \sqrt{\frac{\left(r\cos\left(\phi_s\right)\right)^2}{R_x^2} + \frac{\left(r\sin\left(\phi_s\right)\right)^2}{R_y^2}}.$$ (3.39)

The $\widetilde{r}$ hence corresponds to a given elliptical sub-shell within the solid volume of the freeze-out distribution. The emission source has a surface diffuseness parametrized by the density profile a_s. The box profile of the surface can be realized by setting $a_s = 0$, while the Gaussian shape of the density profile is for $a_s = 0.3$

The momentum spectrum of emitted particles from the source element at (x, y, z) is given by a fixed temperature T of the thermal kinetic motion at the rest frame of the elements. It is then boosted by a transverse rapidity $\rho(x, y)$. The boost strength depends on the centrality of the collisions. Authors of the models assumed that for central collision the rapidity profile linearly changes with the normalized elliptical radius $\widetilde{r}$. Hence in absence of the azimuthal dependence of the flow all source elements on the outer edge of the source would be boosted with the same transverse rapidity ρ_0 in the outward direction. To account for azimuthal flow in non-central collisions, the boost strength is connected with the azimuthal angle ϕ_s. The dependence of the strength of the flow boost and the azimuthal angle ϕ_s is realized via a parameter ρ_2. Its physical meaning is the strength of the second-order oscillation of the transverse rapidity. The left panel of Figure 3.9 illustrates such dependence. Based on these assumptions the resulting flow rapidity is

$$\rho\left(r, \phi_s\right) = \widetilde{r}\left(\rho_0 + \rho_2 \cos\left(2\phi_b\right)\right),$$ (3.40)

where ϕ_b is the azimuthal direction of the boost and ϕ_s is the spacial azimuthal angle. In particular, this part of the parametrization produces the source anisotropy and therefore its important for understanding the measurements of the elliptic flow and azimuthal sensitive HBT. The $\rho_2 > 0$ produces the positive elliptic flow and the boost is stronger in the in-plane direction. On the other hand, the positive elliptic flows can be generated when $\rho_2 = 0$, however in addition $R_y > R_x$ is needed.

As it was discussed the source is the longitudinally boost-invariant and the freeze-out occurs with the Gaussian parametrization

$$\frac{dN}{d\tau} \sim \exp\left(-\frac{\left(\tau - \tau_0\right)^2}{2\Delta\tau^2}\right),$$ (3.41)
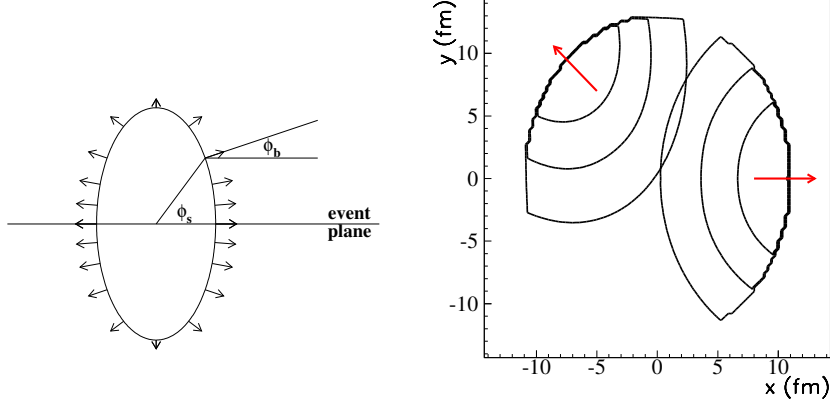
Figure 3.9: Left: Sketch of the dependence the flow boost (represented by the arrows) on the spacial azimuthal angle ϕ_s and the azimuthal direction of the boost ϕ_b. Right: Schematic illustration of the source compounded of two homogeneity regions. The arrows indicate the direction of the particle emission. Taken from [55].

in longitudinal proper time of the source $\tau = \sqrt{t^2 + z^2}$. The τ_0 corresponds to a proper average emission time and the emission duration is equal to $\Delta\tau$. Within this model the time dependence of the emission function enters only via Eq. 3.41. In reality one would naturally expects that all other parameters such R_x, R_y, ρ, etc. would also depend on the time. However such time dependence is beyond spirit of this model and for its inclusion a true dynamic model is needed.

In a summary a single particle emission function in the blast-wave model is parametrized as

$$S\left(x,p\right) = S\left(r,\phi_s,\tau,\eta\right) = m_T \cosh\left(\eta - Y\right)\Omega\left(r,\phi_s\right)\mathrm{e}^{\frac{-(\tau-\tau_0)^2}{2\Delta\tau^2}}\sum_{n=1}^{+\infty}\left(\mp 1\right)^{n+1}\mathrm{e}^{-np\cdot u/T}, \qquad (3.42)$$

where the Y is rapidity and u is the four-velocity. The bulk properties of the studied system like spectra, elliptic flow or HBT radii can be calculated from the single particle emission function. For example it can be mentioned that azimuthally integrated transverse particle spectra is given by

$$\frac{\mathrm{d}N}{p_T\mathrm{d}p_T} = \int \mathrm{d}\phi_p \int \mathrm{d}^4 x S\left(x,p\right). \qquad (3.43)$$

and the elliptic flow as

$$v_2\left(p_T,m\right) = \frac{\int_0^{2\pi}\mathrm{d}\phi_p\left\{\cos\left(2\phi_p\right)\right\}_{0,0}\left(p\right)}{\int_0^{2\pi}\mathrm{d}\phi_p\left\{1\right\}_{0,0}\left(p\right)}. \qquad (3.44)$$

Detailed discussion on how these observables change with different values of the used parameters can be found in [55].

For the purpose of this thesis, the most important are the conclusions from discussion on how the HBT radii depend on parametrization of the source. Therefore they will be discussed in more detail.

As authors have noted, their model is in agreement with previous work [48], which also show that R_l^2 carries information about the lifetime of the source and can be parametrized as

$$R_l^2\left(m_T\right) = \tau_0^2\frac{T}{m_T} \times \frac{K_2\left(m_T/T\right)}{K_1\left(m_T/T\right)}, \qquad (3.45)$$

where K_n is the n-th modified Bessel function. In combination with the spectra providing temperature T, this relation can serve to obtain the emission duration of the measured source. Since the R_s^2 contains

only spacial information and the value of R_o^2 is sensitive to the temporal extents of the source, the dynamical properties of the measured system can be described by the ratio of R_o^2 to R_s^2 as well as the difference R_o^2 and R_s^2.

Finally, the effect of the flow included in the blast-wave model and the temperature on the homogeneity regions will be discussed. These effects result into a shift between the average freeze-out space-time point of different particle species as well as different homogeneity lengths for different particle species.

Due to the radial flow the particles' emission points and momenta are correlated so that the particles with higher momenta are emitted more on the outside of the source. This is the effect of the collective expansion. The size of the emission region is controlled by the transverse flow which competes with the thermal motion.
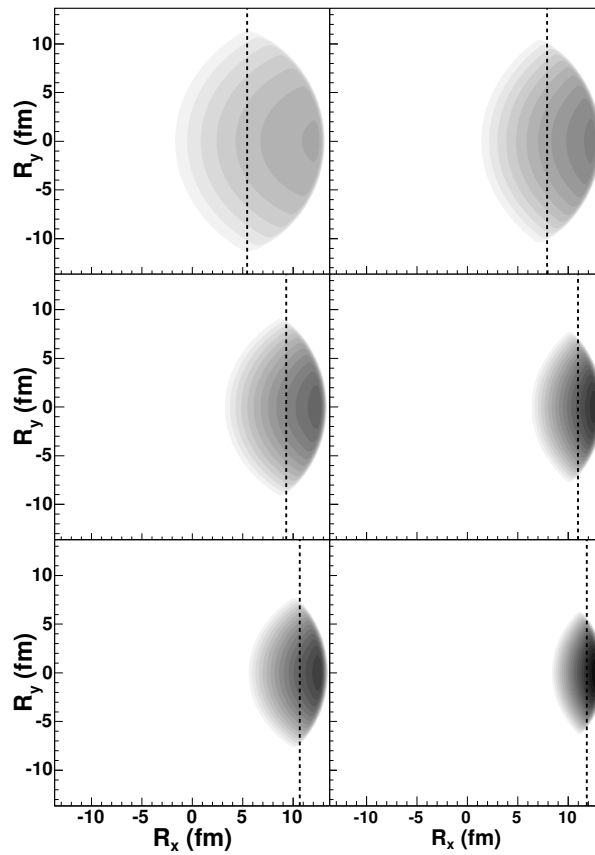
Figure 3.10: The homogeneity region and the average emission points for various particle species emitted at the same transverse velocity $\beta_x = 0.907$ on the left-hand side and $\beta_x = 0.974$ on the right-hand side. Top panel is for pion, middle panel for kaons and bottom for proton. Taken from [55].

While the transverse flow decreases the homogeneity length due to the increasing correlation between position and momentum, the thermal motion is superimposed on the flow and increases the size of the homogeneity region by random thermal motion of the emitted particles over a volume of the system. Such phenomenon known as thermal smearing effect makes the particle velocity a sum of the flow velocity β_f and the thermal velocity β_t. Thus in the case of non-identical particles with the same momenta, the average emission points are different.The average emission point of the lighter particle

is closer to the center of the system and the homogeneity length corresponds more closely to the size of the studied source. To sum up previous discussion, it can be briefly said that the homogeneity region decreases with the particle m_T, while the shift of average emission point increases with the m_T. Such dependence is illustrated in Figure 3.10 where the homogeneity regions are shown for different particle species(pions, kaons and protons) emitted with the same velocity. The freeze-out conditions such as temperature, flow profile, freeze-out time and position are the same for all particle species. The dashed lines show the shift of the mean emission position of the homogeneity region.

3.4 Overview of femtoscopic results

One of the first femtoscopic measurement of the heavy-ion collisions was performed by the NA35 Collaboration about thirty years ago [56]. Since then, increasing statistics of the data sets allowed three dimensional correlation measurements with small statistical errors. In combination with the development sophisticated methods which reduced the systematics errors to the level of $\sim 5\%$ [44], the femtoscopy has became one of the most precise tool for measuring the space-time extents in heavy-ion collisions. In the following part of this section the overview of femtoscopic measurements will be presented.

3.4.1 Collective dynamics and m_T dependence

As was already discussed, the dynamical evolution structure of the source over its lifetime is encoded into its space-time extensions at the freeze-out via space-momentum $(x - p)$ correlations. The expansion and evolution of the measured system is characterized by the collective flow which generates a typical falling off the HBT radii with increasing m_T of the measured pair. Figure 3.11 shows the collection of results on the m_T dependence of the HBT radii from the $\pi^{\pm} - \pi^{\pm}$ correlations from central Au+Au or Pb+Pb collisions. Although the collision energy has changed over the magnitude of two orders, the observed dependence is surprisingly similar for all energies.
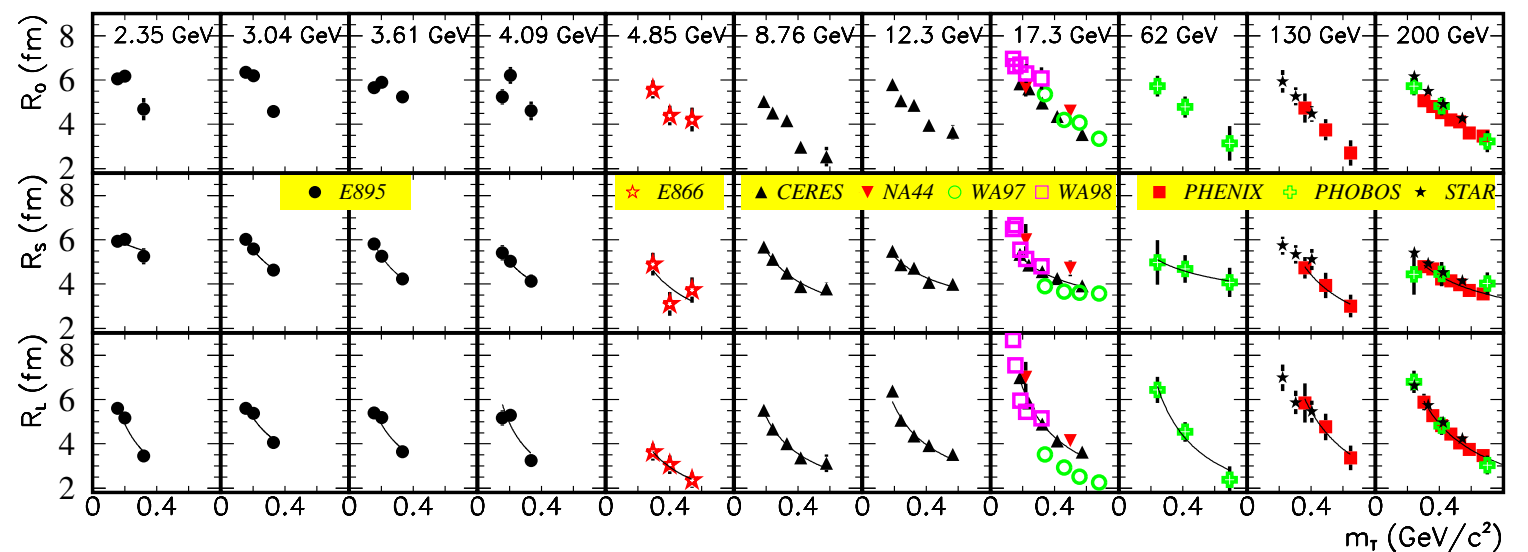
Figure 3.11: World data set of m_T dependence of HBT parameters from $\pi - \pi$ femtoscopics measurements. Taken from [44].

As can be seen in Figure 3.12, the m_T scaling is the ubiquitous property of the HBT radii. Figure 3.12 presents results on measured R_{inv} for various particle species with different masses at the same collisions energy. For not so abundant strange particles such as Λ, only one dimensional correlation functions are accessible. However all of the particle species follow the typical m_T scaling. Such behavior is typical sign of the collection expansion of the system created in heavy-ion collisions.
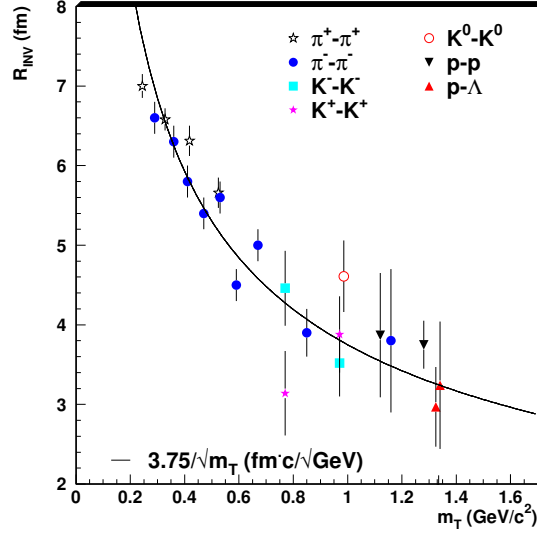
Figure 3.12: The universality of m_T dependence of R_{inv} for different particle species. Taken from [57].

3.4.2 Hydrodynamic predictions and "HBT puzzle"

One of the first theoretical prediction based on the hydrodynamic models assumed that in case that the system created in heavy-ion collisions undergoes the first order phase transition the emission duration will be prolonged due to rapid increase of the entropy. Such behavior should appear in the sudden change of the R_o/R_s ratio, since this ratio is sensitive to the lifetime of the source. The prediction hoped that the magnitude of the ratio will increase of the one order [58]. Hence it was the one of the most promising candidate for a "smoking gun" for discovery of the first order phase transition.

The collection of the results from these measurement, when the collision energy changes over the three orders of magnitude is shown in the left panel of Figure 3.13. No sudden change of R_o/R_s has been observed so far by these systematic studies. Within statistic and systematic errors, the ratio of R_o/R_s varied from 1.0 to 1.3 . While the R_l and R_s shows change in behavior with increasing energy, the R_o is almost constant. The observed decrease and ensuing rising of R_l and R_s is related with the volume of the created system and the particle species which dominated in the created source at the given collision energy. At low energies the system is dominated by the baryon matter, while at higher energies there is larger pion multiplicity, hence the source has the larger freeze-out volume.

The right panel of Figure 3.13 provides a detailed view on the results from the $\pi - \pi$ femtoscopy from the BES. The bottom panel presents the ratio of R_o/R_s, while the difference of these HBT radii is shown in the top panel. In both cases, the significant peak can be observed. It is argued that
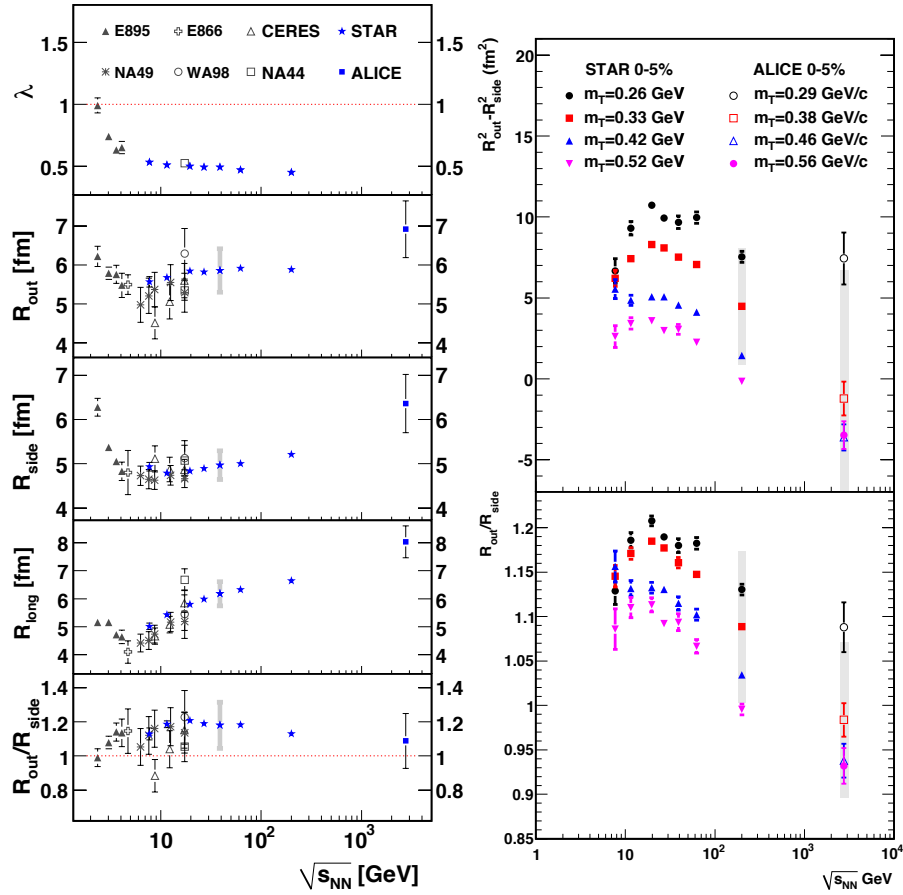
Figure 3.13: Left: The collection of the results from the $\pi - \pi$ femtoscopy from various collision energy performed at midrapidity with $k_T = 0.2 - 0.3\text{GeV}/c$. Right: The ratio and difference of the R_o and R_s radii as a function of the collision energy. Taken from [59].

such a behavior is connected with the phenomenon known as the softening of the equation of state in the vicinity the critical point. Its location in the phase-space diagram can be determined by the critical divergences of some source parameters. The difference of the R_o^2 and R_s^2 is sensitive to the susceptibility κ and non-monotonic patterns for HBT radii can indicate such divergence of κ [60]. So far, the location of the critical point is still an open question in the heavy-ion physics.

The detailed comparison of prediction of dynamic models heavy-ion collisions to the experimental data becomes increasingly more important as experimental data become more precise and include larger variety of particle species. The hydrodynamical calculation are successful in description of the momentum observables such as particle spectra and flow in soft sector i.e. $p_T < 2\text{GeV}/c$. However they usually fail in fully reproducing the femtoscopic results as shown in the left panel of Figure 3.14. As can be seen in Figure 3.14, the various hydrodynamical and hybrid models can not reproduces at the same time all the HBT radii. Experimentally measured radii from the $\pi - \pi$ correlation are significantly differ than those predicted by models. This discrepancy of the model prediction and historical lack of evidence for the first order transition was often called the "HBT puzzle". For resolving the HBT puzzle more realistic models of heavy-ion collisions must be used. It shows that the necessary components of these models include a viscous hydrodynamics and proper initial conditions.
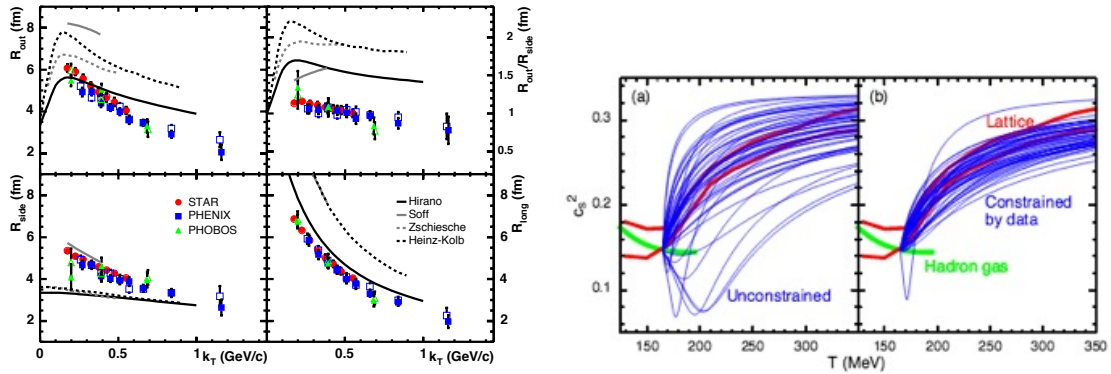
Figure 3.14: Left: The comparison of the hydrodynamics calculation to the experimentally measured HBT radii from the STAR, PHENIX and PHOBOS experiments. Right: Constraining the equation of state by the femtoscopy. Taken from [57].

The systematic femtoscopic measurements provide excellent test of the dynamical evolution of the created system in heavy-ion collision as predicted by the hydrodynamic calculations. Its power is demonstrated in the right panel of Figure 3.14. The speed of the sound c_s^2 controls the expansion of the system created in heavy-ion collisions. The left sub-part of the right panel of Figure 3.14 shows theoretical prediction by hydrodynamical models which are unconstrained by measured HBT radii. As can be seen, the predictions in general do not follow any trend. In case that hydrodynamical predictions are compared to the femtoscopic results, the predictions are constrained, and all of them follow one preferred trend.

3.5 New opportunities in femtoscopy

The first femtoscopic measurements were statistically challenges and hence they had to be performed with the most abundant particles, pions. Therefore the results presented in the previous section come primarily from the $\pi - \pi$ correlations. However the increased luminosity which is achieved nowadays by the RHIC and LHC brings new possibilities in femtoscopy.

3.5.1 Particle interaction measurement

Since the correlation function calculated in Eq. 3.6 depends on the source function and the two-particle relative wave function, the problem can be turned around and the particle interaction can be goal of our study.

Increasing statistics in combination with more detailed knowledge of the spacial and temporal extensions of the source permits to perform such measurement. One of the first such measurements has been recently performed by the STAR [61] when the interaction between two antiprotons has been studied. In this analysis, the scattering length f_0 and effective range d_0 of the antiproton interaction were measured. The scattering length is related to the cross section at low energy limit via

$$\sigma = 4\pi f_0^2. \tag{3.46}$$

For a short range potential, f_0 and d_0 are related to the s-wave scattering phase shift δ_0 and the

collision momentum k by

$$k \cot(\delta_0) \approx \frac{1}{f_0} + \frac{1}{2}d_0 k^2. \tag{3.47}$$

The measured correlation functions with the best fits are shown in the left panel of Figure 3.15. The experimentally measured function was corrected for particle misidentification and residual correlations which are caused by antiprotons from the weak decays of already correlated primary particles. The parameters of the interaction was extracted using the Lednický and Lyuboshitz analytic model [45]. As can be seen in the right panel of Figure 3.15, within systematics errors, the experimentally measured f_0 and d_0 for the antiproton-antiproton interaction are consistent with the ones of the proton-proton interaction.
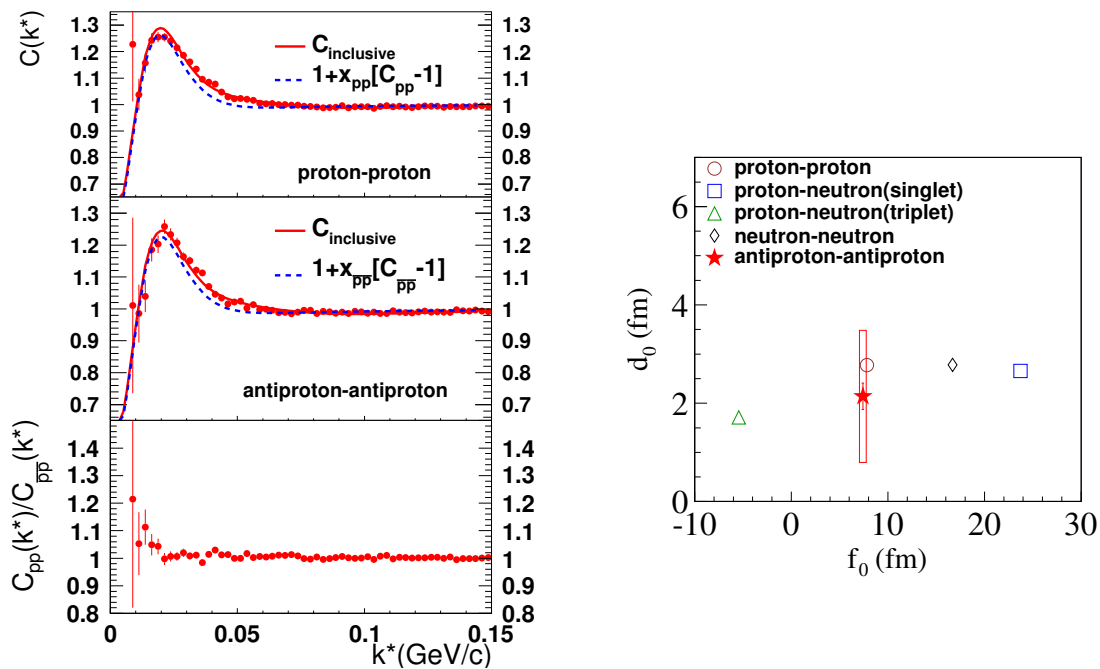
Figure 3.15: Left: Experimentally measured correlation function. Top panel is for proton-proton, middle for antiproton-antiproton and bottom panel presents double ratio of these two functions. Right: The extracted scattering length f_0 and effective range d_0 for the antiproton-antiproton interaction are compared to the parameters of the proton-proton, proton-neutron and neutron-neutron interaction. Taken from [61].

3.5.2   Measurements in the region of a narrow resonance

Increasing statistics have already enabled to perform the first femtoscopic analyses with non-identical interacting particles. In addition to $\pi - \pi$ correlations, such studies can provide a new point of view on the created system in the heavy-ion collisions since the various particle species can be sensitive to different effects and different collision stages. However due to lower abundances of these particles, only one dimensional correlation functions have been usually constructed. A solution to these difficulties can be femtoscopy with pairs of particles which contain a narrow, near-threshold, resonance.

It has been predicted that correlations due to the strong final-state interactions in a system where a narrow resonance is present will be sensitive, in the region of the resonance, to the source size and momentum-space correlations [45]. It is expected that the correlation function will be more sensitive in the region of the resonance where the strength of the correlation should change with the source size r as $\sim r^{-3}$ [45] in comparison with measurements at the very low relative momenta, where the correlation function depends on r^{-2} or r^{-1}. In addition, these measurements will be statistically advantageous, since the two-particle spectra fall rapidly at low relative momenta. Therefore such a measurement can provide complementary information to the measurements at very low relative momenta.

The sensitivity of the correlation function in the region of the resonance have been already observed at low energy experiments. The left panel of Figure 3.16 shows triton - alpha particle correlation function from measurements which were performed for ^{40}Ar-induced reactions on ^{197}Au at energy $E/A = 60$ MeV [62]. The triton - alpha particle correlation function exhibits several sharp structures resulting from a high lying excited state of ^{7}Li which decays into the triton-alpha channel. The theoretical description of such correlation functions can be considerably complicated, nevertheless authors of this analysis [62] made the first estimation. The experimentally constructed deuteron - alpha particle correlation functions, where resonance can be observed, were compared to theoretical correlation function for different source size as is shown in the left panel of Figure 3.16. These functions were predicted by the final-state interaction model and it proved that the correlation function are sensitive to source size in the region of resonance.
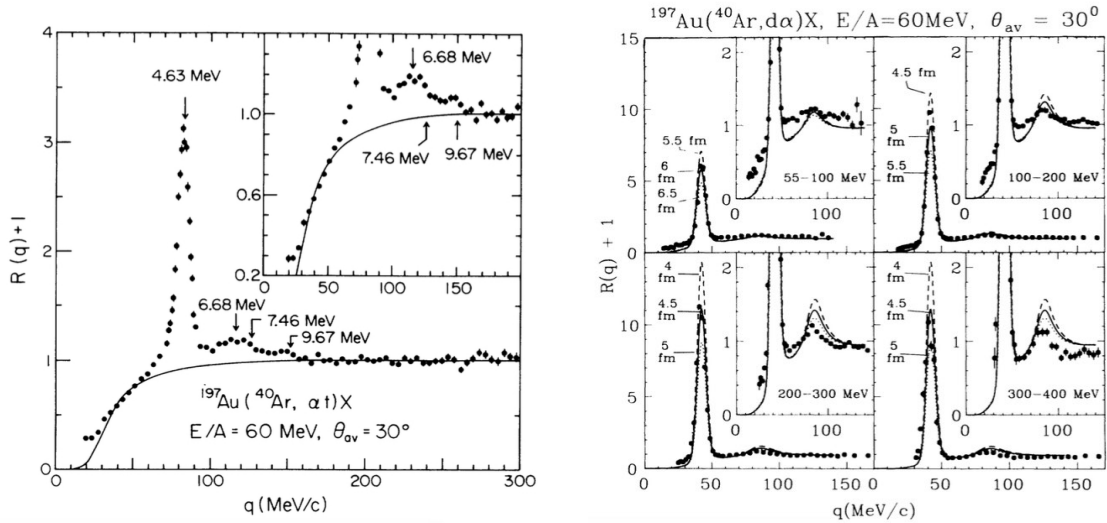
Figure 3.16: Left: Triton - alpha particle correlation function from ^{40}Ar-induced reactions on ^{197}Au at energy $E/A = 60$ MeV. The peaks correspond to excited state of ^{7}Li, which decay into the triton-alpha particle channel. Right: Measured deuteron - alpha particle correlation function are compared to theoretical predictions which takes into account the final-state interaction. Taken from [62].

At high-energy heavy-ion collisions, the similar sharp structure of the correlation function can be also expected. As an example of such function, Figure 3.17 presents the theoretical unlike-sign kaons correlation function calculated by EPOS model. As can be seen, several resonances are visible in the correlation function. In EPOS all resonances, especially the $\phi(1020)$ which is of particular interest for this work are thermally produced. The difference between the thermal production and the previously

mentioned production via the final-state interaction had been widely discussed in [63] and for a case of sudden freeze-out their equivalence had been proved [64].
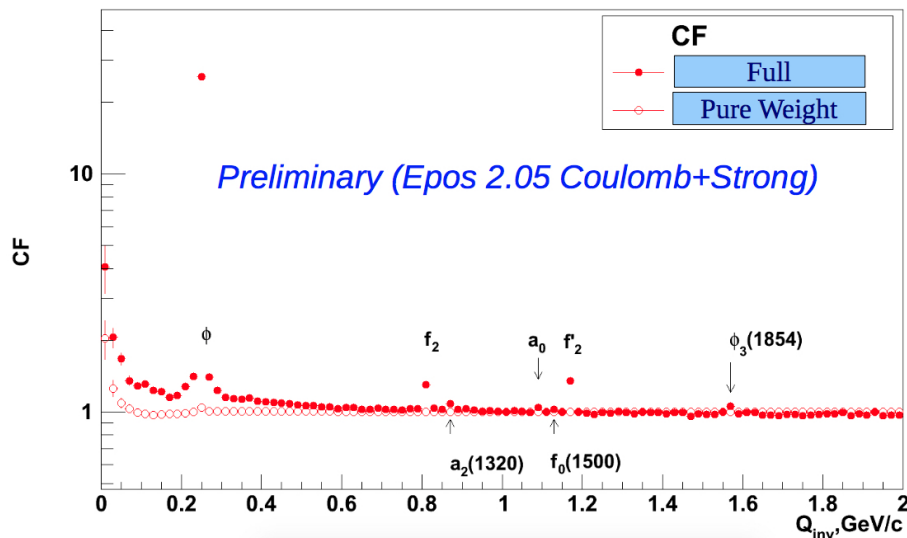
Figure 3.17: Theoretical calculated unlike-sign kaons correlation function calculated by the EPOS. Taken from [62].

The femtoscopy in the region of a narrow, near-threshold, resonance brings challenges for the femtoscopics formalism which has been developed for the measurements at low relative momenta. The classical assumptions such as the smoothness approximation and the equal-time approximation will be pushed to the limits. The approach proposed by Lednický [45] extends the femtoscopic formalisms to higher relative momenta between the two emitted particles in a system where the final-state interaction contains a narrow, near-threshold, resonance. The Lednický's FSI model includes the treatment of the $\phi(1020)$ resonance for unlike-sign kaons correlation function and the $\Xi^*(1530)$ resonance for unlike-sign $\pi - \Xi$ correlation. The Lednický model has so far been only to results

The Lednicky model has so far been compared only to results from unlike-sign kaon correlation measured by NA49 collaboration [65] and the preliminary STAR results on $\pi - \Xi$ correlations [66], [67].

In the analysis of $\pi - \Xi$ correlations, the three-dimensional correlation functions have been decomposed in the spherical harmonics. The advantage of such method is the fact that the correlation function [68]

$$C(k^*, \theta, \varphi) = \sqrt{4\pi} \sum_{l=0}^{\infty} \sum_{m=-l}^{l} A_{l,m}(k^*) Y_{l,m}^*(\theta, \varphi), \tag{3.48}$$

is linear combination of the coefficients $A_{l,m}(k^*)$ and the spherical harmonics $Y_{l,m}^*(\theta, \varphi)$. All space-time information about the source is then encoded into the coefficients. While the monopole - $A_{0,0}$ - describes the size of the source, the shift of the mean emission points in out direction is controlled by the dipole $A_{1,1}$.

The preliminary STAR results are presented in the right panel of Figure 3.18. Although this analysis was statistically challenged, the extracted correlation function shown a strong centrality dependence in the region of the resonance. Figure 3.18 shows the comparison of the coefficients to the model predictions. It can be seen that none of the used model, FSI, blast-wave neither HYDJET++, did not successfully describe the measured data.
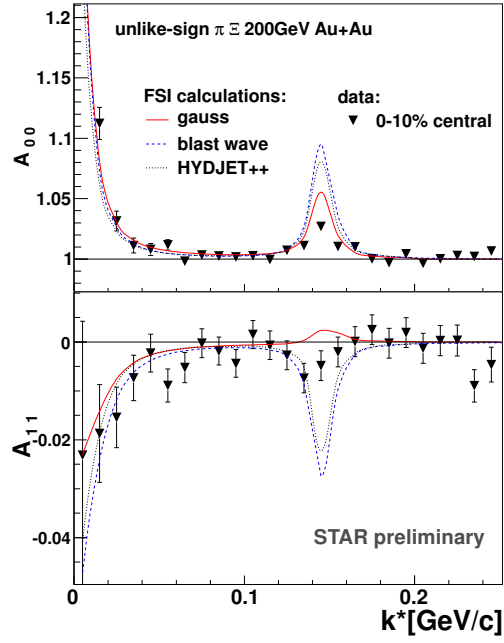
Figure 3.18: Experimental $\pi - \Xi$ correlation function decomposed into spherical harmonics is compared to FSI calculations with gauss, blast-wave and HYDJET++. Taken from [69].

DATA ANALYSIS - CONSTRUCTION OF CORRELATION FUNCTION

The analysis presented in this work is deal with the femtoscopics correlations of unike-sign kaon, including the narrow $\phi(1020)$ resonance. The $\phi(1020)$ resonance with the lifetime of ~ 42 fm/c is characterized by the decay width $\Gamma = 4.3$ MeV and the decay momentum in the rest frame $k^* = 126$ MeV/c. A detailed description of the analysis procedure is presented in this chapter. Consequently the data set, event selection, track selection and kaon identification are described. All these cuts lead to construction of two-particle correlation function that is shown in the last section of this chapter.

4.1 Data set

The data presented in this work was taken in the year 2011 in Au+Au collisions at $\sqrt{s_{\mathrm{NN}}} = 200$ GeV with the minimum bias trigger by the STAR experiment at RHIC. The minimum bias trigger required a coincidence between the East and West ZDC and VPD detectors, respectively. The data are protected against the pile-up. This pile-up occurs when there is such a high rate of collisions that the TPC and other detectors do not have enough time to readout all tracks before the next collision takes place. Therefore it could happen that event would contain a contamination of particles coming from the subsequent events. The detailed information about the used data set in STAR notation is listed below.

- Trigger: vpd-zdc-mb-protected

- Offline Trigger ID: 350003, 350013, 350023, 350033, 350043

- Production: P11id (library: SL11d)

- FileCatalog Command: `trgsetupname=AuAu200_production_2011,filetype=daq_reco_MuDst,` `filetype=daq_reco_MuDst,filename`$\sim$`st_physics,collisions=AuAu200,sanity=1,` `available=1,tpx=1,tof=1,storage!=HPSS`

- Number of Events (before event cuts): $\sim$730M

The total number of $\sim$730M events entered the analysis was on which the event cuts were then applied.

4.2 Event selection

In order to select events that occurred in the center of the TPC, a cut on the position of the primary vertex along the beam direction (z-axis) was applied. The events were required to have $|V_z| < 30$ cm, where V_z is the z-coordinate of the primary vertex position measured by the TPC. Such event cut assures that detector acceptance does not change significantly with V_z. The primary vertex position is reconstructed from TPC tracks. Even though, the events are protected against the pile-up which removes large part of the effect, an additional cut on this phenomenon was also applied. This selection criteria uses that fact that the V_z can be calculated from the measured tracks in the TPC as well as by VPD detector that determines V_z of the event on which was triggered. Therefore, the difference between the vertex position measured by the TPC and VPD detectors $\left|V_z - V_z^{VPD}\right|$ were required to be smaller than 5 cm. Both of applied event selection criteria are shown in Figure 4.1.
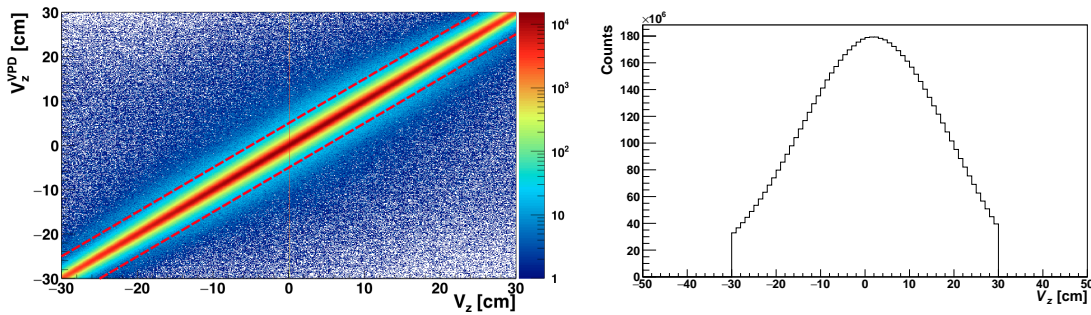
Figure 4.1: Left: The distribution of the z-coordinate of the primary vertex position measured by the TPC versus the z-coordinate of the primary position on which VPD triggered. The red lines represent applied cut. Right: The distribution of the z-coordinate of the primary vertex position after applied cut.

4.2.1 Centrality definition

There are multiple possible ways how to experimentally define event centrality. The most common method is via the multiplicity of the charged particles. Other observables which are connected to the unobserved impact parameter are the signal from the both of the ZDC detectors and the number of hits recorded by the ToF detector. Correlation between the multiplicity of tracks in TPC and the signal from the ZDC detectors and the ToF Tray multiplicity, respectively is shown in Figure 4.2.

In case that the centrality definition is based on multiplicity, the number of charged tracks in TPC, it brings some disadvantages. One of them is a possible dependence of the multiplicity on the primary vertex position. The standard method for removal of this dependency used in the STAR experiment is via a `StRefMultCorr class`. This method is based on the Glauber model and uses information about the ZDC coincidence rate and the z-coordinate of the primary vertex position. The corrected multiplicity is then calculated as

$$\texttt{refMult\_corr} = (\texttt{reftMult\_raw} + \texttt{gRandom} \rightarrow \texttt{Rndm}()) \cdot \texttt{correction\_luminosity} \cdot \texttt{correction\_V_z},$$

where the `correction_V_z` is the correction on the z-coordinate of the primary vertex position and
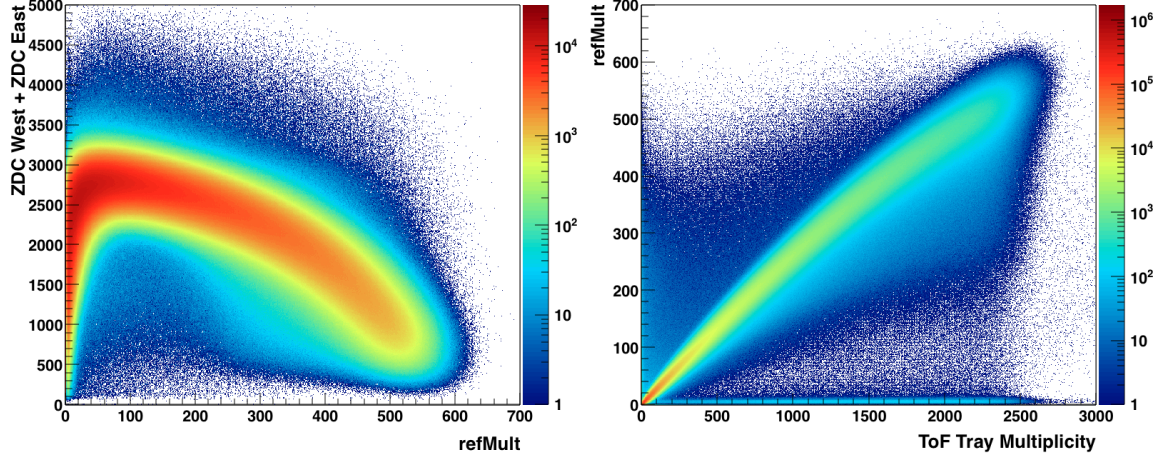
Figure 4.2: Left: The correlation between the measured signal by ZDC detectors and TPC multiplicity. Right: The distribution of the reference multiplicity and the ToF tray multiplicity.

`correction_luminosity` is related with the ZDC coincidence rate. These correction are calculated in a following way:

$$\texttt{correction\_V}_\texttt{z} = \frac{\texttt{zpar0} + \texttt{zpar7}}{\texttt{zpar0} + \texttt{zpar1} \cdot \texttt{V}_\texttt{z} + \texttt{zpar2} \cdot \texttt{V}_\texttt{z}^2},$$

and

$$\texttt{correction\_luminosity} = \frac{1}{1 + \frac{\texttt{lpar1}}{\texttt{lpar0}} \cdot \frac{\texttt{zdcCoincidenceRate}}{1000}}.$$

The values of the parameters $lpar_i$ and $zpar_i$ can differ for each recorded event and have to be experimentally obtained. The values of these parameters in the `StRefMultCorr class` which was used in the presented analysis are from STAR internal study for Run11. Then `StRefMultCorr class` allows to recalculate and correct the measured (uncorrected) multiplicity. With the newly obtained corrected multiplicity the centrality can be determined based on the corrected multiplicity. Table 4.1 lists the multiplicity boundaries used in the centrality definition.

centrality	Multiplicity	centrality	Multiplicity	centrality	Multiplicity
0-5%	>466	30-35%	>156	60-65%	>31
5-10%	>396	35-40%	>125	65-70%	>22
10-15%	>335	40-45%	>98	70-75%	>15
15-20%	>281	45-50%	>76	75-80%	>10
20-25%	>234	50-55%	>58		
25-30%	>193	55-60%	>43		

Table 4.1: Multiplicity boundaries used in the centrality definition.

For the analysis presented in this work, events are divided into 5 bins corresponding to 0-5%, 5-10%, 10-30%, 30-50% and 50-75% centrality. Figure 4.3 shows the multiplicity distribution of the corrected multiplicity divided into these 5 centralities bins. This binning is used for construction of

one-dimensional correlation function. Since the first two bins are statistically limited they are later, in construction of the three-dimensional correlation function, merged into one bin.
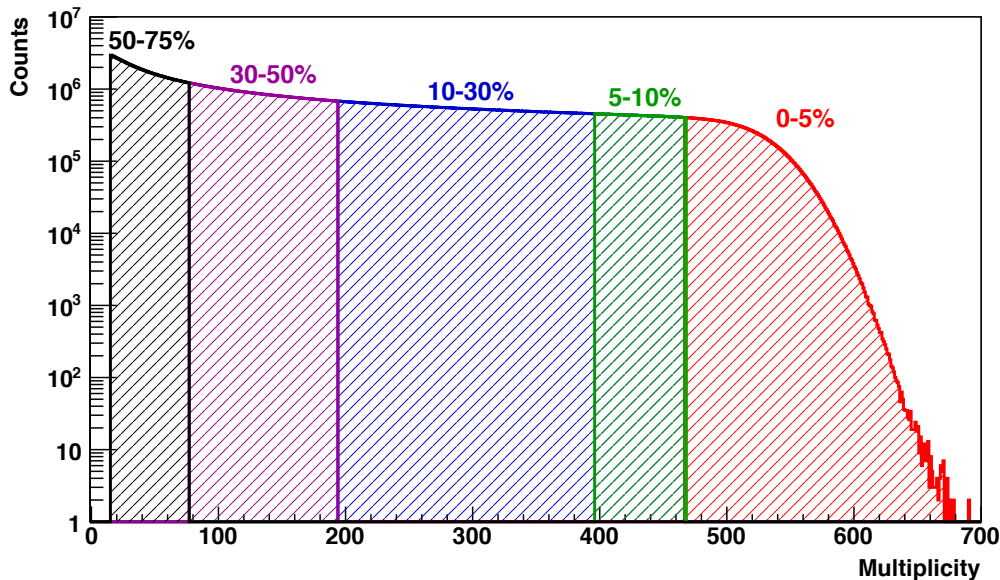
Figure 4.3: The corrected multiplicity distribution and corresponding centrality.

In order to remove all non-femtoscopics correlations and to obtain uncorrelated two-particle distribution which is used as the denominator of the experimentally constructed correlation function, mixed pairs from similar events are required. The mixed pairs are constructed in such a way that each particle from one event is mixed with all particles from events belonging to a sub-class of similar events. The division into the subclasses of similar events is done according to the position of the z-coordinate of the primary vertex and uncorrected multiplicity. In total, events were divided into 10 bins in the primary vertex position (1bin per 6 cm) and 7 bins in the multiplicity distribution (1 bin per 100 units of multiplicity).

4.3 Particle selection

4.3.1 Track quality cuts

From the events satisfying the event selection criteria good-quality tracks, particle trajectories, were selected. Only primary tracks with pseudorapidity $|\eta|$<1.0 were accepted. Such cut makes sure that the measured particles fall into the detector acceptance. Then primary tracks were required to have the distance of the closest approach to the primary vertex smaller than 3 cm. The application of these track quality cuts is shown in Figure 4.4. This way only primary particles were used.

Another *standard* cut which is usually used for the track quality selection is based on the minimal number of reconstructed hits in TPC and the criterion on the ratio of fitted hits to maximum number of hit points. The purpose of these quality cuts is to reduce effects such as track merging or imprecisely reconstructed tracks. Track were required to have minimal 15 fit points in TPC and the ratio of fitted hits to maximal possible hits in TPC was more than 0.52 . There are also criteria which were used
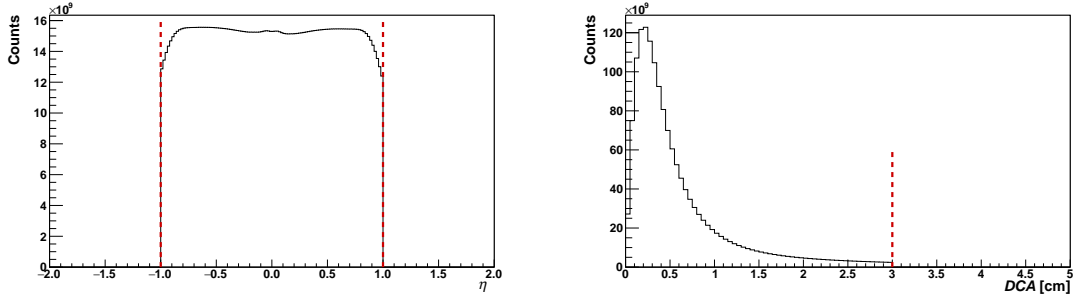
Figure 4.4: Left: The distribution of the pseudorapidity of tracks. Right: The distribution of the DCA of tracks. In both cases, the red dotted lines represents applied cuts.

by tracking system in order to associate track in TPC with a hit in the ToF.

4.3.2 Kaon identification

From the tracks which passed the quality cuts described in the previous section, kaon tracks are selected. In presented analysis, the kaon identification is based on a cut on specific ionization energy loss in the TPC and a cut on mass squared measured by the ToF. These selection criteria are described in more detail below. Since the TPC enables to identify particles with the transverse momentum p_T larger than 0.15 GeV/c, in addition a cut on the transverse momenta of the reconstructed tracks was applied. Hence only tracks with $p_T > 0.15$ GeV/c which fulfilled both of the identification cuts were identified as kaons.

TPC cut

As was already discussed in the Chapter 2, charged particles are identified via the specific energy loss $\mathrm{d}E/\mathrm{d}x$ in the TPC gas. Due to a finite resolution of the TPC, the measured energy loss deviates from the theoretically expected value calculated using Bichsel function [34]. In case that the measured distribution of the specific energy loss has a Gaussian distribution with the mean value determined by the theoretical value of $\mathrm{d}E/\mathrm{d}x^{theo}$ and with the standard deviation σ_K, the normalized energy loss for kaon can be defined as

$$n\sigma_K = \ln\left(\frac{\mathrm{d}E/\mathrm{d}x^{meas}}{\mathrm{d}E/\mathrm{d}x^{theo}}\right)/\sigma_{\mathrm{d}E/\mathrm{d}x}, \qquad (4.1)$$

where $\mathrm{d}E/\mathrm{d}x^{meas}$ is the measured value of the energy loss. The normalized energy loss is scaled by the resolution $\sigma_{\mathrm{d}E/\mathrm{d}x}$.

In this work, the tracks were required to have $n\sigma_K$ in the range between -3 and 3. As can be seen in Figure 4.5, by applying this cut the hadron contamination can be eliminated up to momentum $p < {\sim}0.55$ GeV/c. However there is a significant presence of the pions at negative $n\sigma_K$ and protons at positive $n\sigma_K$ for higher momenta. The reason for this contamination is the fact that areas of the specific energy loss of pions, kaons and protons overlap for higher momenta as can be seen in Figure 2.7. In order to remove the remaining hadron contamination, the ToF cut had to be used as shown in the right panel of Figure 4.5
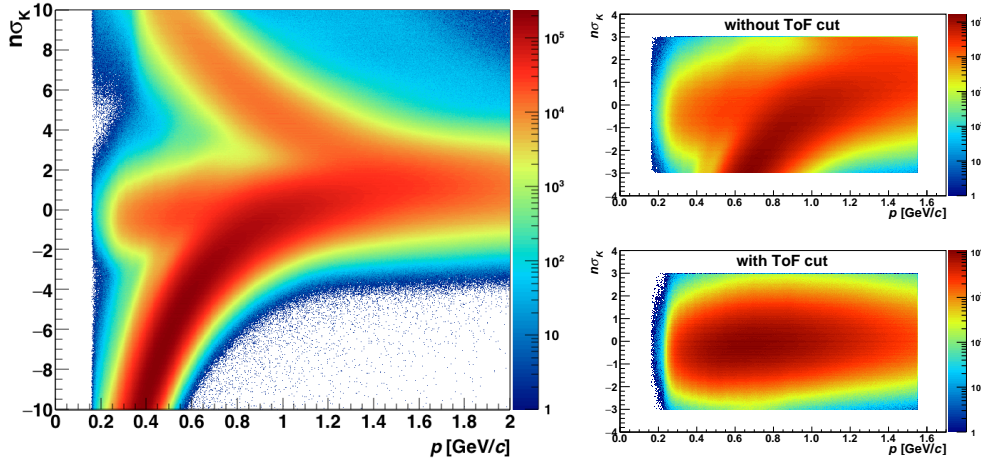
Figure 4.5: Left: The distribution of the $n\sigma_K$ versus momentum p of tracks in TPC. Right, Top: The distribution of $n\sigma_K$ versus momentum p without ToF cut. Right, Botton: The distribution of $n\sigma_K$ versus momentum p with ToF cut.

ToF cut

The ToF measures the time of flight β. When this information is combined with the measured momentum in TPC, the particle mass m can be calculated by Eq. 2.4. As can be seen in the right panel of Figure 4.5, in comparison with TPC, the ToF enables to separate charged kaons from other hadron up to momentum ~ 1.55 GeV/c. Therefore tracks were required to have momenta in the range $0.15 < p < 1.55$ GeV/c. Since for kaons $m_K^2 = 0.2437$ GeV$^2/c^4$, the last identification cut requires the track to have the mass squared in the range $0.21 < m^2 < 0.28$.

    The applied identification selection criteria enable to obtain very pure sample of kaons as is shown in Figure 4.6.
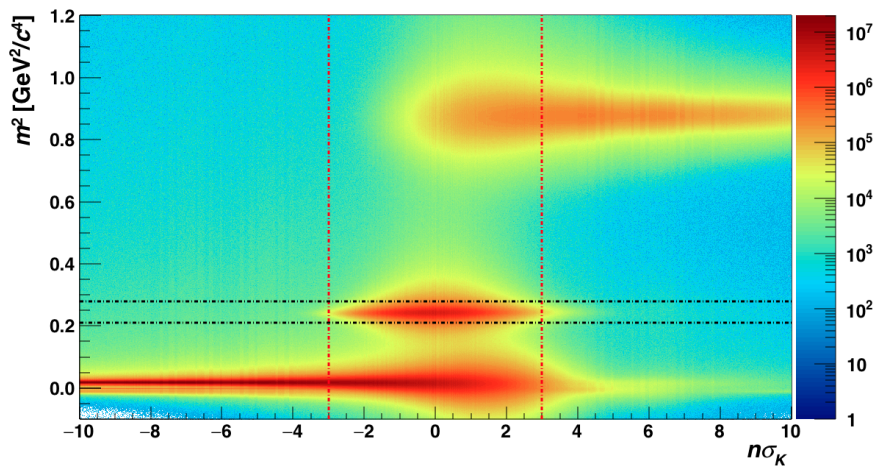
Figure 4.6: The distribution of mass square of particle vs $n\sigma_K$. Red lines represent $n\sigma_K$ cut and black lines represent cut on particle mass.

4.4   Pair cuts

Despite very clean kaon sample the two particle distribution is affected by detector defects arising from the tracking reconstruction imperfections. The influence of these imperfections exhibits at the low relative momentum q_{inv}, where the measured correlation function is the most sensitive to space-time extents of the source. These effects are track splitting and track merging. In the following two subsections, the cuts which eliminate these effects will be described and tested.

4.4.1   Track splitting

The case, when track from single particle is reconstructed as two very close tracks, is called the track splitting [17]. The measured tracks then have very similar momenta, hence their relative momentum q_{inv} is small. Therefore the track splitting causes an enhancement of pairs at low relative momentum q_{inv}. In order to remove these split tracks the locations of the hits for each track in the pair in the pad-rows of the TPC were studied. It was performed via the so-called "Splitting level" (SL) calculated as

$$SL = \frac{\sum_i S_i}{NHits_1 + NHits_2},$$
(4.2)

where

$$S_i = \begin{cases} +1 \ldots \text{one track leaves a hit on pad-row} \\ -1 \ldots \text{both tracks leave a hit on pad-row} \\ 0 \ldots \text{neither track leaves a hit on pad-row,} \end{cases}$$
(4.3)

where i is the pad-row number of the TPC, and $NHits_1$ and $NHits_2$ are the total number of hits associated to each track in the pair. The main principle of the splitting level is shown in Figure 4.7, where the SL is calculated for four possible cases. As can be seen in Figure 4.7, for two clearly distinct tracks the splitting level takes value equal to -0.5. On the other hand, in case of the possibly split track the splitting level is equal to unity.
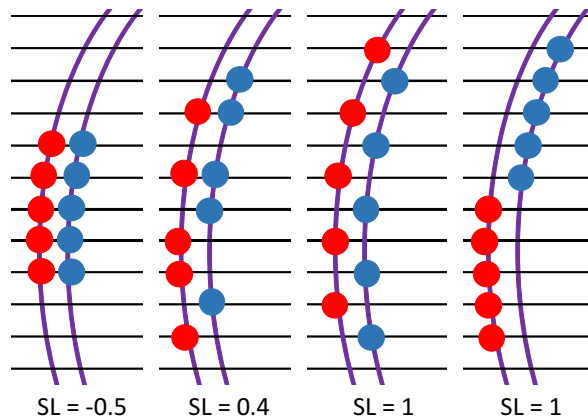
Figure 4.7: The description of the anti-splitting cut, which is applied on four possible cases. Red circles are hits assigned to one track, blue circles are assigned to the other.

To remove split tracks, every pair has to fulfilled anti-splitting cut. The value of the anti-splitting cut is determined from the experimentally measured correlation function for different SL. Figure 4.8 shows like-sign kaon correlation functions constructed for different values of the SL. As can be seen the effect of the track splitting is not present. The absence of the splitting tracks was also confirmed for unlike-sign kaon correlation functions.
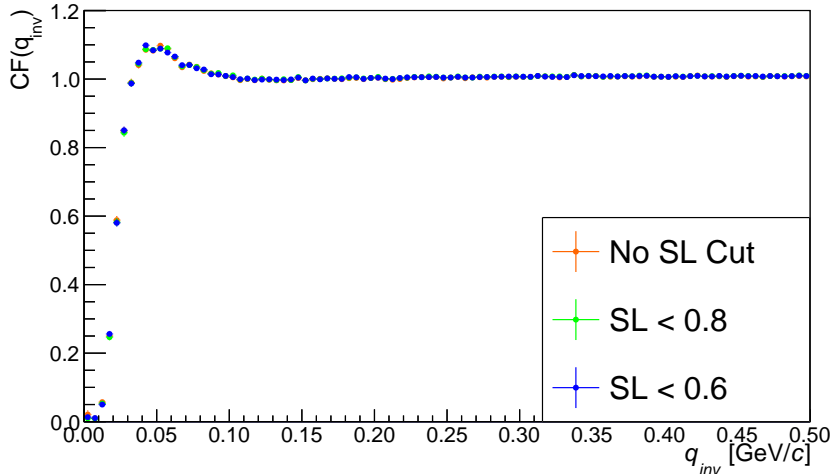
Figure 4.8: One-dimensional like-sign kaon correlation function for different values of SL.
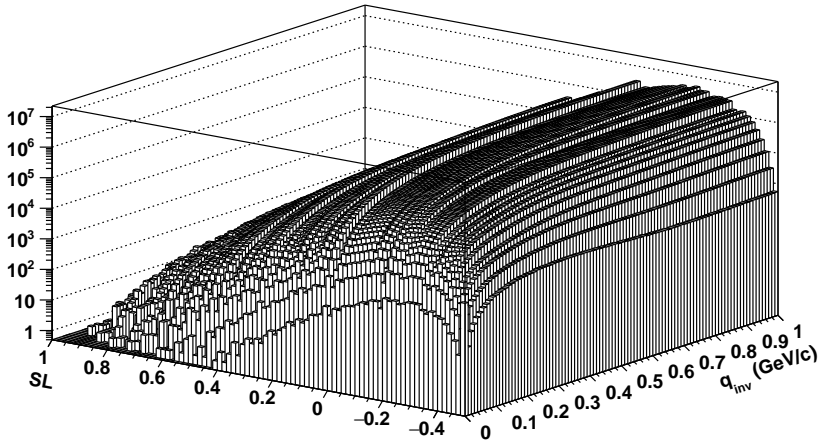
Figure 4.9: The distribution of real pairs versus relative momentum q_{inv} and splitting level SL.

As a cross-check of no influence of the track splitting, the distribution of real pairs versus relative momenta q_{inv} and splittting level were constructed. From the first femtoscopic measurements [17], one would expect to observe the enhancement at low q_{inv} and at higher value of the SL. However, Figure 4.9 does not show any enhancement. Similarly, no presence of the track splitting has been recently reported in [70]. One of the possible explanation is the selection criterion on the number of hits in TPC. In the past, track reconstruction was performed with lower number of the hits in TPC and therefore the track splitting was more frequent. Nevertheless thanks to high available statistics

it was possible to apply *standard* SL < 0.6 cut to real and mixed pairs and remove whatever possible evidence of the track splitting.

4.4.2   Track merging

Besides of track splitting, it can happen that two particles with similar momenta are reconstructed as only one track. It happens when two particles leave hits in the TPC so close to each other that it is beyond the resolution of the read-out pads in the TPC. Two hits are considered merged if the probability of separating them is less than 99% [17]. To determine the maximum fraction of merged hits which eliminates the effect of track merging, the correlation function were constructed for different values of the fraction of the merged hits. Figure 4.10 shows the one-dimensional like-sign correlation functions for different values of the maximum fraction of merged hits. As can be seen, the correlation function is affected by the fraction of merged hits. This effect can be reduces, when the pairs were required to have a fraction of merged hits smaller than 10%.
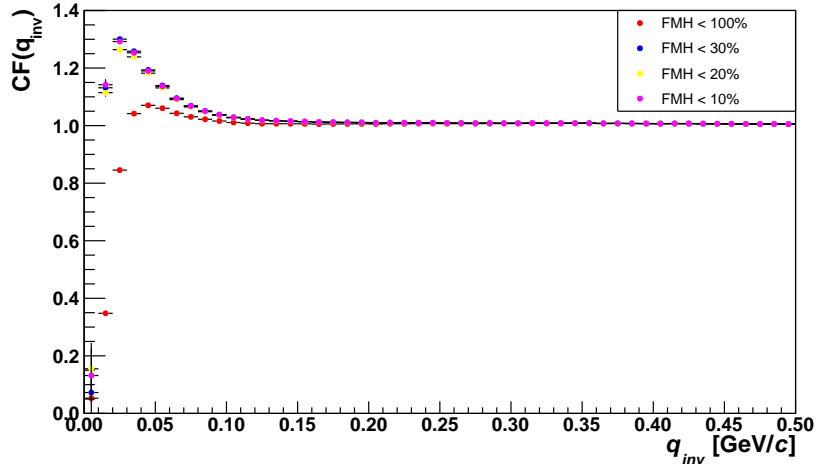
Figure 4.10: One-dimensional like-sign correlation function for different values of fraction of merged.

4.4.3 k_T cuts

Finally, the last applied cut is on the average pair transverse momentum k_T defined as

$$k_T = \left(\frac{\boldsymbol{p_1} + \boldsymbol{p_2}}{2} \right)_T , \tag{4.4}$$

where $\boldsymbol{p_1}$ and $\boldsymbol{p_2}$ are the momenta of the first and second particle in the given pair, respectively. As was already discussed, homogeneity regions are expected to depend on the pair transverse momentum. Hence such cut enables to change the size of the measured volume at the constant centrality and temperature of the system. The average transverse momentum can be rewritten in the term of the transverse mass of the pair as

$$m_T = \sqrt{k_T^2 + m_0^2}, \tag{4.5}$$

where m_0 is the particle's mass. This relation is suitable for study of the m_T dependence of the measured HBT radii which reflects the dynamics of the systems.

In our analysis, the pairs were required to have the average transverse momenta in the range from 0.05 GeV/c to 1.25 GeV/c. This range was consequently divided into four bins: 0.05-0.35, 0.35-0.65, 0.65-0.95 and 0.95-1.25 GeV/c. Figure 4.11 shows the k_T distribution of real like-sign pairs.
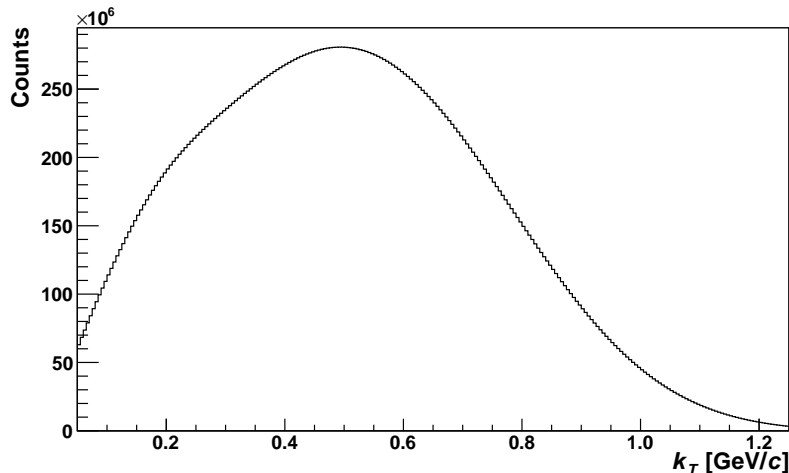
Figure 4.11: The distribution of real pair transverse momentum.

4.5   Raw one-dimensional correlation functions

Finally, the correlation function $CF(q_{inv})$ can be constructed as a ratio of the correlated two-particle distribution from the same event, $N_{same}(q_{inv})$ and the uncorrelated two-particle distribution from mixed events, $N_{mixed}(q_{inv})$:

$$CF(q_{inv}) = \frac{N_{same}(q_{inv})}{N_{mixed}(q_{inv})} = \frac{real\,pairs}{mixed\,pairs}. \tag{4.6}$$

Figure 4.12 presents results on the unlike-sign kaons correlation function from Au+Au collisions at $\sqrt{s_{\mathrm{NN}}} = 200$ GeV. The left panel of Figure 4.12 presents unlike-sign correlations for 4 k_T bins and centrality 30-50%. Centrality dependence of unlike-sign correlation functions, which are integrated over k_T is shown in the right panel of Figure 4.12. While at the low q_{inv} the attractive Coulomb interaction and strong interaction in s-wave can be observed, in the region of $q_{inv} \sim 0.25$ GeV/c the strong interaction in p-wave via $\phi(1020)$ resonance in FSI is present.

As can be seen, the correlation function is sensitive to the source size. In particular, a strong dependence on collisions centrality and on the pair k_T is observed in the resonance region. The height of the ϕ peak decreases significantly with the centrality as well as with k_T.

Similarly also the like-sign correlation functions were constructed, separately for positively and negatively charged pairs of kaons. The like-sign kaon correlation functions are also sensitive to the space-time extents as shown Figure 4.13. At the low q_{inv}, the repulsive Coulomb interaction which competes with Bose-Einstein statistics can be observed. However the region of the low q_{inv} is strongly effected by the statistical uncertainties resulting from the rapidly falling two-particle spectra at low relative momenta.
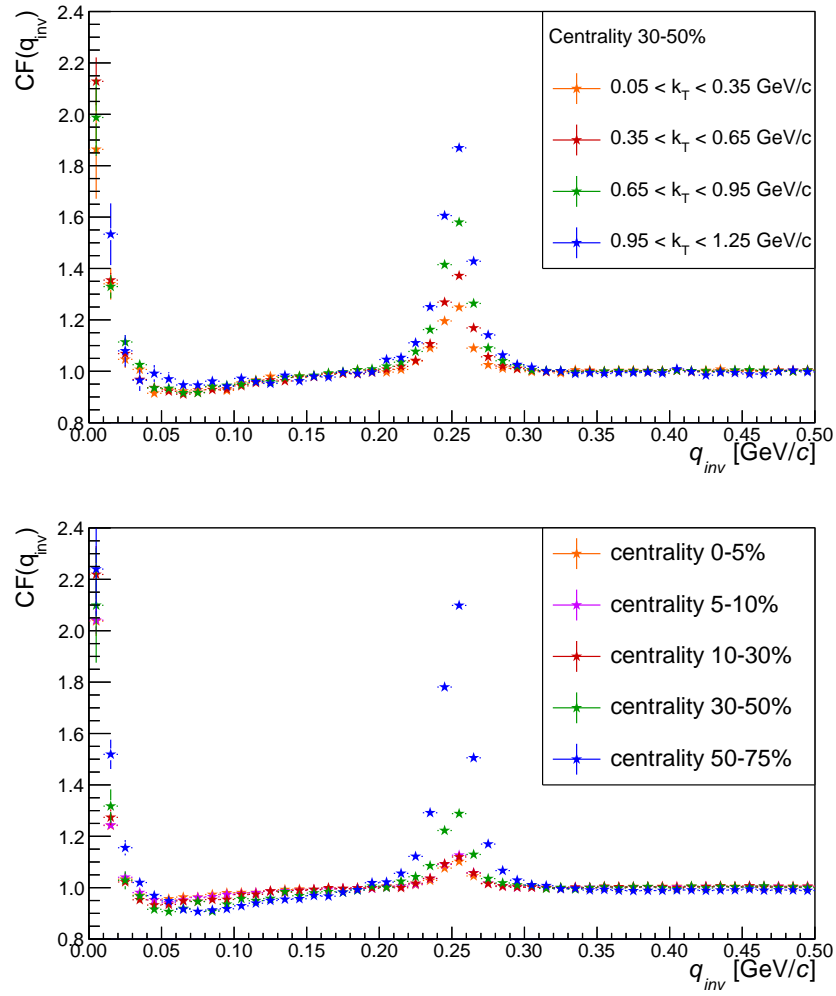
Figure 4.12: Top: One dimensional unlike-sign correlation functions for centrality 10-30% and for 4 k_T bins. Bottom: One dimensional unlike-sign correlation functions for 5 centralities.
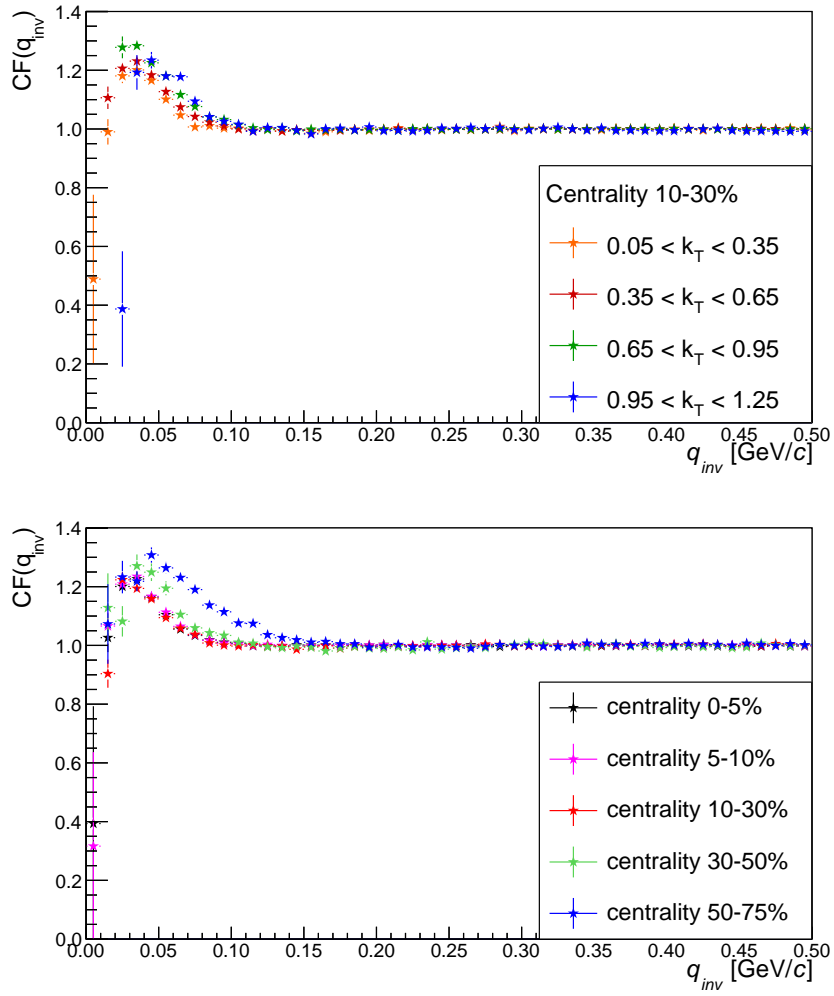
Figure 4.13: Top: One dimensional like-sign correlation functions for centrality 10-30% and for 4 k_T bins. Bottom: One dimensional like-sign correlation functions for 5 centralities.

CHAPTER
FIVE

CORRECTIONS OF EXPERIMENTAL CORRELATION FUNCTIONS

Even when very strict selection criteria have been applied, there are additional effect that can alter the strength of the correlation function. They can decrease the strength of the experimental correlation function and affect the extracted HBT radii. One of the main sources of these imperfection is the particle misidentification, when selected the kaon was not actually a kaon. Another effect is related to finite detector momentum resolution.Corrections for both of these effects are introduced below. In this chapter the Coulomb correction required for fitting like-sign correlation functions together with the fitting procedure is also discussed.

5.1 Purity correction

Although the single particle cuts were strict and required identification by the ToF in combination with the TPC, it can not be ruled out that some pions or protons could be inaccurately identified as kaons. The misidentified particles then weakened the measured correlation function.Therefore experimental correlation function has to be corrected for misidentification of particles. Since the correlation function depends on the relative momentum q_{inv}, the purity correction denoted as PairPurity has to be calculated as a sum of the product of the single particle purities weighted by the probability that two given particles with momenta $\boldsymbol{p_1}$ and $\boldsymbol{p_2}$ form pair with the relative momentum q_{inv}. Mathematically it can be expressed as

$$PairPurity\left(q_{inv}\right) = \sum_{\boldsymbol{p_1},\boldsymbol{p_2}} Purity\left(\boldsymbol{p_1}\right) Purity\left(\boldsymbol{p_2}\right) Prob\left(q_{inv}|\boldsymbol{p_1}\boldsymbol{p_2}\right). \tag{5.1}$$

The purity of the particle with momentum $\boldsymbol{p_i}$ is calculated as

$$Purity\left(\boldsymbol{p_i}\right) = Purity_{TPC}\left(\boldsymbol{p_i}\right) Purity_{ToF}\left(\boldsymbol{p_i}\right), \tag{5.2}$$

where $Purity_{TPC}\left(\boldsymbol{p_i}\right)$ is the purity of particles which fulfilled $n\sigma_K$ cut at the given momentum $\boldsymbol{p_i}$, while the purity of particles with momentum $\boldsymbol{p_i}$ which met requirement on their mass squared is referred as $Purity_{ToF}\left(\boldsymbol{p_i}\right)$. The PairPurity has been studied on fraction of the whole sample, ca ~ 150M events.

5.1.1   TPC purity

The TPC purity of the particle sample which fulfilled all selection criteria but without applying the $n\sigma_K$ cut was extracted from the $n\sigma_K$ distributions as a function of particle momenta p. Figure 5.1 shows example of the two $n\sigma_K$ distributions of positively charged particles with momenta $0.59 < p < 0.61$ GeV/c and $0.99 < p < 1.01$ GeV/c for centrality 10-30%. While for the lower momenta, the three Gaussians distribution are clearly observed, with increasing momenta the Gaussians are merged and finally only one Gaussian remains. The Gaussian centered at zero corresponds to kaons. This Gaussian is gradually contaminated by the pion Gaussian coming from the negative value of the $n\sigma_K$ and for very high momenta also by the proton Gaussian from the right side. Such behavior is in agreement with presented Figure 4.5 where $n\sigma_K$ as a function of momenta p was shown.

The purity was calculated as the ratio of the kaon Gaussian integrated from -3 to 3 from which the pion's and proton's contributions were subtracted and multi Gaussian also integrated from -3 to 3 expressed as

$$Purity_{TPC} = \frac{\int_{-3}^{3} N_K\left(\sigma\right) \mathrm{d}\sigma - \int_{-3}^{3} N_\pi\left(\sigma\right) \mathrm{d}\sigma - \int_{-3}^{3} N_p\left(\sigma\right) \mathrm{d}\sigma}{\int_{-3}^{3} N_{all}\left(\sigma\right) \mathrm{d}\sigma}, \tag{5.3}$$

where $N(\sigma)$ is Gaussian distribution. The boundaries of the integral are equal to the range of the applied $n\sigma_K$ cut.
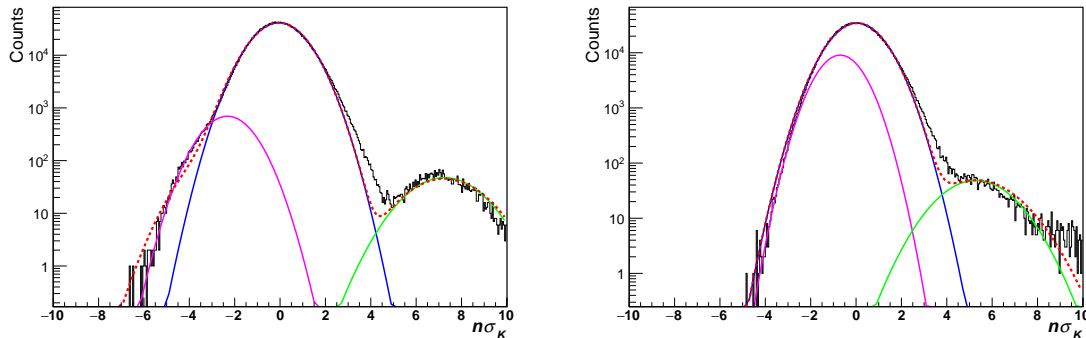
Figure 5.1: The distribution of $n\sigma_K$ for $0.59 < p < 0.61$ GeV/c and $0.99 < p < 1.01$ GeV/c for positively charged kaons for centrality 10-30%. Blue line represents kaon Gaussian, magenta line represents pion Gaussian and green line if for proton Gaussian. Their sum is represented by red dotted line.

It is apparent that the fitting becomes complicated with increasing particle momenta p since the Gaussians start to overlap. In order for the fits to convergence, some of the fit parameters their value have to be constrained. There are two possible ways how to limit parameters of the pion Gaussian. The first is based on the theoretical calculation, when the distance between the mean of pion and kaon Gaussian for given momentum is calculated from Bichsel function [34]. However such approach does not take into account detector effects. In our analysis, the identification cuts were changed to select pions and the mean of the pion Gaussian distribution was studied as a function of $n\sigma_K$. This additional study provided information on how to restrict the maximal and minimal values of the mean of the pion Gaussian at the moment when it was overlapped by the kaon Gaussian.

Figure 5.2 shows extracted purity as a function of particle momentum for positively charged kaons for centrality 10-30%. As can be seen, the contaminations of pions and protons is removed by the

ToF cut hence the TPC purity is very high, around $\sim 98\%$ and slightly decreases with increasing p. Similarly high purity was also observed for all centralities. The same applies for negatively charged kaons.
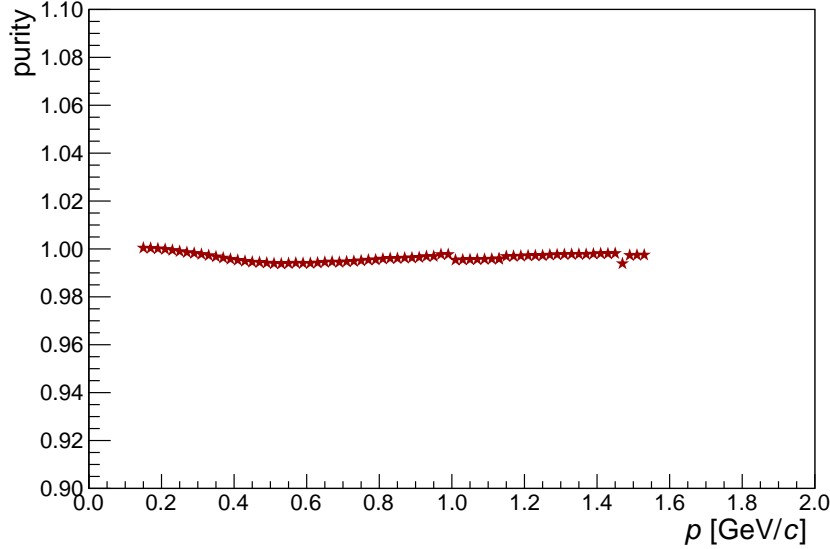
Figure 5.2: The TPC purity as a function of momentum p.

5.1.2 ToF purity

Similar method was employed to extract the purity of the kaon sample for the ToF cut. The ToF purity was extracted from the mass squared distribution. Unlike in previous cases, now the distributions were fitted by Student's t-probability distribution defined as

$$\mathcal{N}\frac{\Gamma\left(\frac{\nu+1}{2}\right)}{\sqrt{\nu\pi}\Gamma\left(\frac{\nu}{2}\right)}\left(1+\frac{(x-\mu)^2}{\nu}\right)^{-\frac{\nu+1}{2}}, \tag{5.4}$$

where ν is the variance, μ is the mean and $\mathcal{N}$ is the constant. All of these parameters were free parameters of the fit. Figure 5.3 shows the distribution of the mass squared for $0.95 < p < 1.03$ GeV/c and $1.43 < p < 1.51$ GeV/c for positively charged kaons for centrality 30-50%. As can be seen in Figure 5.3, now the mean of the distribution is well-defined in contrast to the previous TPC cases. The means should be equal to squared values of pion and kaon masses, respectively. The disadvantage of this procedure is that even after fitting there is some remaining residual background that was fitted by the third-order polynomial functions. In our analysis, it is assumes that the contamination from protons can be neglected.

The ToF purity as a function of the momentum p is shown in Figure 5.4. Similarly as for the TPC purity, also the ToF purity is very high.

5.1.3 Probability matrix

Finally the PairPurity is calculated according to Eq. 5.1 where the probability that two given particles with momenta p_1 and p_2 form pair with the relative momentum q_{inv} is determined by the probability
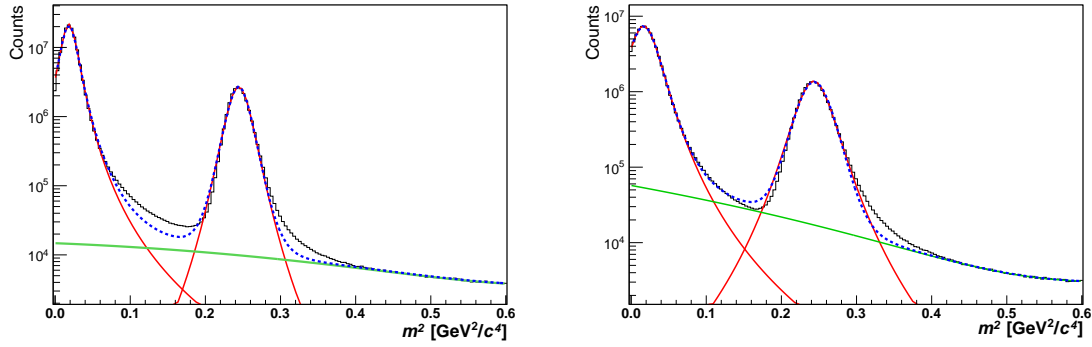
Figure 5.3: The distribution of the mass squared of positively charged kaons for $0.95 < p < 1.03$ GeV/c and $1.43 < p < 1.51$ GeV/c for centrality 30-50% measured by ToF. Red lines represent pion and kaon Student's t-probability distributions. Blue line is for Multi-Student's t-probability and the background is represented by the green lines.
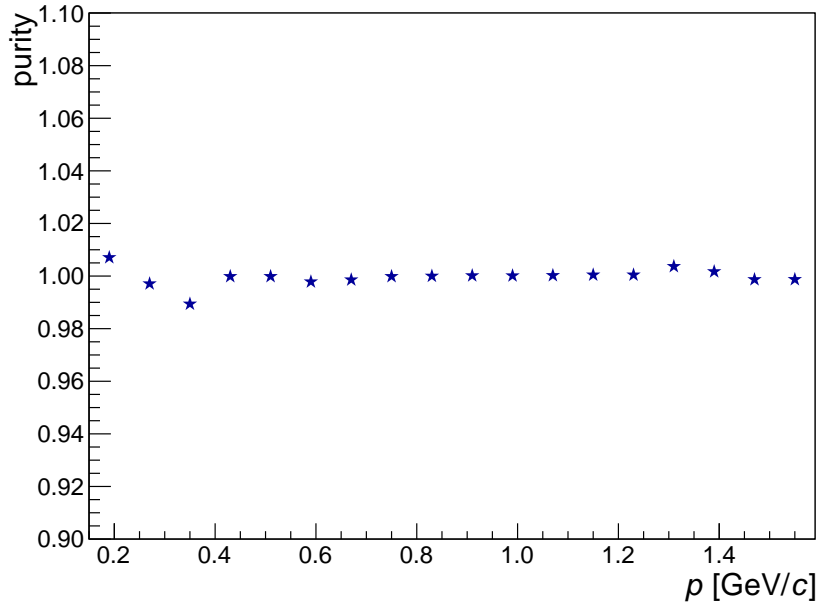
Figure 5.4: The ToF purity as a function of momentum p.

matrix obtained from measured data. Figure 5.5 shows probability matrix for positively charged pairs of kaons for centrality 10-30%.

The PairPurity for positively charged kaons for centrality 30-50% is shown in Figure 5.6. As can be seen, the purity is very high. Similarly high purity was measured for all centralities as well as for negatively charged kaons, even for unlike-sign kaons. Hence the applied correction on raw correlation function $CF^{raw}(q_{inv})$ via relation

$$CF^{corr}(q_{inv}) = \frac{CF^{raw}(q_{inv}) - 1}{PairPurity(q_{inv})} + 1 \tag{5.5}$$

was rather small.
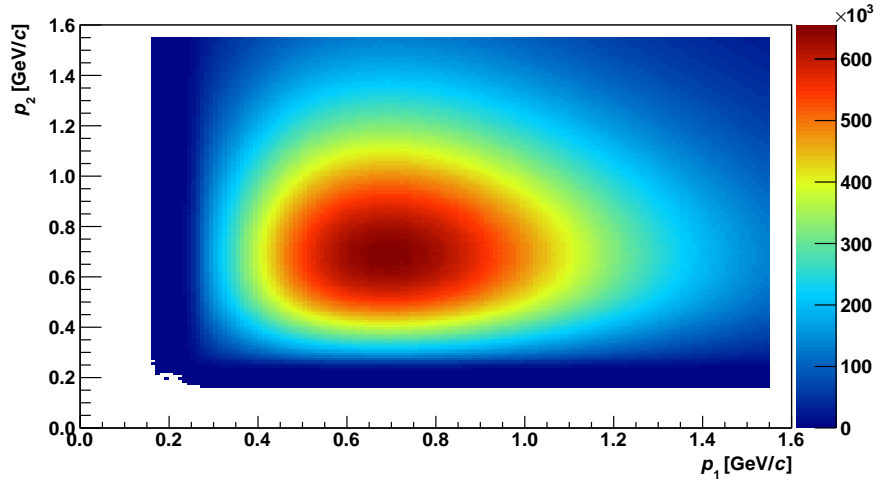
Figure 5.5: The probability matrix distribution of two particles with momenta p_1 and p_2 forming pair with the relative momentum q_{inv}.
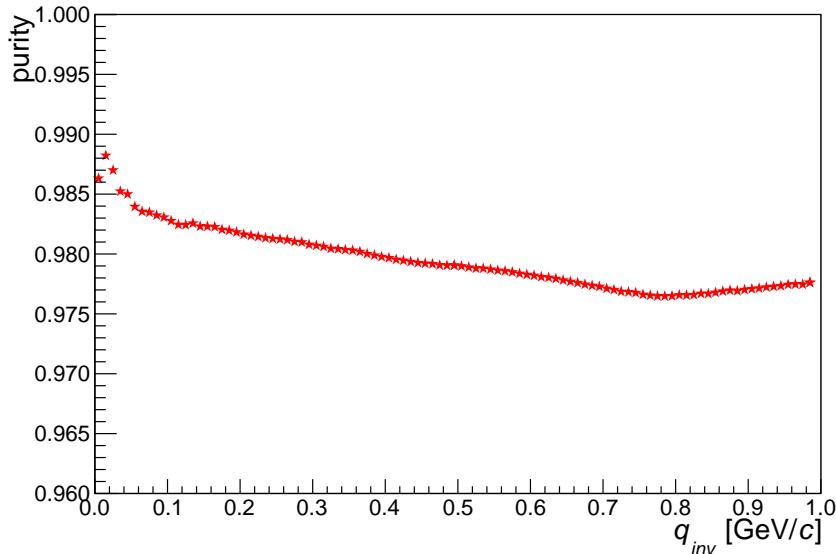
Figure 5.6: The PairPurity for positively charged kaons for centrality 30-50%.

5.2   Coulomb correction of like-sign correction function and fitting procedure

In case of the unlike-sign correlation function, there is no analytical parametrization that could be used for fitting. Nevertheless these functions can be fitted numerically. One of the most sophisticated fitting program enabling fitting without the knowledge of the exact form of the correlation function is CorrFit [71] developed by Adam Kisiel. In the presented work, the CorrFit has not been employed so far due to its inherent difficulty. In future it is possible that it will be used.

Instead of unlike-sign correlation function, the like-sign correlation function can be fitted. Hence

the source parameters such as the sizes of the source and the λ parameter can be obtained so far and used for calculation of the unlike-sign correlation function. The kaons are charged particles, hence the correlation function can not be simply fitted by Eq. 3.31 or Eq. 3.32 because of the dominant Coulomb interaction at the low q_{inv}. The Coulomb interaction is repulsive for like-sign kaons and causes a suppression of the correlation function at the low q_{inv}.

In presented analysis the Bowler-Sinyukov fitting procedure was used [72]. This method is based on separation of the Coulomb interaction from the Bose-Einstein correlations. Then the one-dimensional correlation function, which is normalized to unity at large q_{inv} is fitted to:

$$CF\left(q_{inv}\right) = \left[\left(1 - \lambda\right) + \lambda K_{Coul}\left(q_{inv}\right)\left(1 + e^{-q_{inv}^2 R_{inv}^2}\right)\right]\mathcal{N}, \tag{5.6}$$

where $\mathcal{N}$ is the normalization and K_{Coul} is the Coulomb factor defined by Eq. 3.23. The free parameters of the fit are R_{inv}, λ and $\mathcal{N}$. The fit region is for $q_{inv} < 0.4$ GeV/c.

The normalization has to be calculated in the region where there is no correlations. Therefore the first estimation of the normalization was calculated in the range from $q_{inv} = 0.6$ GeV/c to $q_{inv} = 1.0$ GeV/c. In this region, the measured correlation function is already flat since the Bose-Einstein statistics as well as Coulomb interaction are dominated at the low q_{inv}.

In case of the three-dimensional correlation function, the fitting function is expressed as

$$CF\left(q_o, q_s, q_l\right) = \left[\left(1 - \lambda\right) + \lambda K_{Coul}\left(q_{inv}\right)\left(1 + e^{-q_o^2 R_o^2 - q_s^2 R_s^2 - q_l^2 R_l^2}\right)\right]\mathcal{N}. \tag{5.7}$$

Also here the correlation function is corrected by the Coulomb factor that depends on q_{inv}. However, in our cases, due to low statistics, the normalization $\mathcal{N}$ was fixed on the value calculated at the region $0.3 < q_i < 0.5$ GeV/c. Similarly to the fitting of one-dimensional correlation function, the fitting range is from $q_i = 0$ GeV/c to $q_i = 0.4$ GeV/c.

In both cases, the best fit is determined on the principle of maximum log-likelihood minimization function [73] defined as

$$\chi^2 = -2\left[A\ln\left(\frac{C\left(A + B\right)}{A\left(C + 1\right)}\right) + B\ln\left(\frac{A + B}{B\left(C + 1\right)}\right)\right], \tag{5.8}$$

where C is the ratio of the numerator A to denominator B. Although no significant difference between the log-likelihood method and the classical χ^2 fitting was observed during fitting one-dimensional correlation function, the implementation of this procedure was motivated by the nonconvergence of the χ^2 method in fitting three-dimensional correlation functions. This procedure is more adequate for lower statistics, where the χ^2 test converges with difficulty. The divergence of the χ^2 is caused by the fact that the ratio of two Poisson distribution is not Poisson distribution itself, especially when taking the ratio of small numbers [44]. The log-likelihood method is described in [73] where the full derivation of the minimization function can be found.

The systematic errors related with the fitting procedure were studied by varying fit range and the normalization region.

The results of fitting, the extracted HBT radii and the λ parameters, are intentionally not presented in this section since the correlation functions are still uncorrected on the momentum resolution. However, the procedure providing correction for momentum resolution needs a first estimate of the HBT radii and the λ parameters. This procedure will be presented in following section. Only after application of all corrections on experimental correlation functions, the final HBT radii and the λ parameters will be extracted and presented.

5.3   Momentum resolution correction

Due to the finite particle momentum resolution of the TPC, there is a systematic uncertainty in the determination of $\boldsymbol{q_{inv}}$ which leads to decrease of the strength of the measured correlation function. The effect is stronger in low q_{inv} hence it has significant influence on the extracted radii. Therefore these effects of the momentum resolution have to be corrected.

The magnitude of this effect can be estimated by Monte-Carlo simulations when the simulated particle is embedded into the real event and passed through whole reconstruction process. Such simulation can provide information about the momentum resolution and its influence on the measurable variables.

The components of the real momentum $\boldsymbol{p}$ can be expressed in the term of the measured transverse momentum p_T, the azimuthal angle φ and the polar angle θ as

$$
\begin{aligned}
p_x &= p_T \cos\left(\varphi\right) \\
p_y &= p_T \sin\left(\varphi\right) \\
p_z &= \frac{p_T}{\tan\left(\theta\right)}.
\end{aligned}
\tag{5.9}
$$

However, these components are reconstructed with following deviations:

$$
\begin{aligned}
\delta p_x &= p_x \frac{\delta p_T}{p_T} - p_y \delta\varphi \\
\delta p_y &= p_y \frac{\delta p_T}{p_T} + p_x \delta\varphi \\
\delta p_z &= p_z \frac{\delta p_T}{p_T} + p_T \frac{\delta\theta}{\sin^2\left(\theta\right)}.
\end{aligned}
\tag{5.10}
$$

where the $\frac{\delta p_T}{p_T}$, $\delta\varphi$ and $\delta\theta$ are during the data analysis unknown and have to be extracted from the simulations. Here the kaon embedding for run of 2011 was used. The Monte Carlo simulations contains in total 144 164 positive kaons and 145 383 negative kaons.

Figure 5.7 shows the extracted distribution of the $\frac{\delta p_T}{p_T}$, $\delta\varphi$ and $\delta\theta$ as the function of the p_T. These distributions were then parametrized by the Gaussian and its mean and width were studied as the function of the p_T. In Figure 5.8 there are the mean and width of the $\frac{\delta p_T}{p_T}$, $\delta\varphi$ and $\delta\theta$, respectively. The data are fitted with the same functions which were used in [69], [17] and [74]. While the mean of the $\frac{\delta p_T}{p_T}$ is fitted with

$$
f\left(p_T\right) = a + b p_T^{\alpha} + c p_T,
\tag{5.11}
$$

the others are fitted with

$$
f\left(p_T\right) = a + b p_T^{\alpha},
\tag{5.12}
$$

where a, b, c and α are the free parameters of the fits. These functions do not have any deeper physical motivation, they just describe well the asymptotic behavior at the low and high p_T. It has been shown that the momentum resolution does not depend on the collision centrality and is almost similar for positively and negatively charged kaons. Therefore it was possible to merge both datasets and study the effects of the momentum resolution for all centralities.

To estimate the effect of the momentum resolution, two correlation function have to calculated. While the first is the ideal one, the second on is constructed from particles with their momenta randomly smeared. The method how to construct these functions is described below.

First of all, the source was parametrized by a Gaussian in the CMS with a parameter R_{inv}. Here the individual R_{inv} were those extracted from fitting like-sign correlation function discussed in the
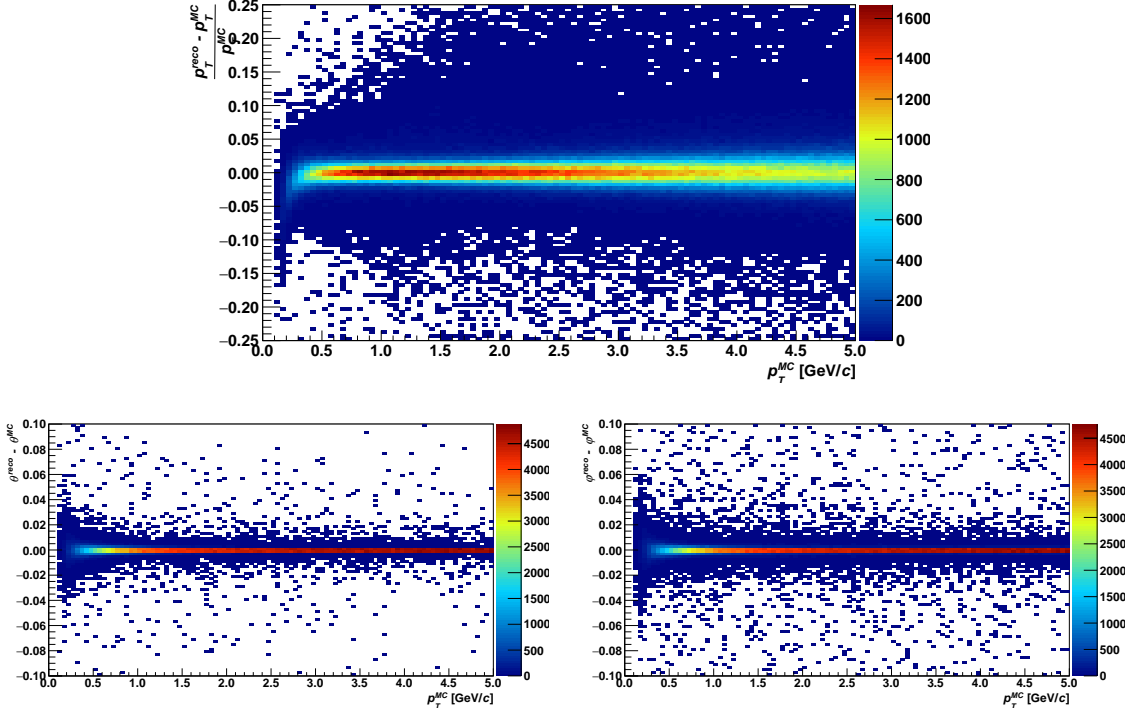
Figure 5.7: Monte Carlo simulations for kaons. Top: The distribution of $\frac{\delta p_T}{p_T}$ as a function of p_T. Bottom, Left: The distribution of $\delta\theta$ as a function of p_T. Bottom, Right: The distribution of $\delta\varphi$ as a function of p_T

previous section. Hence the distribution of the position for x, y and z-direction is Gaussian. The momentum distribution of kaons was obtained from analyzed data from different events. Each pair in the numerator in the correction function was weighted according to the following formula

$$weight = (1 - \lambda) + \lambda K_{Coul}(q_{inv})\left(1 + e^{-q_{inv}^2 R_{inv}^2}\right), \tag{5.13}$$

where the λ parameter was the same one as obtained from fitting like-sign correlation function (see Figure 6.2). The second part of the weight factor $K_{Coul}(q_{inv})\left(1 + e^{-q_{inv}^2 R_{inv}^2}\right)$ was calculated by the Lednický-Lyuoboshitz model. These pairs then formed the numerator of the correlation function. Now the theoretical correlation function can be constructed. In comparison with experimentally measured correlation function, such constructed function is not influenced by any detector effects.

To obtain function that corresponds to the measured one, the momenta of particles had to be smeared according to the extracted momentum resolution (see Figure 5.8). Then the pairs are weighted with the same factor (Eq. 5.13) which was already used for unsmeared pairs. This procedure causes that the pairs with smeared momenta and the given weight have slightly different q_{inv}. This function was denoted as the smeared one and include the effect of momentum resolution. The left panel of Figure 5.9 shows the clean and smeared correlation function constructed by the process discussed above. As can be seen the effect momentum resolution is dominant in the region of the low q_{inv}, especially in the region where the Coulomb interaction is dominant. In Figure 5.9 the smeared correlation is also compared to the experimentally measured one. The observed small disparity in the shape of the correlation function can come from using the Bowler-Sinyukov method. The measured function is fitted by Bowler-Sinyukov approximation, while the calculated function was obtained from
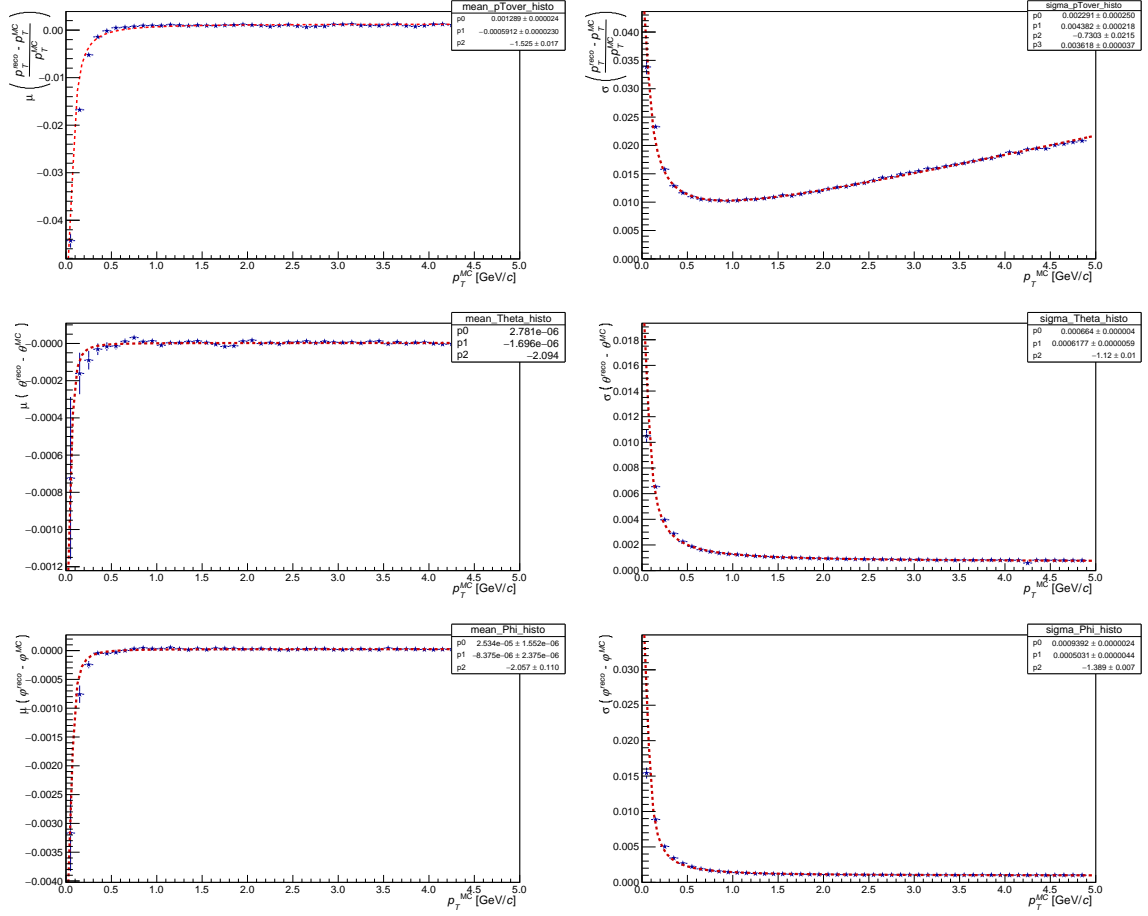
Figure 5.8: The μ and σ of the Gaussian distribution of the $\frac{\delta p_T}{p_T}$, $\delta\varphi$ and $\delta\theta$ as a function of the transverse momentum.

the exact Lednický-Lyuboshitz analytical model.

To quantify the magnitude of the momentum resolution on the correlation function, the correction factor is constructed as

$$K\left(q_{inv}\right) = \frac{CF^{ideal}\left(q_{inv}\right)}{CF^{smear}\left(q_{inv}\right)} = \frac{\frac{A\left(\boldsymbol{p}_1^{idea}, \boldsymbol{p}_2^{idea}\right)}{B\left(\boldsymbol{p}_1^{idea}, \boldsymbol{p}_2^{idea}\right)}}{\frac{A\left(\boldsymbol{p}_1^{smear}, \boldsymbol{p}_2^{smear}\right)}{B\left(\boldsymbol{p}_1^{smear}, \boldsymbol{p}_2^{smear}\right)}}, \tag{5.14}$$

where the CF^{clean} and CF^{smear} are the ideal and smeared correlation function, respectively. Example of the correction factor for like-sign kaon correlation function for centrality 30-50% and $0.35 < k_T < 0.65$ GeV/c is shown in the right panel of Figure 5.9.

In order to remove the effect of the momentum resolution on experimentally measured correlation function $CF^{raw}\left(q_{inv}\right)$ and to obtain corrected experimental function $CF^{corr}\left(q_{inv}\right)$, the correction factor is applied as

$$CF^{corr}\left(q_{inv}\right) = CF^{raw}\left(q_{inv}\right) K\left(q_{inv}\right). \tag{5.15}$$

The same correction is also used in the case of the three-dimensional correlation function.

Such corrected correlation functions can be refitted by the same method as was described in the previous section. In our analysis, the effect of this correction is an increase on the HBT radii between
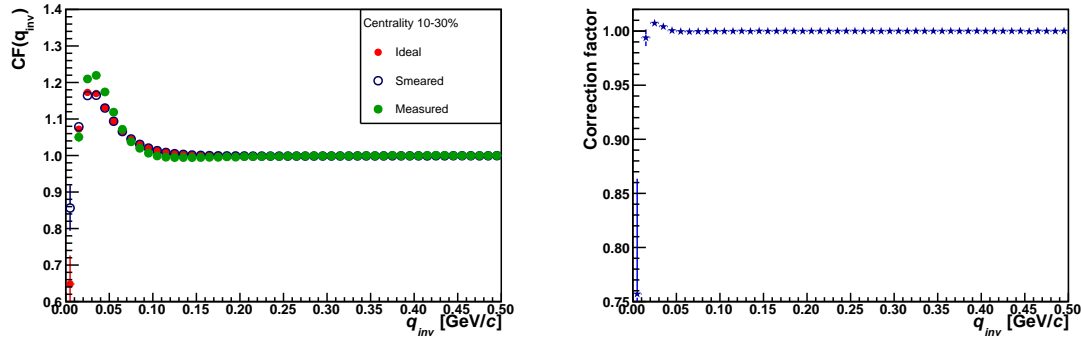
Figure 5.9: Left: The smeared correlation function is compared to the clean theoretical function and the experimental correlation function. Right: The correction factor as a function of q_{inv}.

5% and under up to 10% for the highest k_T bin. In case of the largest changes of the HBT radii, this method can be used iteratively until the moment when the difference of newly extracted radii and the ones used for calculation is smaller than a required value. However this iterative method can be significantly time consuming.

One of the possible improvements which will be performed in the future is parametrization the source by the three Gaussian: R_o, R_s and R_l.

5.4 Cross-check of correlation function sensitivity on detector acceptance

The unlike-sign kaons correlation function contains a significant peak in region of $q_{inv} \sim 0.252$ GeV/c. This peak corresponds to strong interaction in p-wave between unlike-sign kaons via resonance in FSI. Since the q_{inv} is directly connected with the invariant mass M_{inv} by

$$q_{inv} = \sqrt{M_{inv}^2 - 4m_K^2}, \tag{5.16}$$

where m_K is kaon mass, it is clean that this peak is really $\phi(1020)$ resonance with mass $m_\phi = 1.019$ GeV/c^2 [75]. The $\phi(1020)$ resonance [75] with the lifetime of ~ 42 fm/c is characterized by the decay width $\Gamma = 4.3$ MeV and the decay momentum in the rest frame $k^* = 126$ MeV/c. The most likely hadronic decay mode is via unlike-sign kaons channel with branching ratio of 49.2%. Figure 5.10 shows the invariant mass M_{inv} of $\phi(1020)$ resonance as a function of its transverse momenta p_T.

In the *standard* femtoscopics measurements when the correlation function is sensitive to the pertinent physics at the low q_{inv}, the detector acceptance has no influence on the correlation function.

In the presented analysis the effect of the detector acceptance on the height of the resonance had been tested. The height of peak should scale with the ratio of number of kaons from the decayed $\phi(1020)$ resonance to number of all kaons. Hence any detector influence should be canceled out. In order to test this effect, the analysis was performed for two different values of the cut on particle's pseudorapidity. In the first case, the kaons were required to have pseudorapidity η from -1 to 1. The same cut was used in the whole presented analysis. The second cut was more strict and was set on $-0.25 < \eta < 0.25$. It made sure that fewer kaons passed this cut and hence fewer kaons originated from the decay of the $\phi(1020)$ resonance. The left panel of Figure 5.11 shows raw signal of the $\phi(1020)$ after background subtraction. As can be seen, different cuts provides different raw yield of ϕ mesons.
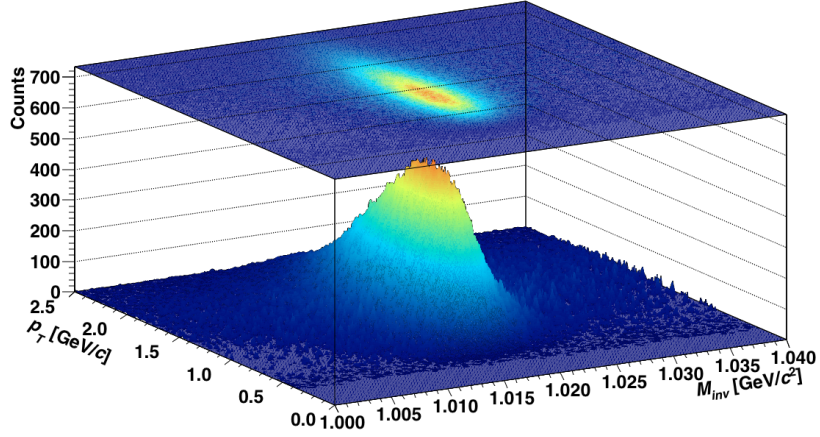
Figure 5.10: The invariant mass M_{inv} of $\phi(1020)$ resonance as a function of its transverse momentum p_T.

The same pairs that had been used for calculating invariant mass were also used for construction of the correlation function. The constructed correlation function in Figure 5.11 clearly demonstrates that in both cases the constructed correlation function is the same even though the number of kaons coming from $\phi(1020)$ resonance differs significantly.
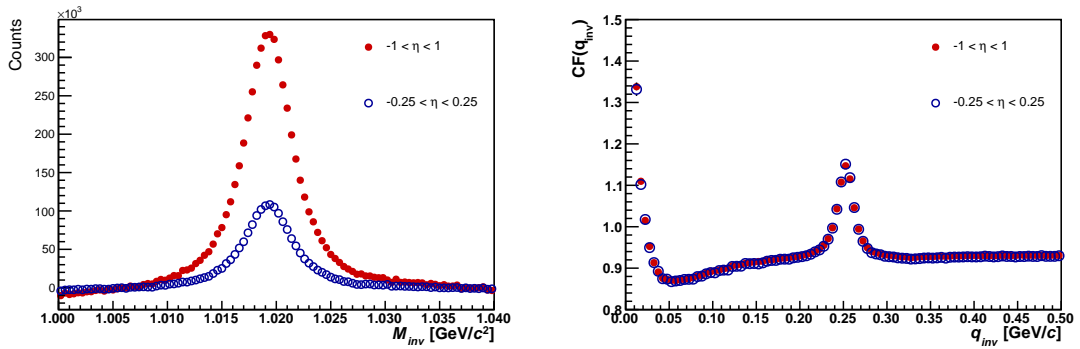
Figure 5.11: Cross-check of correlation function sensitivity on the detector acceptance. Left: The invariant mass M_{inv} of $\phi(1020)$ resonance for 2 different cut on the pseudorapidity. Right: The unlike-sign kaon correlation functions for 2 different cuts on the pseudorapidity.

CHAPTER

SIX

RESULTS

In the previous two chapters the construction of experimental correlation function and applied corrections were discussed. In this chapter the corrected correlation functions are studied in detail.

In the first part of this chapter the results from like-sign kaon correlation function are presented. The like-sign correlation function is used to extract space-time extents of the source. Using the obtained radii it is possible to compare the unlike-sign kaon correlation functions to Lednický model [45]. This model contains treatment of the $\phi(1020)$ resonance due to the final-state interaction. A detailed study of sensitivity of the unlike-sign kaon correlation functions in the region of the $\phi(1020)$ resonance is presented. The experimental correlation functions are also compared to model predictions from different models. Finally, three-dimensional unlike-sign correlation functions are presented.

6.1 Like-sign kaon correlation function

The measured raw like-sign kaon correlation functions were corrected for misidentification of particle and momentum resolution. While the purity correction was applied according to Eq. 5.5, the effect of the momentum resolution was restored via Eq. 5.15. Then the one-dimensional corrected correlation functions were fitted by Eq. 5.6. Figure 6.1 shows example of one-dimensional correlation function for $0.35 < k_T < 0.65$ GeV/c and centrality 10-30%. The left panel of Figure 6.1 presents the corrected correlation function for positively charged kaons and the correlation function constructed for the negatively charged kaons is shown in the right panel of Figure 6.1. The lines represents the best fits to the data by using Eq. 5.6. As can be seen, in all cases the fits well describe the experimentally measured and corrected correlation functions.

Results from fits of correlation function for different centralities and k_T bins are presented in Figure 6.2. Here the λ parameter, source radius R_{inv} and the normalization factor $\mathcal{N}$ are shown as a function of the centrality and pair transverse momentum k_T.

As can be seen the source radii R_{inv} increase with the centrality. The falling of the R_{inv} with the pair transverse momentum k_T qualitatively agrees with the effects expected from a system undergoing a transverse expansion where pairs with the larger transverse momentum are emitted from a smaller effective source than the pairs with the smaller k_T, as it was already discussed in the Chapter 3. The behavior of the λ parameter is not monotonic. In most cases the λ parameter slightly increases for two lower k_T bins and then decreases.
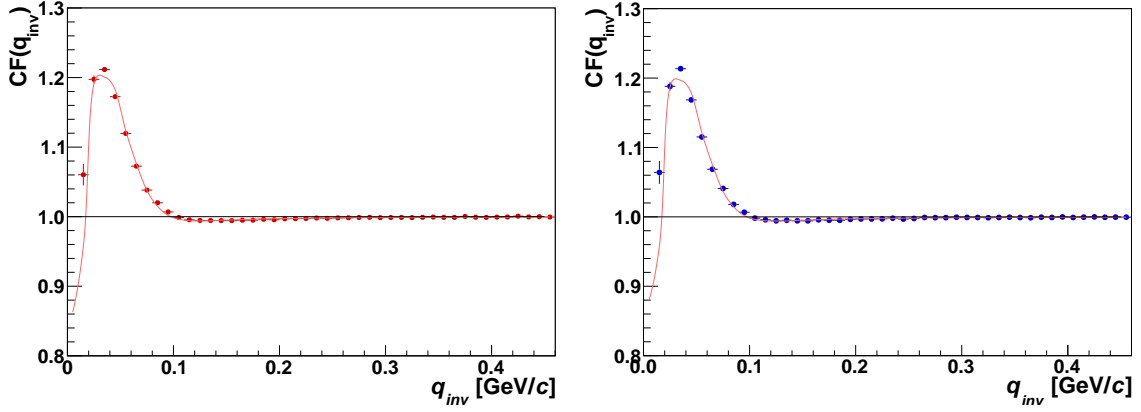
Figure 6.1: One dimensional like-sign correlation function for positive (left) and negative (right) kaons for centrality 10-30% and $0.35 < k_T < 0.65$ GeV/c. The lines represent the best fit to the data by using Eq. 5.6.
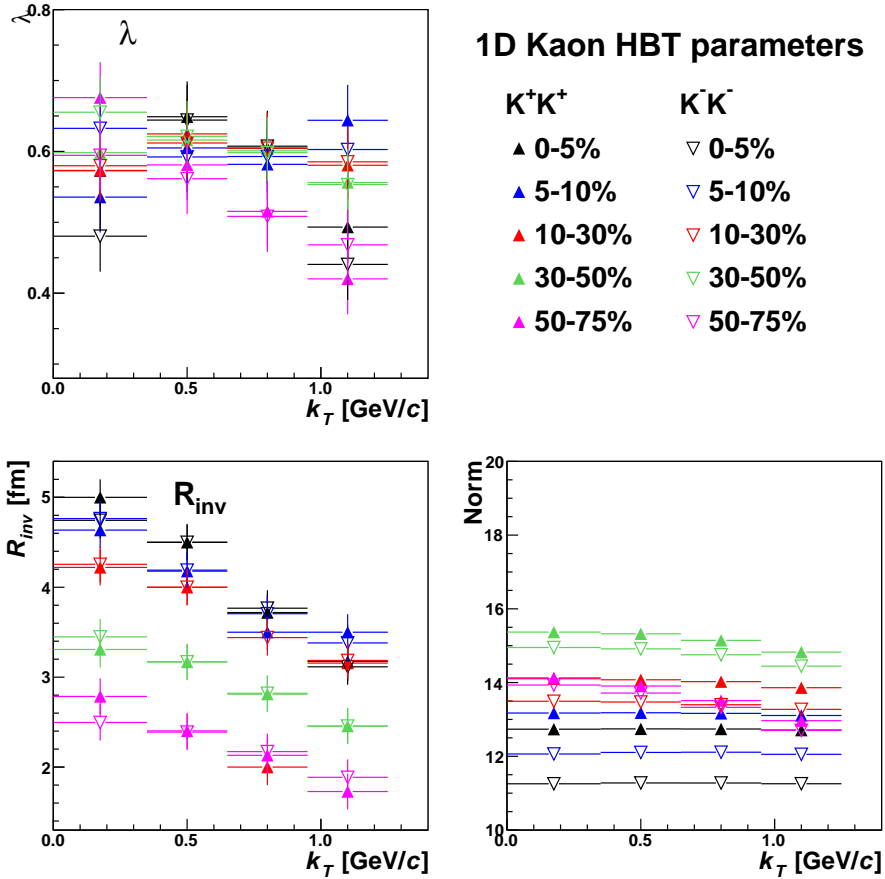
Figure 6.2: Fit results: λ parameters, source radii R_{inv} and normalization factors $\mathcal{N}$ as a function of k_T and centrality.

The errors of the fit results are dominated by systematic uncertainties which were estimated by varying the fit ranges. Within presented errors, no significant difference between source radii R_{inv}

from positive and negative kaons is observed.

More information about the kaon source can be obtained from a three-dimensional correlation function. Similar procedure as for the one-dimensional correlation functions was used for correction of the three-dimensional correlation functions on misidentification of particle and momentum resolution. The fitting was performed by the parametrization given in Eq. 5.7. An example of fitted three-dimensional correlation function for centrality 10-30% and $0.35 < k_T < 0.65$ GeV/c is shown in Figure 6.3.
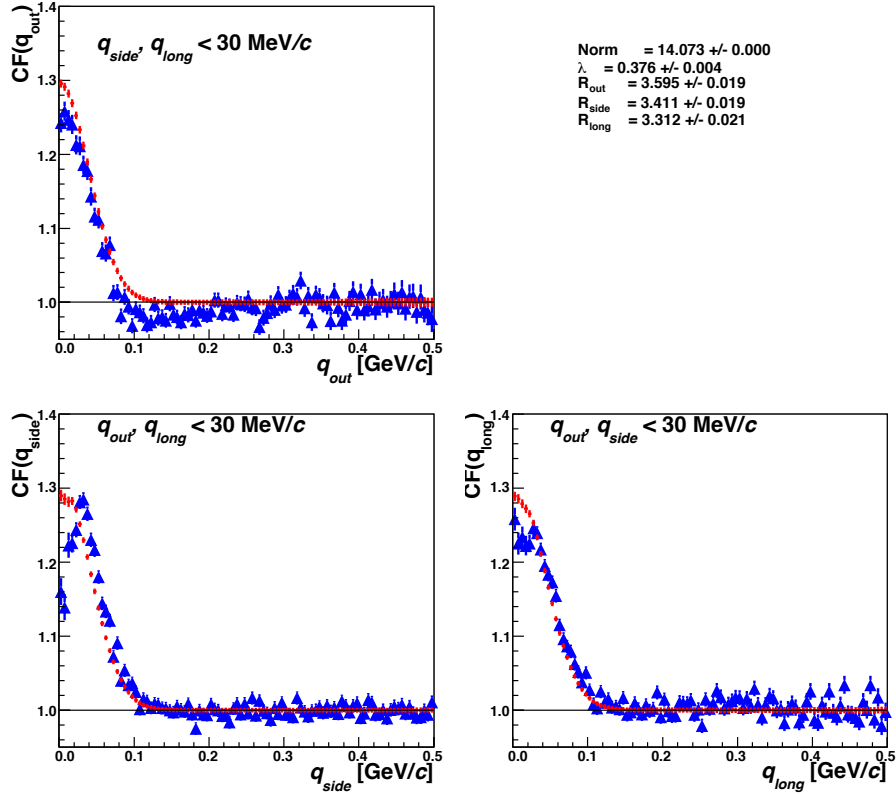
Figure 6.3: Projection of the three-dimensional correlation function and corresponding fits according Eq. 5.7 for positive kaons for centrality 10-30% and $0.35 < k_T < 0.65$ GeV/c.

Figure 6.4 shows the HBT parameters λ, R_{out}, R_{side} and R_{long} for four centralities as a function of the pair transverse momentum k_T, separately for positively and negatively charged kaons. The extracted HBT radii decrease as a function of k_T. While the observed decrease of the R_o and R_l is produced by the transverse flow, the falling of R_l radii is ascribed to the longitudinal expansion of the source. The λ parameter slightly increases with k_T. For most measured values there is a good agreement between the parameters extracted from the positively and negatively charged kaons. The first and the last k_T bin for centrality 50-75% is statistically limited, therefore the fits for these bins are unstable. Recently, the femtoscopy with the like-sign kaon in Au+Au collisions at energy $\sqrt{s_{NN}} = 200$ GeV was also performed by the PHENIX experiment [76]. Figure 6.5 shows the comparison of the extracted HBT radii by the PHENIX collaboration for the 0-10% most central events with those obtained in this analysis at the same beam energy, collision system and centrality. In general, the same trend of the HBT radii is observed, however our results are slightly lower. The presented results contains only the statistic errors.
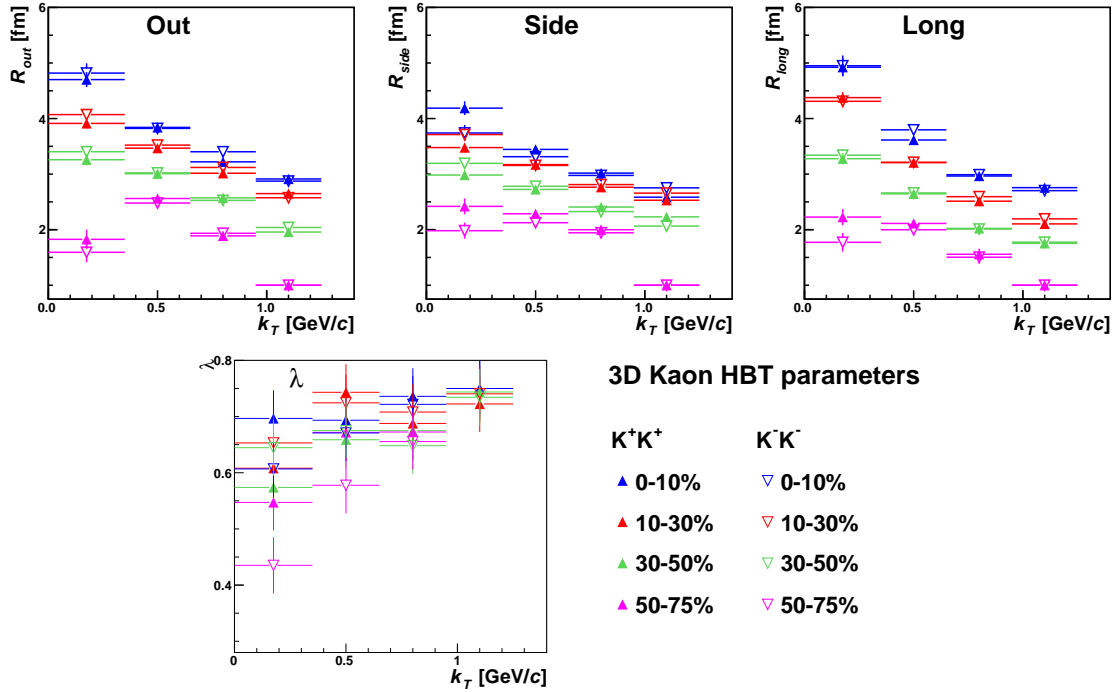
Figure 6.4: Fit results: λ parameter, HBT radii R_{out}, R_{side} and R_{long} as a function of k_T and centrality.
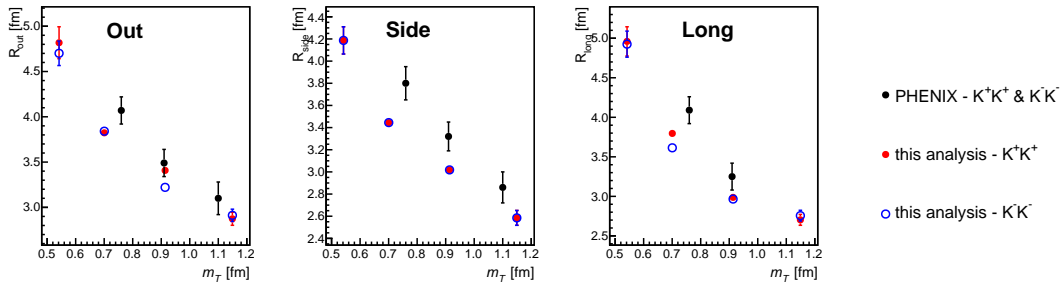
Figure 6.5: Comparison of extracted HBT radii R_{out}, R_{side} and R_{long} from Au+Au collision at $\sqrt{s_{NN}} = 200$ GeV to PHENIX results [76] for the same beam energy, collision system and centrality.

6.1.1   Blast-wave parametrization

It was already discussed that in order to obtain complete space-time extents of the source it is necessary to employ a model describing four-dimensional particle emission. One of the most standard tools in femtoscopy for such a purpose is the blast-wave parametrization [55] (see Chapter 3) which is designed to describe the freeze-out configuration with minimal set of parameters. The same blast-wave model which was described in detail in Chapter 3 is also used in this section. The extracted space-time extent by the blast-wave parametrization will be used in the next section for the parametrization of the source in more sophisticated hydrodynamical models and theoretical calculations.

Since the significant difference between the extracted HBT radii from the measured pairs of positive and negative kaons was not observed, it was possible to combine the measured pairs of kaons to decrease

statistics uncertainties. Then the blast-wave parametrization was used for fitting the obtained kaon HBT radii and the particle spectra with a single set of free parameters. The combined particle spectra of pions, kaons and protons were simultaneously used in the fit to constrain the temperature and the flow velocity. Here, the data on p_T spectra are taken from [77]. Contrary to the most general case when the blast-wave model employs eight independent parameters to describe the studied system, in this analysis due to the unavailability of the event plane only five parameters were used: the freeze-out temperature T, the maximum transverse rapidity ρ_0, the radius of the source R, the system proper time τ and the emission duration $\Delta\tau$. The combined kaon HBT radii with the blast-wave fits are presented in Figure 6.6. As can be seen the blast-wave parametrization is able to successfully describe the measured HBT radii, however some deviations are observed for the lowest centrality 50-75%.
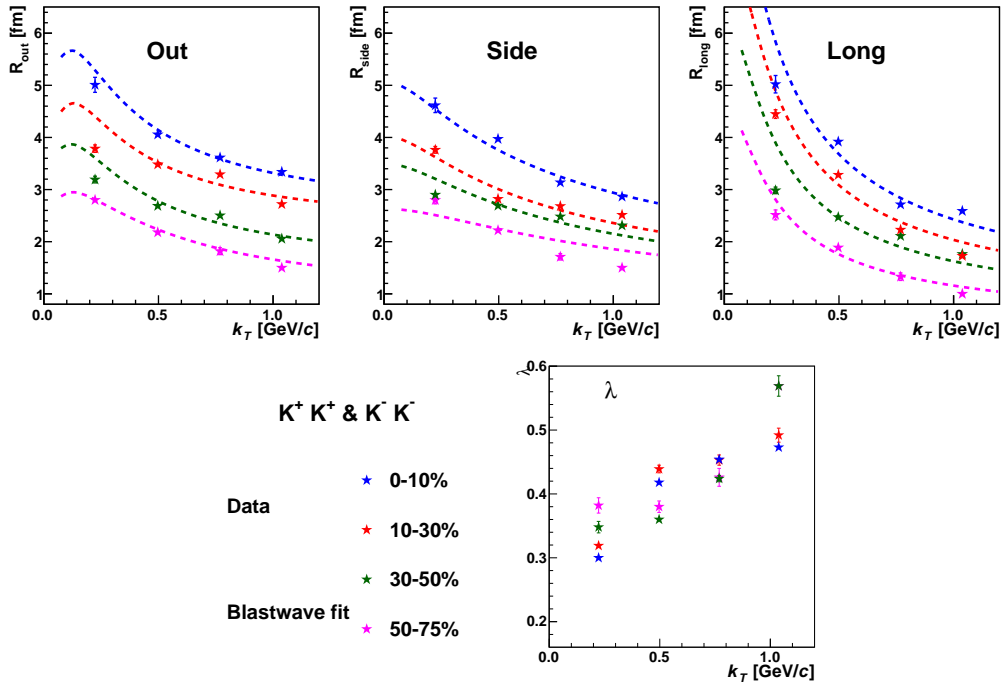
Figure 6.6: Comparison of extracted kaon HBT radii R_{out}, R_{side} and R_{long} with the blast-wave fit represent by colored lines for four centrality and four k_T bins.

Centrality[%]	T [MeV]	ρ_0	R[fm]	τ[fm/c]	$\Delta\tau$ [fm/c]
0-10	104±3	1.02±0.01	11.1±0.3	6.8±0.3	2.8±0.1
10-30	106±3	1.00±0.02	8.8±0.2	4.9±0.3	2.8±0.2
30-50	111±6	0.91±0.05	7.5±0.3	4.4±0.3	1.6±0.1
50-75	115±10	0.89±0.08	3.4±0.3	3.0±0.2	0.7±0.1

Table 6.1: Extracted parameters from a blast-wave fit to kaon HBT radii and pion, kaon and proton transverse momentum spectra at $\sqrt{s_{\mathrm{NN}}} = 200$ GeV.

The extracted parameters from the blast-wave model are shown in Table 6.6 for four centrality. Most of the parameters and their dependence on the collisions centrality agree with the expectations. While the temperature T decreases with the increasing centrality, the maximum transverse rapidity ρ_0

increases with increasing centrality. Such behavior of these parameters reflects increasing source size with the centrality. The expansion of the larger system takes longer time as shown by the decreasing system evolution time τ and the emission duration $\Delta\tau$ with the decreasing the centrality.

It is especially interesting to compare our extracted blast-wave parameters with the parameters from pion femtoscopy [78]. Figure 6.7 presents the comparison of the obtained blast-wave parameters from this work and from the STAR analysis of pion femtoscopy [78]. The results are also compared to PHENIX results on blast-wave fit of the kaon HBT radii [76].
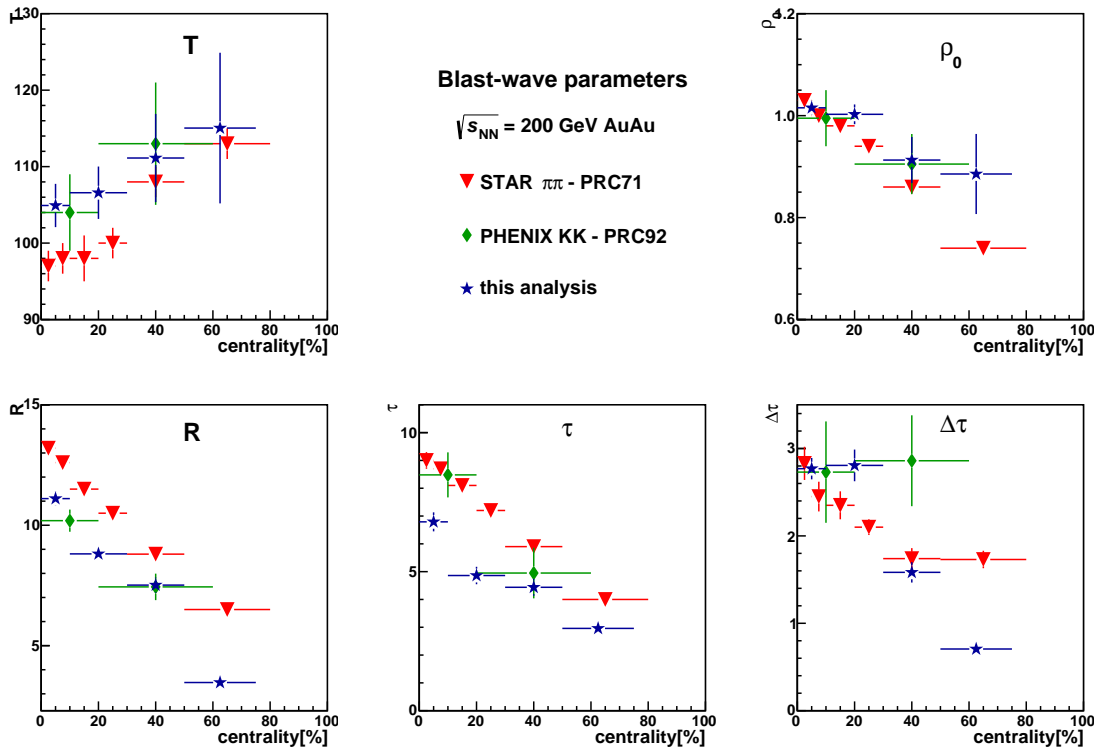
Figure 6.7: Comparison of extracted blast-wave parmeters from fits to HBT radii. The red stars represents results from fit $\pi - \pi$ HBT radii, the green diamond is for PHENIX results on KK femtoscopy and the blue stars represents blast-wave parameters obtained in this analysis.

As can be seen the blast-wave parameters from kaon femtoscopy seem to slightly differ from those parameters obtained from the STAR pion HBT radii [78]. For given centrality, the temperature T of the system obtained in our analysis is higher than for pion femtoscopy. The measured radius R of the source, system evolution time τ and emission duration $\Delta\tau$ are also smaller than those obtained from the previous pion femtoscopy [78]. All of these observed differences would suggest that the kaons could be emitted earlier than pions due to their relative smaller cross section [79] with hadronic matter in comparison with pions. However one has to be very careful, because this conclusions need to be further tested and especially systematic errors have to be carefully evaluated.

6.2 Unlike-sign kaon correlation function

In this section experimental correlation function for unlike-sign kaon is studied in detail. The measured raw functions were corrected for misidentification of particle in a same ways as like-sign kaon correlation functions via Eq. 5.5. The correction for the momentum resolution has not been applied so far. In the future when the unlike-sign kaon correlation function is fitted, the momentum resolution will be useful for fitting in the region of the low q_{inv}. The corrected unlike-sign kaon correlation functions for centrality 0-5% and centrality 30-50% for 4 k_T bins are shown in Figure 6.8 and Figure 6.9. The correlations functions for other centralities can be found in Appendix A.

6.2.1 Comparison of unlike-sign one-dimensional correlation to Lednický model

The experimental results of the unlike-sign one-dimensional correlation function are compared to the theoretical prediction from Lednický model [45] in Figure 6.8 and Figure 6.9. The theoretical functions were calculated accord to Eq.3.6. Similarly, in the case of the one-dimensional correlation functions, the source was characterized by one-dimensional Gaussian in the PRF with a parameter R_{inv}. Here the individual R_{inv} are those extracted from fitting like-sign kaon correlation function (see Figure 6.2). The Lednický FSI model [45] includes the treatment of $\phi(1020)$ resonance in the final state. The extended femtoscopics formalism, which contains generalized form of the smoothness approximation, is included in this model. As authors of the models claim, the generalized smoothness assumption is needed for correct description of the correlation function in the region of the resonance. Since the theoretical function does not include effects contained in the experimental λ parameter, it is scaled for correct comparison according to

$$CF = \left(CF^{theo} - 1\right)\lambda + 1, \tag{6.1}$$

where λ parameter was obtained from the fit to the like-sign kaon correlation function (see Figure 6.2).

Example of comparison of unlike-sign kaon correlation function to model calculations is shown in Figure 6.8 and Figure 6.9. The measured unlike-sign kaon correlation functions for the most central collisions and for 4 k_T bins are shown in Figure 6.8. Figure 6.9 presents the comparison of the theoretical function to experimentally measured functions for mid-peripheral collisions, centrality 30 - 50%. The comparisons of model calculations to experimental correlation functions for other centralities are presented in Appendix A.

As can be seen, the model reproduces well the overall structure of the measured correlation functions. At the region of the low q_{inv} where the well-known attractive Coulomb interaction and the strong interaction in s-wave are present, the model is able to describe the strength of the correlation. For most central collisions and low k_T mid-peripheral, the Lednický model is also able to predict the measured correlation function in the region of the resonance region.

However, with decreasing source size (decreasing centrality and higher k_T) the model starts to underestimate the strength of the correlation function. Even when the correlation function is underestimated by Lednický model in the region of the resonance, the model still describes the correlation at the low q_{inv}. The small difference in the low q_{inv} can be ascribed to effect of the smearing and/or possibly residual correlations.
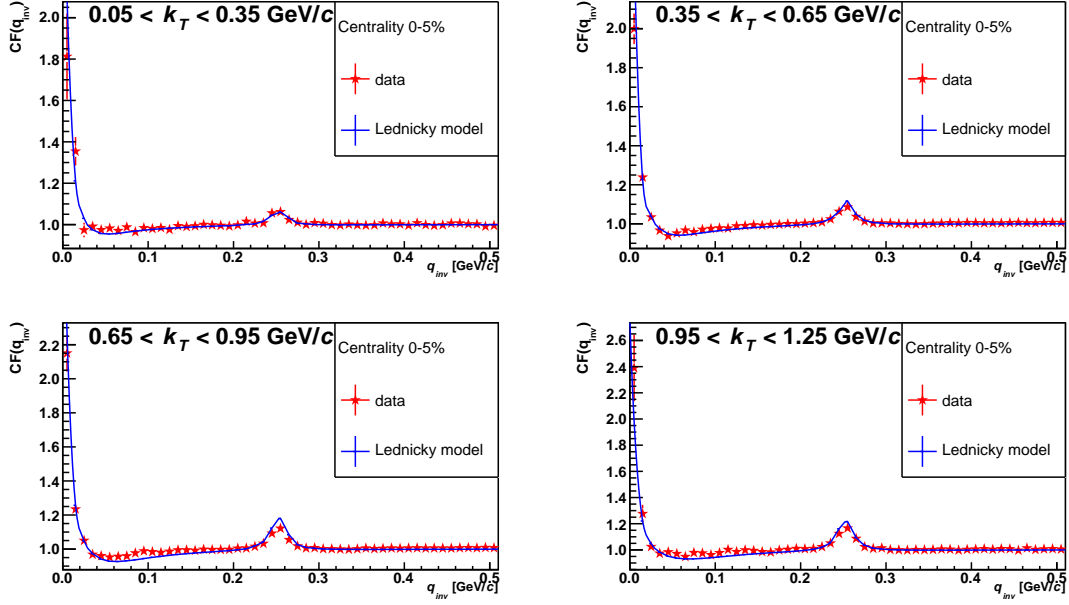
Figure 6.8: Comparison of experimental unlike-sign kaon correlation function to theoretical calculation for centrality 0-5% centrality for 4 different k_T bins.
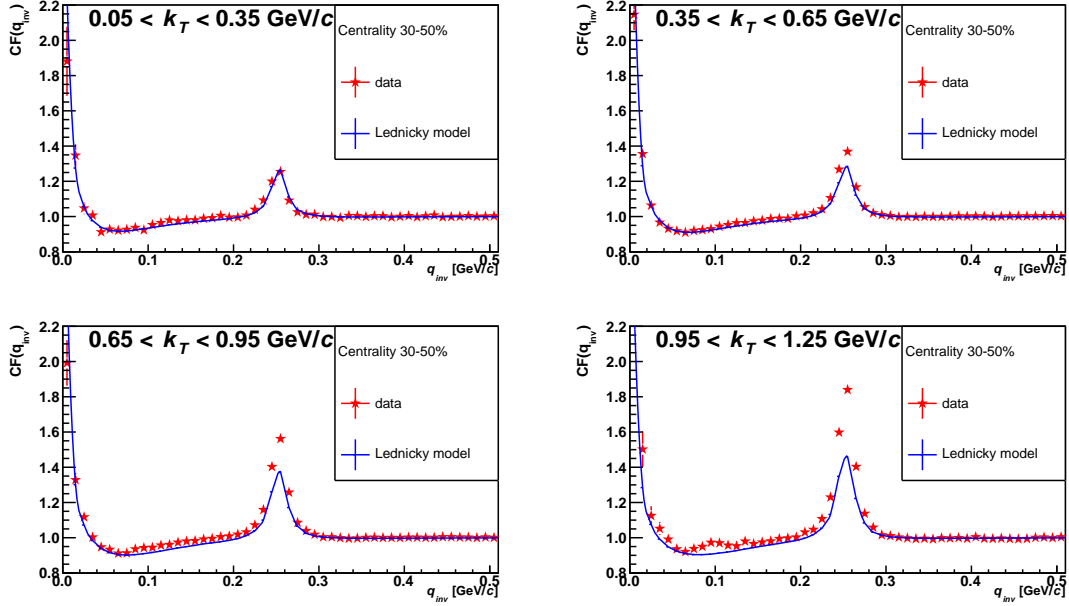
Figure 6.9: Comparison of experimental unlike-sign kaon correlation function to theoretical calculation for centrality 30-50% centrality for 4 different k_T bins.

It was predicted by Lednický [45], that the strength of the correlation should change with the source size R_{inv} as R_{inv}^{-3} The right panel of Figure 6.10 shows the height of the peak of the resonance as a function of the measured like-sign source size R_{inv}.

The dependence of the height of the peak on the R_{inv}^{-3} is shown in the left panel of Figure 6.10. As
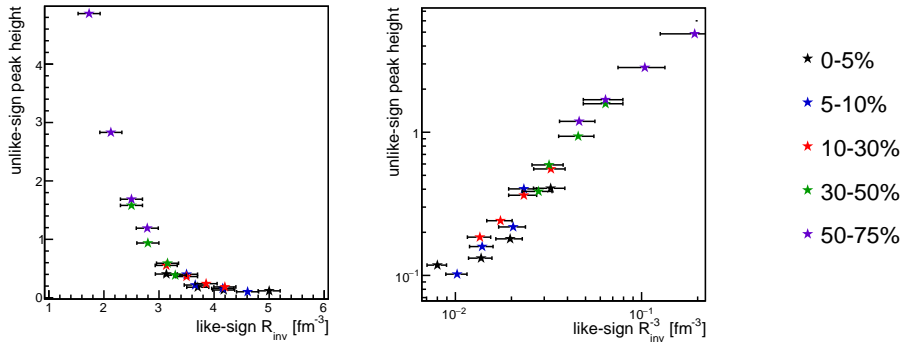
Figure 6.10: Left: The dependence of the height of the peak as a function of measured source radii R_{inv} from like-sign kaon correlation function. Right: The dependence of the height of the peak as a function of inverse volume of the system $\sim R_{inv}^{-3}$, where the source size R_{inv} is obtained from one-dimensional like-sign correlation functions.

can be seen, the peak height scales with source size as R_{inv}^{-3}. In particular, it is especially interesting to note that the same source sizes R_{inv} were obtained from different correlation functions. The R_{inv} is the same for higher centrality and higher k_T as well as for lower centrality and lower k_T. Within errors arising from the extraction of the source radii by fitting like-sign kaon correlation function, the height of the peaks are consistent. It indicates that the correlation function in the region of the resonance is indeed connected to the source size and does not depend for example on temperature.

In the following two subsections the experimental correlation functions are compared to hydrodynamic model predictions, namely to HYDJET++ and THERMINATOR 2. Such a model comparison can bring additional insight into the interpretation of the results.

6.2.2 Comparison of unlike-sign one-dimensional correlation with HYDJET++

HYDJET++ (HYDrodynamics plus JETs) is Monte Carlo heavy ion event generator for simulation of relativistic heavy ion AA collisions [53]. It is considered as a superposition of the soft, hydro-type state and the hard state resulting from multi-parton fragmentation. The soft part of HYDJET++ is based on the parameterization of relativistic hydrodynamics with present freeze-out conditions used for the chemical and thermal freeze-out hypersurfaces during generating the thermal hadronic state. HYDJET++ includes the longitudinal, radial and elliptic flow effect and the decays of hadronic resonances. However, HYDJET++ does not include any interactions.

HYDJET++ contains default setup of input parameters for describing system created in Au+Au collisions at energy $\sqrt{s_{NN}} = 200$ GeV. This setup was tuned for description of the spectra, v_2 and HBT radii of the most abundant particles, pions [53]. HYDJET++ can also successfully reproduce the particle ratios. The used input parameters are summarized in Table 6.2.

The unlike-sign kaon correlation function was obtained by applying the same kinematic cuts that were used in analysis. Since HYDJET++ does not contain Coulomb interaction and Strong final-state interaction, only the peak in the region of the $\phi(1020)$ resonance is presented. This peak corresponds to the thermal production of the $\phi(1020)$ resonance. The experimental correlation functions were

Parameter	Value	Parameter	Value
T_{ch} (GeV)	0.165	μ_{I_3} (GeV)	-0.001
T_{th} (GeV)	0.100	τ (fm/c)	8
μ_B (GeV)	0.0285	$\triangle\tau$ (fm/c)	2
μ_s (GeV)	0.007	R (fm)	10
μ_c (GeV)	0	γ_S	1

Table 6.2: Input parameters of the HYDJET++ model used in the presented simulations.

scaled by the λ parameters according to

$$CF^{corr} = \frac{CF^{raw} - 1}{\lambda} + 1, \tag{6.2}$$

where λ parameters was obtained from the fit to the like-sign kaon correlation function (see Figure 6.2). Figure 6.11 shows the comparison of experimental unlike-sign kaon correlation function with the correlation function obtained from HYDJET++.
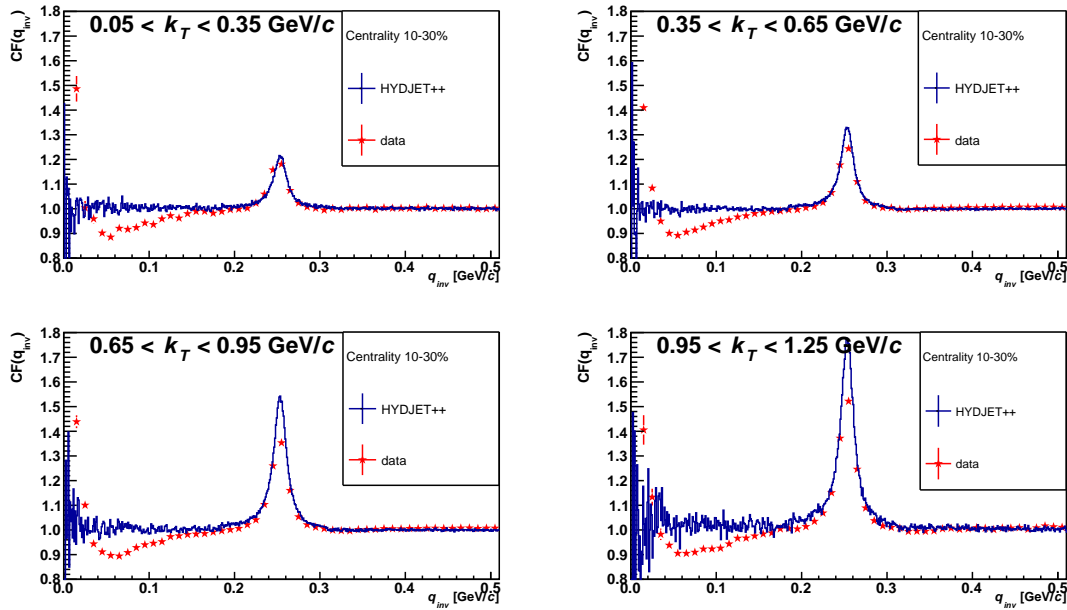
Figure 6.11: Comparison of experimental unlike-sign kaon correlation function with HYDJET++ calculation for centrality 10-30% for 4 different k_T bins.

As can be seen, the correlation functions from HYDJET++ show similarly strong sensitivity in the region of the resonance. The sensitivity of the correlation function in the region of resonance is qualitatively the same as already observed in the experimentally measured function, but for higher k_T bins the height of the peak is overestimated for higher transverse pair momentum. The observed overestimation of the correlation function in region of the resonance can be related with imprecise reproducing of the transverse mass spectra of the $\phi(1020)$ mesons in the model as shown in Figure 6.12. It should be noted that comparison with HYDJET++ with standard tune for RHIC energy may be a bit problematic. The scaling by the λ parameter is questionable. This will be object of further studies as well as tuning HYDJET++ to correctly reproduces ϕ spectra.
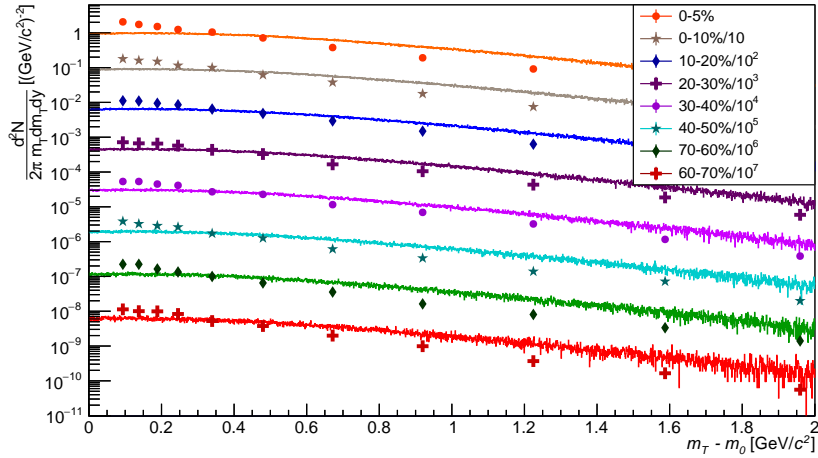
Figure 6.12: Measured transverse mass spectra of the $\phi(1020)$ mesons [21] compared to HYDJET++ predictions.

6.2.3 Comparison of unlike-sign one-dimensional correlation with THER-MINATOR 2

The experimentally constructed unlike-sign kaon correlation functions were also compared with prediction by THERMINATOR 2 [54]. It is thermal heavy-ion generator dedicated to studies of the statistical production of particles in ultra-relativistic heavy-ion collisions [54]. THERMINATOR 2 includes various shape of the freeze-out hypersurface and the expansion velocity field, including 2+1 as well as 3+1 dimensional profiles. Behind the statistical approach, it contains hadronic resonances which significantly contribute to the observables.

The freeze-out configuration of the source emitting particles was characterized by Blast-wave model with following set of parameters: temperature T, barion chemical potential μ_B, strangeness potential μ_s, third component of isospin μ_I, transverse velocity v_T, maximal transverse radius ρ_{max} and the proper time at freeze-out τ. As can be seen, it is quite different blast-wave model than the one which was used for fitting kaon HBT radii was discussed in the previous section. Compared to the Gaussian parametrization of the source, the blast-wave parametrization is more realistic and inherently introduces k_T dependence of radii as well as $r - k$ correlations [45]. The relative distance of emission point of two particles is correlated with relative pair momentum. Such phenomena should reflect in the height of the peak.

In the presented analysis, the setup [80] for collision energy $\sqrt{s_{NN}}$=200 GeV was used. The interaction between particles was calculated by the already discussed Lednický model [45]. Figure 6.13 shows the comparison of experimental unlike-sign correlation function for the most central collisions with calculations where the source was parametrized by the Gaussian as well as blast-wave parametrization from THERMINATOR 2. As can be seen, both of the used source parameterizations successfully reproduces the shape of the correlations and describe the strength of correlations in the region of the resonance.

However, the blast-wave parametrization used in THERMINATOR model is different from the previously employed and includes natively λ parameter, this comparison provide the first look on case when the theoretical calculation is performed with more realistic source parametrization. In future the
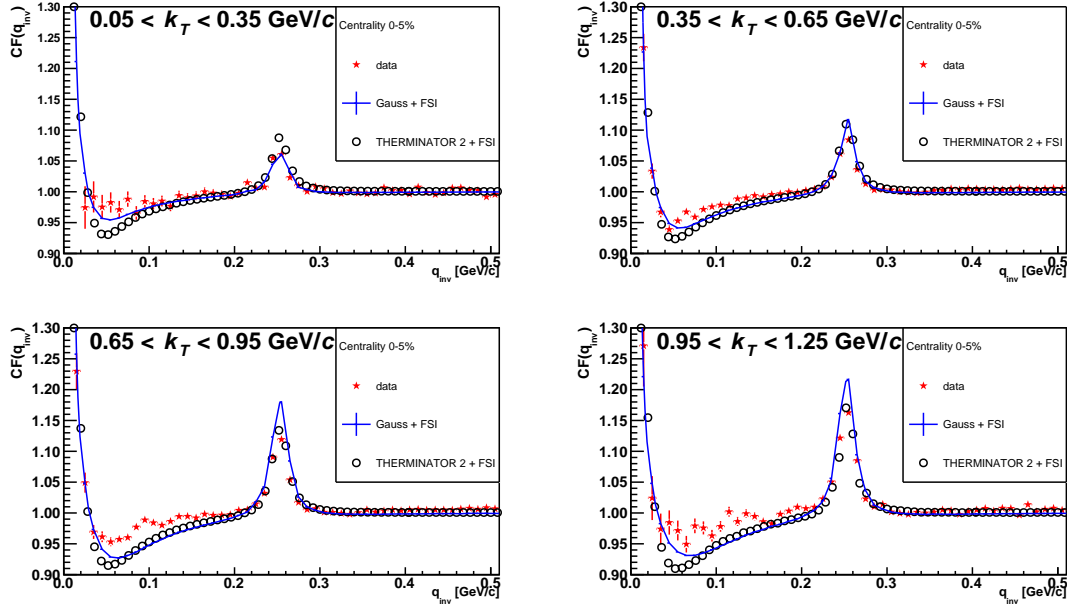
Figure 6.13: Comparison of experimental unlike-sign kaon correlation function to two model calculations for centrality 0-5% and 4 different k_T bins. The blue lines represent the case when the source is parametrized by the Gaussian. The open blue circle shows correlation function calculated f by THERMINATOR 2.

similar calculations will be done with same blast-wave model, which was used for fitting. It enables to compare experimental correlation function for other centralities.

In the future model like HYDJET++ or THERMINATOR 2 can be used for estimation of the effect of residual correlations. These effect arise from the presence of particles which come from weak decays of already correlated particles. THERMINATOR has been specially develop for such studies and has been commonly employed by experiment at RHIC [81], [82] and LHC[83]. Figure 6.14 shows contribution of two resonance decays to kaon transverse momentum.
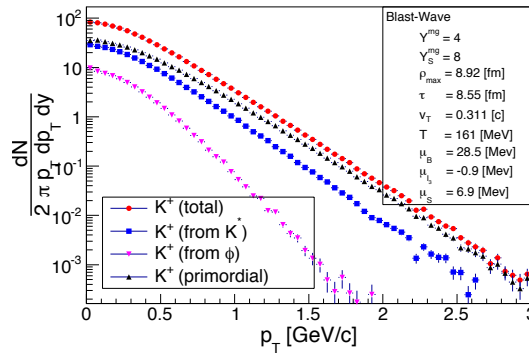
Figure 6.14: The transverse momentum spectra of positive kaon with two resonance decay contribution.

6.2.4   Three-dimensional unlike-sign kaon correlation function

Finally, the three-dimensional unlike-sign kaon correlation functions were constructed by the method already described in section 3.2.4 . The measured function depends on k^*, hence the observed resonance is present in the region of $k^* \sim 126$ MeV/c. Figure 6.15 shows the three-dimensional unlike-sign kaon correlation function for different centralities and integrated over k_T. As can be seen, the $\phi(1020)$ resonance is still present and exhibits similar strong sensitivity to the source size in all three projections.
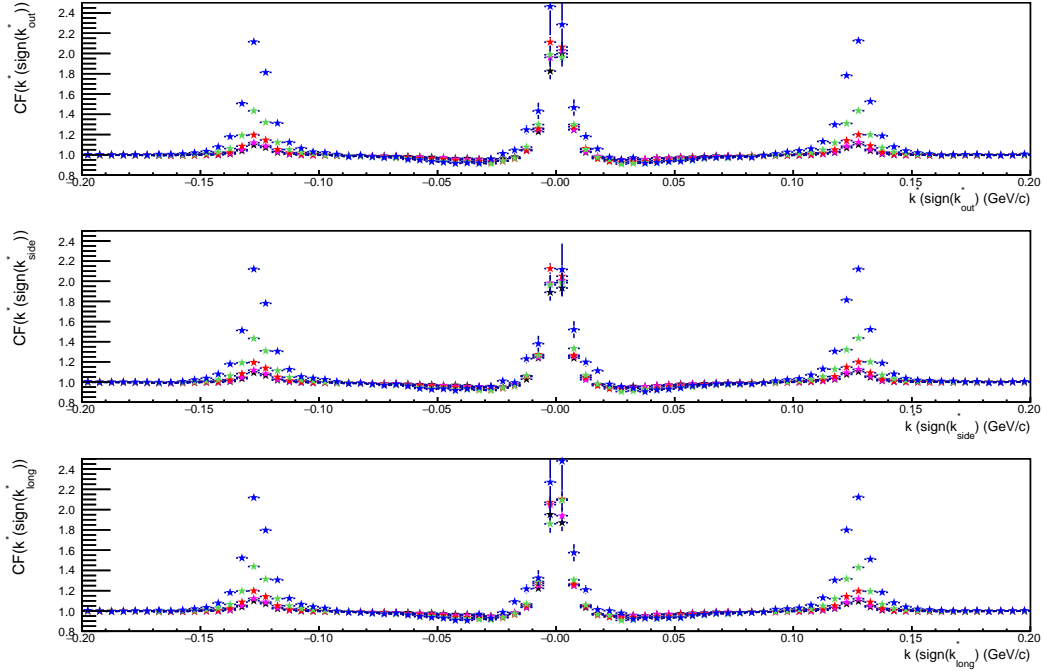
Figure 6.15: Three-dimensional non-identical kaon correlation function for five centralities. The blue 50-75%, the green 30-50%, the red 10-30%, the magenta 5-10% and the black stars are for centrality 0-5%. Top panel is for out direction, middle for side and bottom panel for long direction.

The common cross-check which can be done is the "double ratio" of three-dimensional non-identical kaon. As was discussed in chapter 3, the "double ratio" serves as a quality check of the measured functions as well as an indicator of space and time asymmetry in the emission between the two particle species. Figure 6.16 shows the "double ratio" for measured non-identical kaon correlation function for the centrality 0-5%. As can be seen, due to an azimuthal symmetry and symmetry in rapidity, the "double ratio" of measured correlation functions for direction *side* and *long* is within statistics errors equal to unity. Also, the last "double ratio" for *out* direction is equal to unity. It confirms our previous results when extracted HBT radii were the same for positively and negatively charged pairs of kaon and shows that there is no emission asymmetry between kaons and anti-kaons.
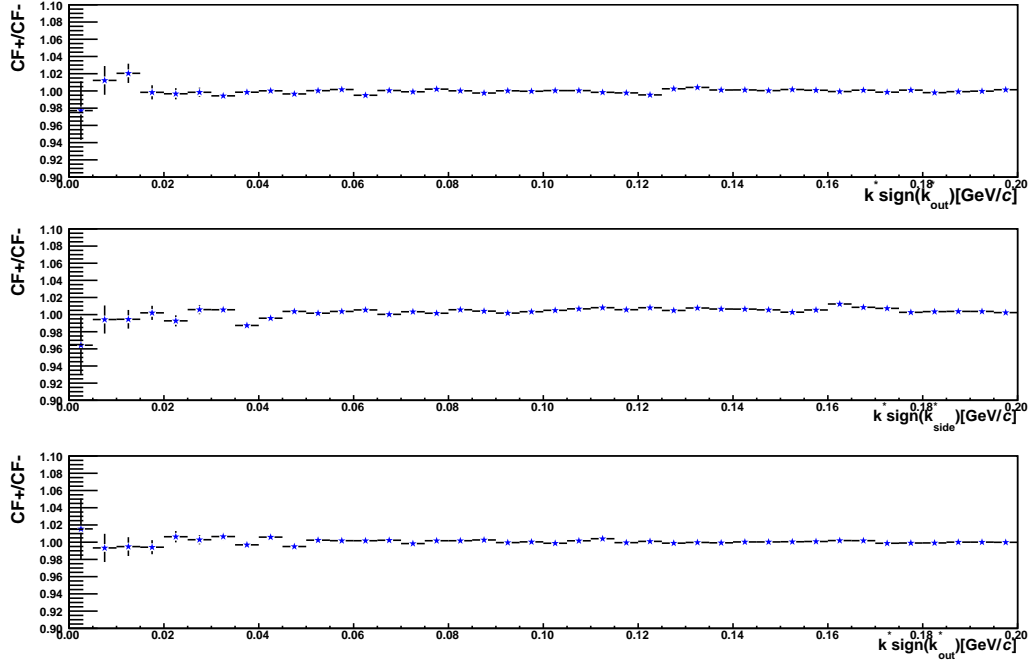
Figure 6.16: Double ratio of three-dimensional non-identical kaon correlation function for centrality 0-5%. Top panel is for out direction, middle for side and bottom panel for long direction.

Conclusions and Outlook

The main purpose of the analysis introduced in this work is a femtoscopic study of two-particle correlation function in a system where narrow near-threshold resonance is present. The correlation function is predicted to be highly sensitive to the source size and momentum-space correlations in the region of the resonance. System of unlike-sign kaons is ideally suited for such a study since it contains the $\phi(1020)$ resonance. The presented analysis was performed on minimum bias data from Au+Au collisions at $\sqrt{s_{NN}} =$200 GeV collected by the STAR experiment. It is the first high-statistics systematic study of unlike-sign kaon correlation function in heavy-ion collisions. The preliminary results of the analysis have already been presented at several conferences (Appendix B).

The available statistics and selection criteria allowed to construct one dimensional correlation functions for pairs of unlike-sign kaons for five collision centralities and four different k_T bins. First results for k_T-integrated three dimensional correlation functions were also obtained. All measured unlike-sign kaon correlation functions (Figure 4.12) exhibit strong centrality and transverse pair momentum dependence in the region of the ϕ resonance.

In order to compare the experimentally measured correlation functions with theoretical predictions and model calculations a femtoscopic analysis with like-sign kaons was performed using the same centrality classes and k_T bins. The extracted space-time extents were then used for parameterizing the source in the theoretical calculations of the unlike-sign kaon correlation functions. This like-sign analysis uses the highest available dataset and is hence the most precise measurement of kaon HBT radii at RHIC. The preliminary results on the HBT radii ($R_{out}, R_{side}, R_{long}$) obtained from three dimensional correlation functions (6.4) follow characteristic trends in the centrality and k_T confirming the presence of the collective expansion of the system. The comparison with recently published PHENIX results (6.5) shows small systematic difference towards smaller values. The measured radii and kaon spectra were fitted by blast-wave model obtaining parameters which describe the kaon source at the kinetic freeze-out. The larger available statistics at STAR has resulted in a larger number of k_T bins for each centrality and allowed better constraints of the blast-wave fits. The extracted blast-wave parameters and their dependence on collision centrality agree with the expectations, following similar trends as for pions. The comparison with STAR pion blast-wave results (Figure 6.7) reveals systematically smaller size, higher temperature and smaller transverse velocity. This may indicate possible earlier emission of kaon from the system. However, this conclusions need to be further tested and especially systematic errors have to be carefully evaluated.

After the extraction of source parameters from like-sign correlation function, the experimental unlike-sign correlation functions were compared to theoretical calculations based on the improved Lednický model of the final-state interaction. This model includes the treatment of $\phi(1020)$ resonance due to final-state interaction and therefore it should be able to reproduce the structure of the measured correlations. The results were compared to calculations using simple Gaussian parameterization of the kaon source as well hydro-based models: HYDJET++ and THERMINATOR 2. All calculations qualitatively reproduce the measured correlation function, however their quantitative agreement gets worse for smaller systems. Although the Lednický model contains the generalized smoothness assumption, the observed underestimation of the strength of the correlation in the region of the resonance for lower centralities and higher k_T bins can be probably ascribed to a breakdown of the smoothness

approximation - one of the basic assumption in femtoscopy. Other explanation, supported by the author of the model, is an interplay between thermally produced resonances and those produced as a result of the final state interaction. If the thermal production and the production via final-state interaction are not equivalent, the free room which the FSI model leaves should be filled by the thermal production of the $\phi(1020)$ resonance. In such a case, the Lednický model does not properly describe the correlation function in the resonance region for the most central collisions. Currently there is no clear consensus on the side of the theory, hence the high-statistics results presented in this thesis can help to clarify the issue.

The results in this thesis are first systematic study of two-particle correlation function in a system where narrow near-threshold resonance using the femtoscopic formalism. For this reason there is still much work that can be done in the future. To strengthen the conclusions detailed study of systematic errors is under way. Also since radii extraction is at this point dominated by systematic uncertainties it may be possible to increase the number of k_T bins.

One of the most interesting challenges is related to the comparison of the measured correlation functions with the theoretical calculations and hydrodynamics models. The correct description of experimental unlike-sign kaon correlation function may need better parametrization of the freeze-out configuration of the source emitting particle in combination with detailed theoretical study of femtoscopic formalism in the region of resonace. In future, such analysis can provide additional insight into the studied system via femtoscopic measurements and bring complementary information to the standard measurements at very low relative momentum.

Appendices

UNLIKE-SIGN KAON CORRELATION FUNCTION
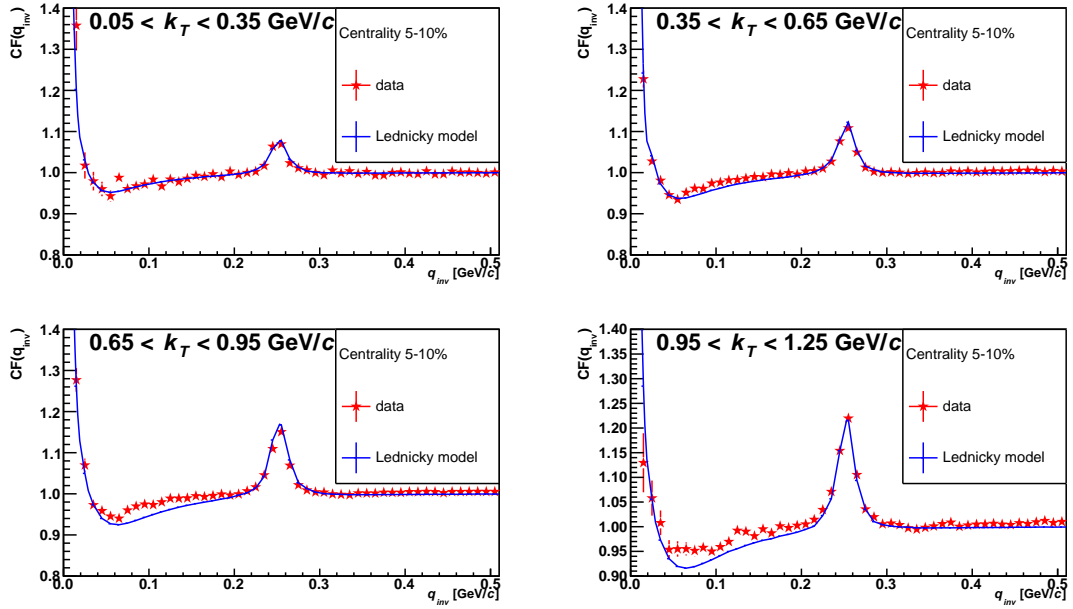
Figure A.1: Comparison of experimental unlike-sign kaon correlation function to theoretical calculation for centrality 5-10% centrality for 4 different k_T bin.
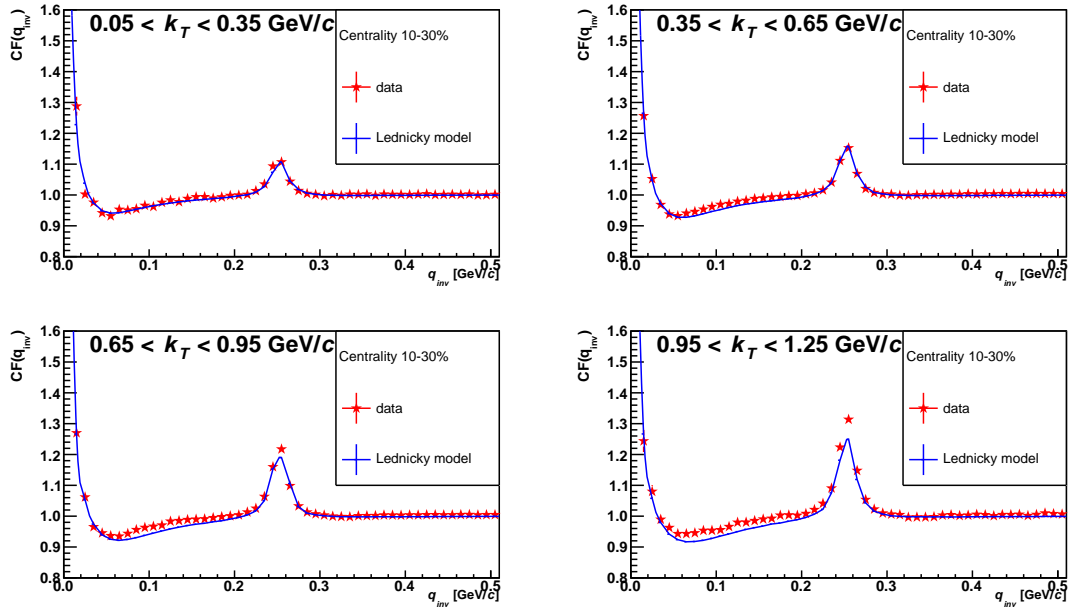
Figure A.2: Comparison of experimental unlike-sign kaon correlation function to theoretical calculation for centrality 20-30% centrality for 4 different k_T bin.
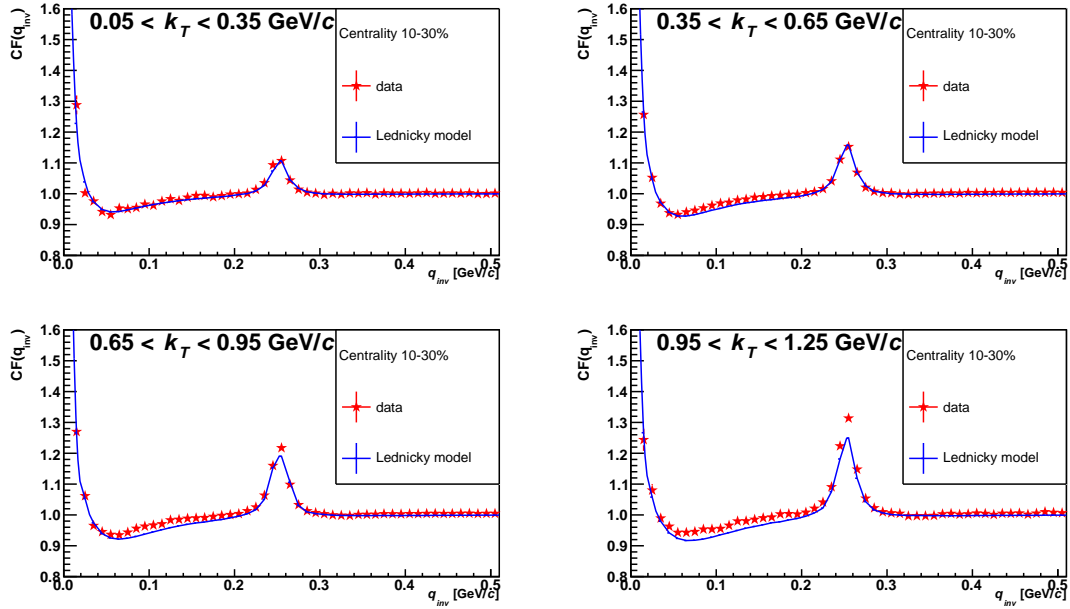
Figure A.3: Comparison of experimental unlike-sign kaon correlation function to theoretical calculation for centrality 50-75% centrality for 4 different k_T bin.

APPENDIX
TWO

LIST OF PRESENTATIONS AND PUBLICATIONS

The preliminary results of the analysis have already been presented at several conferences:

- The 4th International Conference on New Frontiers in Physics 2015, Chania, Greece, as a poster presentation with the title Femtoscopy with unlike-sign kaon at STAR in 200 GeV Au+Au collisions. Proceedings accepted and will be published in the European Physical Journal Web of Conferences

- XIth Workoshop on Particle Correlations and Femtoscopy 2015, Warsaw, Poland, as an oral presentation with the title Femtoscopy with unlike-sign kaon at STAR in 200 GeV Au+Au collisions. Proceedings accepted and will be published in Acta Physica Polonica B: Proceedigns Supplement.

- XVth Zimányi Winter School 2015 at Budapest, Hungary, as a part of an oral presentation about Femtoscopy with kaons at the STAR experiment.

Femtoscopy with unlike-sign kaons at STAR in 200 GeV Au+Au collisions

Jindřich Lidrych for the STAR Collaboration

Faculty of Nuclear Sciences and Physical Engineering

Czech Technical University in Prague

Abstract

In the collisions of heavy ions the nuclear matter can undergo a phase transition from hadrons to a state of deconfined quarks and gluons, the Quark-Gluon Plasma (QGP). Femtoscopic measurements of two-particle correlations at small relative momenta reveal information about the space-time characteristics of the system at the moment of particle emission. The correlations result from quantum statistics, final-state Coulomb interactions, and the strong final-state interactions (FSI) between the emitted particles.

It has been predicted [1] that correlations due to the strong FSI in a system where a narrow resonance is present will be sensitive, in the region of the resonance, to the source size and momentum-space correlations. Such a measurement can provide complementary information to the measurements at the very low relative momenta. This poster presents a status report of a STAR analysis of unlike-sign kaon femtoscopic correlations in Au+Au collisions at $\sqrt{s_{NN}} = 200$ GeV, including the region of $\phi(1020)$ resonances. The experimental results are compared with HYDJET++ simulations and to a theoretical prediction that includes the treatment of resonance formation due to the final-state interactions [1].

Motivation

The formalism of femtoscopic measurement at very low q_{inv} is well understood. The formalism proposed in [1] allows to use strong FSI going through a narrow resonance at higher q_{inv}.

The system of unlike-sign kaon pairs is ideally suited for testing this extension of femtoscopy formalism as it contains narrow $\phi(1020)$ resonance.

Use strong FSI in region of resonance:
- More sensitive
- Statistically advantageous
  - High statistics
  - Low feed down
  - Source well known from imaging

Unlike-sign kaon correlation function:
- $\phi(1020)$ resonance:
  $k^* = 126$ MeV/c, $\Gamma = 4.3$ MeV
- Narrow – separation of emission and FSI

Challenges – femtoscopy formalism at higher q_{inv}
Possibility of breakdown of basic assumptions
- Smoothness assumption
- Equal-time approximation

The Solenoidal Tracker at RHIC (STAR)

- 2π azimuthal coverage
- Pseudorapidity $|\eta| < 1$

Main subdetectors used for this analysis are:

Time Projection Chamber (TPC)
- Particle identification via specific ionization energy loss dE/dx
- Charged particle tracking and momentum reconstruction

Time of Flight (TOF)
- Particle identification via $1/\beta$
- Timing resolution < 100 ps
- Separation of charged kaons from other hadrons up to momentum ~1.5 GeV/c
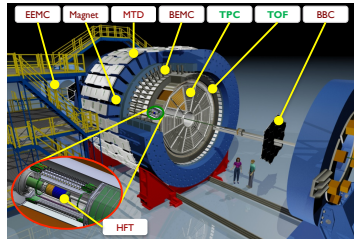
Data selection and construction of correlation function

- Au+Au collisions at $\sqrt{s_{NN}} = 200$ GeV taken in 2011

Track selection
- Primary track with signal from TOF
- $|\eta| < 1$ and $|DCA| < 3$ cm
- $0.15 < p < 1.55$ GeV/c
- $0.21 < m^2 < 0.28$ (GeV/c^2)^2
- $|n\sigma_{kaon}| < 3$,

where $n\sigma_{kaon}$ is the distance from the expected dE/dx for kaons expressed in terms of standard deviation units

Correlation function:

Koonin-Pratt eq.: $C(p_1, p_2) = \int d^3 r S(r, k) |\psi_{1,2}(r,k)|^2$,

where $S(r,k)$ is emission source function and $\psi_{1,2}(r,k)$ is wave function describing interaction

Experimentally: $C(q_{inv}) = \frac{N_{same}(q_{inv})}{N_{mixed}(q_{inv})} = \frac{real\ pairs}{mixed\ pairs}$

$q_{inv} = p_1 - p_2 = 2k^*$, $k_T = \frac{p_{1,T} + p_{2,T}}{2}$
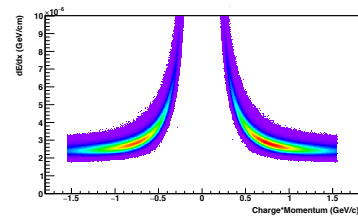
Event mixing
- To obtain uncorrelated two-particle distributions $N_{mixed}(q_{inv})$. In order to remove non-femtoscopic correlations, events are divided into sub-classes according to primary vertex position along the beam direction and multiplicity

Unlike-sign 1D correlation function

- Correlation functions are sensitive in the region of the ϕ resonance to the source size and momentum-space correlations

k_T dependence

Centrality dependence
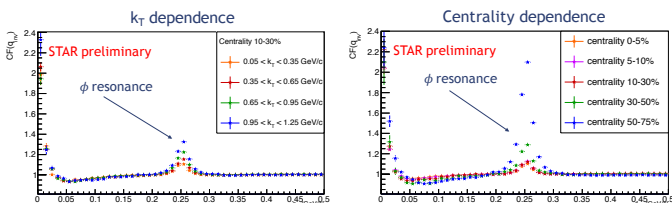
Like-sign 1D correlation function and fitting

- Used for extraction of kaon emission source size R_{inv} and lambda parameter λ
- Fitting function: $CF(q_{inv}) = \left[(1-\lambda) + \lambda K(q_{inv}) e^{-R_{inv}^2 q_{inv}^2}\right] N$,

  where λ - correlation strength, $K(q_{inv})$ - Coulomb function and N - normalization
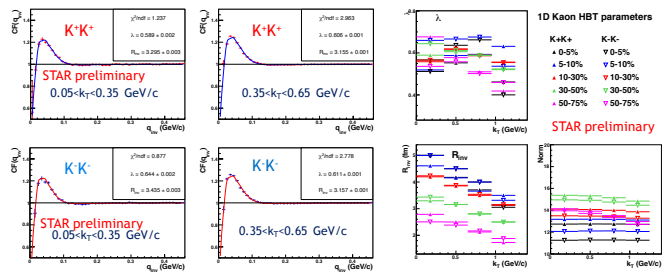
- The source radii R_{inv} increase with the centrality and decrease with pair transverse momentum k_T
- Only statistical errors shown; systematic error is underway

Comparison of unlike-sign 1D correlation function with HYDJET++ simulations

- HYDrodynamics plus JETs – Monte-Carlo heavy ion AA collisions generator [2]
- HYDJET++ contains only thermal production of ϕ, no Quantum statistics, Coulomb, Strong and FSI
- Experimental correlation function is corrected via $CF^{corr} = \frac{CF^{raw} - 1}{\lambda} + 1$, where λ parameter is from fitting like-sign correlation function
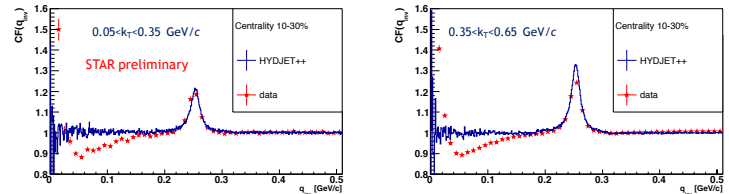
Comparison of unlike-sign 1D correlation function to Lednicky model

- Lednicky model [1] - includes the treatment of ϕ resonance due to the FSI as well as generalized smoothness approximation
- Gaussian source sizes R_{inv} used for calculation of theoretical CF are extracted from fitting like-sign CF
- Clean theoretical function is transformed to a raw one via: $CF^{raw} = (CF^{corr} - 1)\lambda + 1$, in order to compare to an experimental correlation function
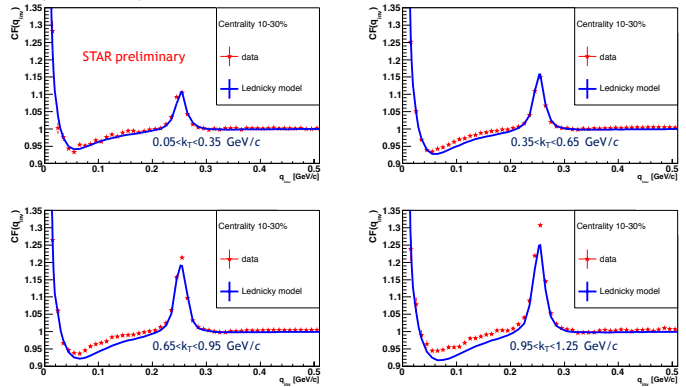
Conclusion

- Measurement of K^+K^- correlation function in Au+Au collisions
- Extraction of λ parameter and source radii R_{inv} from fitting like-sign correlation function
- HYDJET++ model reproduced the correlation functions well especially in the phi-mass region, final comparison will be done after the efficiency correction is applied to the data
- Studies of 3D correlation function underway

References:
[1] R.Lednicky, Phys.Part.Nucl.Lett. 8 (2011) 965-968
[2] I.P. Lokhtin et al., Comp.Phys.Comm 180 (2009) 779-799

Femtoscopy with unlike-sign kaons at STAR in 200 GeV Au+Au collisions

Jindřich Lidrych[1,a] (for the STAR Collaboration)

[1] *Faculty of Nuclear Sciences and Physical Engineering*
Czech Technical University in Prague
Břehová 7
115 19 Prague 1

Abstract.
In the collisions of heavy ions the nuclear matter can undergo a phase transition from hadrons to a state of deconfined quarks and gluons called the Quak-Gluon Plasma. Femtoscopic measurements of two-particle correlations at small relative momenta reveal information about the space-time characteristics of the system at the moment of particle emission. The correlations result from quantum statistics, final-state Coulomb interactions, and the strong final-state interactions between the emitted particles.

It has been predicted that correlations due to the strong final-state interactions in a system where a narrow resonance is present will be sensitive, in the region of the resonance, to the source size and momentum-space correlations. Such a measurement can provide complementary information to the measurements at very low relative momenta. This paper presents the preliminary results of a STAR analysis of unlike-sign kaon femtoscopic correlations in Au+Au collisions at $\sqrt{s_{NN}}$=200 GeV, including the region of $\phi(1020)$ resonance. The experimental results are compared to a theoretical prediction that includes the treatment of resonance formation due to the final-state interactions.

1 Introduction

In 1960 Goldhaber and collaborators observed in proton-antiproton annihilations an excess of pairs of identical pions produced at small relative momenta [1]. These observed correlations, as experimenters correctly asserted, came as a result of quantum statistics. Based on this observation the theoretical background of femtoscopy was developed by G. I. Kopylov and M. I. Podgoretsky in the 1970s [2]. Since then the femtoscopic measurements of two-particle correlations at low relative momenta became a standard tool for extracting the space-time extents of particle emitting sources. Nowadays femtoscopic studies include identical particles, as well as non-identical interacting particles [3–6].

The approach proposed by Lednicky [7] extends the femtoscopic formalisms to higher relative momenta between the two emitted particles in a system where the final-state interactions (FSI) contain a narrow, near-threshold, resonance. It is predicted that the correlation function will be more sensitive in the region of the resonance, where the strength of the correlation should change with the source size,

---

[a]e-mail: jlidrych@gmail.com

r as $\sim r^{-3}$ in comparison with measurements at the very low relative momenta, where the correlation function depends on r^{-2} or r^{-1}. In addition, these measurements will be statistically advantageous, since the particle spectra fall rapidly at low relative momenta.

Pairs of unlike-sign kaons are ideally suited for such femtoscopic analysis as they contain the narrow $\phi(1020)$ resonance. The $\phi(1020)$ resonance is characterized by the decay width $\Gamma = 4.3$ MeV and the decay momentum in the rest frame $k^* = 126$ MeV/c. The use of kaons is also advantageous due to the fact that the emission source function is less affected by weak decays of resonances. From previous STAR source imaging analysis [4], the kaon source function is known to be well-described by a Gaussian form.

2 Data analysis

The data used for this analysis were collected in Au+Au collisions at $\sqrt{s_{\mathrm{NN}}} = 200$ GeV by the Solenoidal Tracker at RHIC (STAR) in 2011. The STAR [8] is a multi-purpose detector, which excels in tracking and identification of charged particles at mid-rapidity with full coverage in azimuthal angle. The most important subdetectors for this analysis are the Time Projection Chamber (TPC) [9] and the Time of Flight (ToF) [10]. The TPC records charged particle tracks and measures their momentum p and identifies them via specific ionization loss dE/dx. For kaon selection, the particles were required to have $|n\sigma_K| < 3$, where $n\sigma_K$ is the distance from the expected mean $<$dE/d$x>$ expressed in terms of standard deviation units σ_K. The ToF measures particle velocity β which is used to calculate particle mass m according to the relation

$$\frac{1}{\beta} = \sqrt{1 + m^2/p^2}, \tag{1}$$

where the momentum p is measured by the TPC. Due to a good time resolution, which is less than 100 ps, the ToF is able to separate charged kaons from other hadrons up to $p \sim 1.55$ GeV/c, as shown in Figure 1. Due to this fact, only primary tracks at mid-rapidity $|\eta| < 1$ with momentum $p \in [0.15, 1.55]$
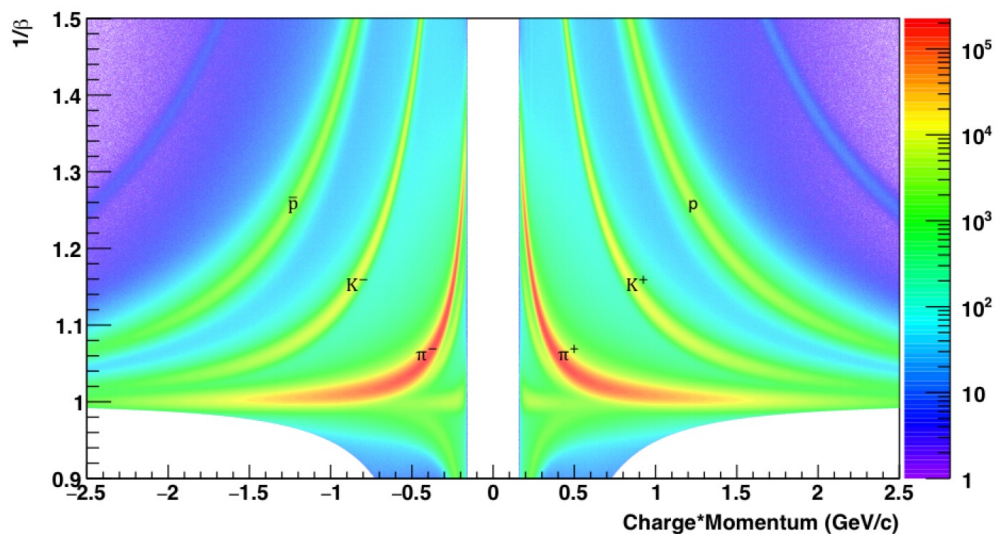
Figure 1. The relative velocity $1/\beta$ (from ToF) of charged particle as a function of momentum p (from TPC).

GeV/c, which have signal from the ToF and satisfy cut criteria on mass: $0.21 < m^2 < 0.28$ GeV^2/c^4 were used here.

3 Construction of correlation function

Experimentally, the two-particle correlation function $CF(q_{inv})$ is constructed as a ratio of the correlated two-particle distribution from the same event, $N_{same}(q_{inv})$, and the uncorrelated two-particle distribution from mixed events, $N_{mixed}(q_{inv})$:

$$CF(q_{inv}) = \frac{N_{same}(q_{inv})}{N_{mixed}(q_{inv})} = \frac{real\ pairs}{mixed\ pairs}, \tag{2}$$

where $q_{inv}^2 = -(p_1^\mu - p_2^\mu)^2$. In the pair rest frame $q_{inv} = 2k^*$. The technique of event mixing is used to obtain the uncorrelated two-particle distribution. The events are mixed within sub-classes with similar values of the primary vertex position along the beam direction and the multiplicity.

4 Unlike-sign 1D correlation functions

In this analysis, the correlation functions are constructed for 5 centralities and 4 different bins of transverse pair momentum $k_T = (\vec{p_1} + \vec{p_2})_T /2$, where $\vec{p_1}$ and $\vec{p_2}$ are the momenta of the first particle and the second particle, respectively. In Figure 2 there are the STAR preliminary results of K^+K^- correlation functions from Au+Au collisions at $\sqrt{s_{NN}} = 200$ GeV. While at the low q_{inv}, the attractive Coulomb interaction and strong interaction in s-wave can be observed, in the region of $q_{inv} \sim 0.25$GeV/c the strong interaction in p-wave via $\phi(1020)$ resonance in FSI is present. As can be seen, the correlation function is sensitive to the source size. In particular, a strong dependence on collision centrality and on the pair k_T is observed in the resonance region.
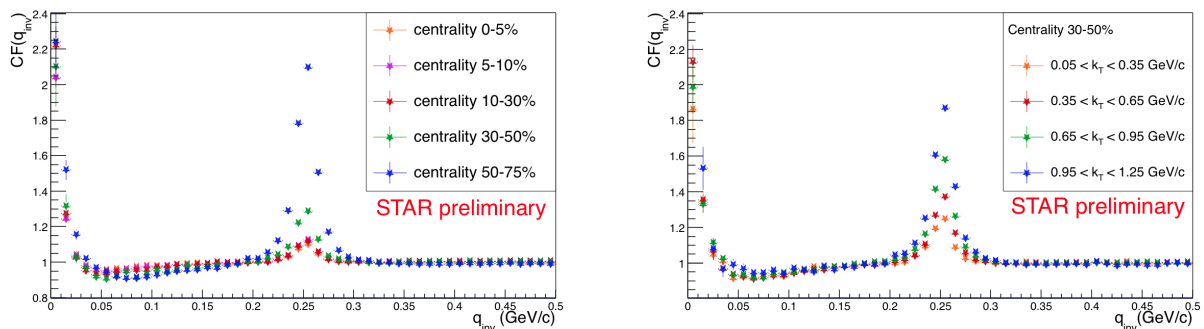
Figure 2. Left: Centrality dependence of one dimensional unlike-sign correlation function from Au+Au collisions at $\sqrt{s_{NN}} = 200$ GeV. Right: k_T dependence of one-dimensional unlike-sign correlation function for centrality 30-50% from Au+Au collisions at $\sqrt{s_{NN}} = 200$ GeV.

Regarding the centrality dependence, where the correlation functions are integrated over all k_T, the height of the ϕ peak decreases significantly with centrality. Similarly a strong dependence is observed as a function of k_T, as shown on right panel of Figure 2 for centrality $30 - 50\%$, mid-peripheral events. The k_T dependence of femtoscopic correlations reflects the dynamics of the system. The observed increase in the correlation strength with the k_T qualitatively agrees with the effects expected

from a system undergoing a transverse expansion where pairs with the larger transverse momentum are emitted from a smaller effective source than the pairs with the smaller k_T [11].

For comparison to the theoretical prediction of [7], additional physical effects have to be taken into account, since they decrease the strength of the measured correlation function. These effects are contained in the so-called correlation strength, the λ parameter. In this analysis, the λ parameter is obtained from fitting an experimental correlation function of like-sign kaons. The effects of momentum resolution, feed-down and residual correlations have not been studied yet.

5 Like-sign 1D correlation functions and fitting

The one-dimensional like-sign correlation functions were constructed by the same method as the unlike-sign correlation functions introduced in the previous sections. Figure 3 shows STAR preliminary results of K^+K^+ and K^-K^- correlation functions from Au+Au collisions at $\sqrt{s_{NN}} = 200$ GeV. As the pairs consist of two identical particles with the same charge, the repulsive Coulomb interaction and Bose-Einstein statistics can be observed at low q_{inv}.
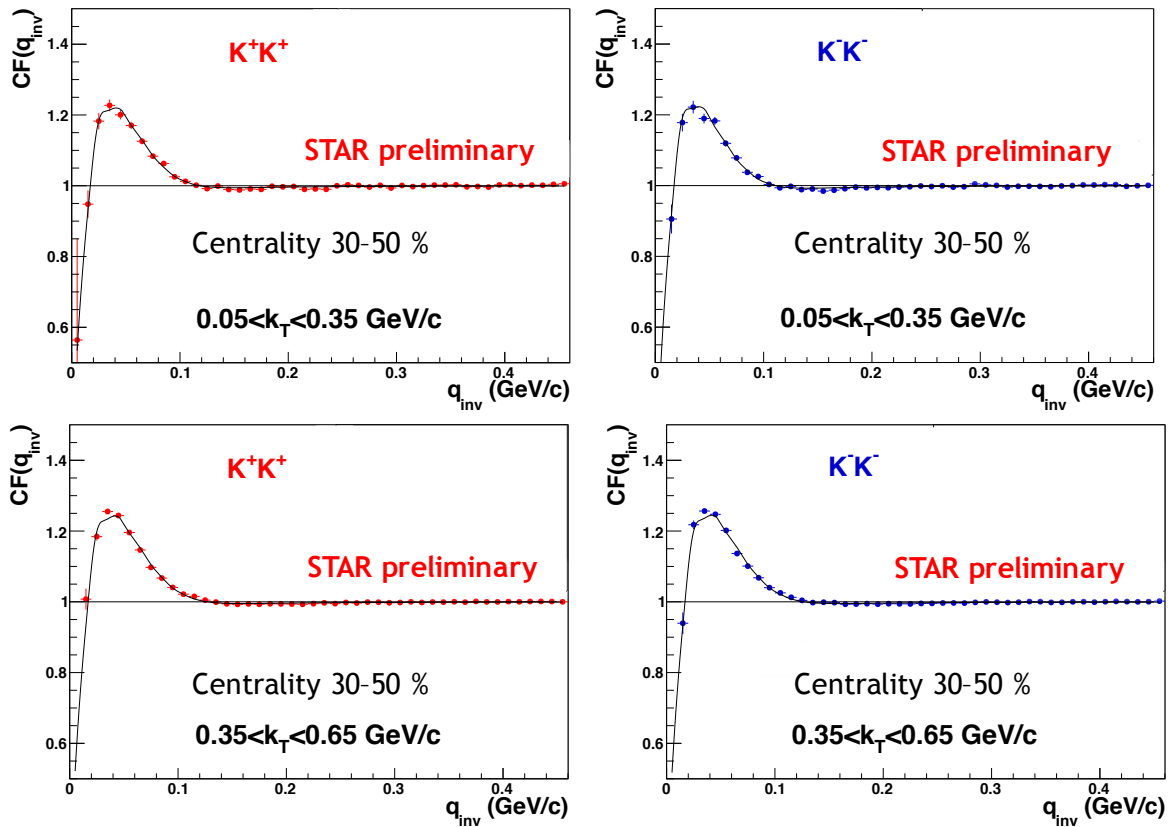
Figure 3. One dimensional K^+K^+ and K^-K^- correlation function from 30-50% central collisions for positive(top) and negative(bottom) kaons for two k_T bins: $0.05 < k_T < 0.35$ GeV/c and $0.35 < k_T < 0.65$ GeV/c. The lines represent the best fits to the data by using the Eq. 3.

The source radii R_{inv} and the λ parameters are obtained from fitting experimental correlation functions with a standard Bowler-Sinyukov form of one dimensional correlation function
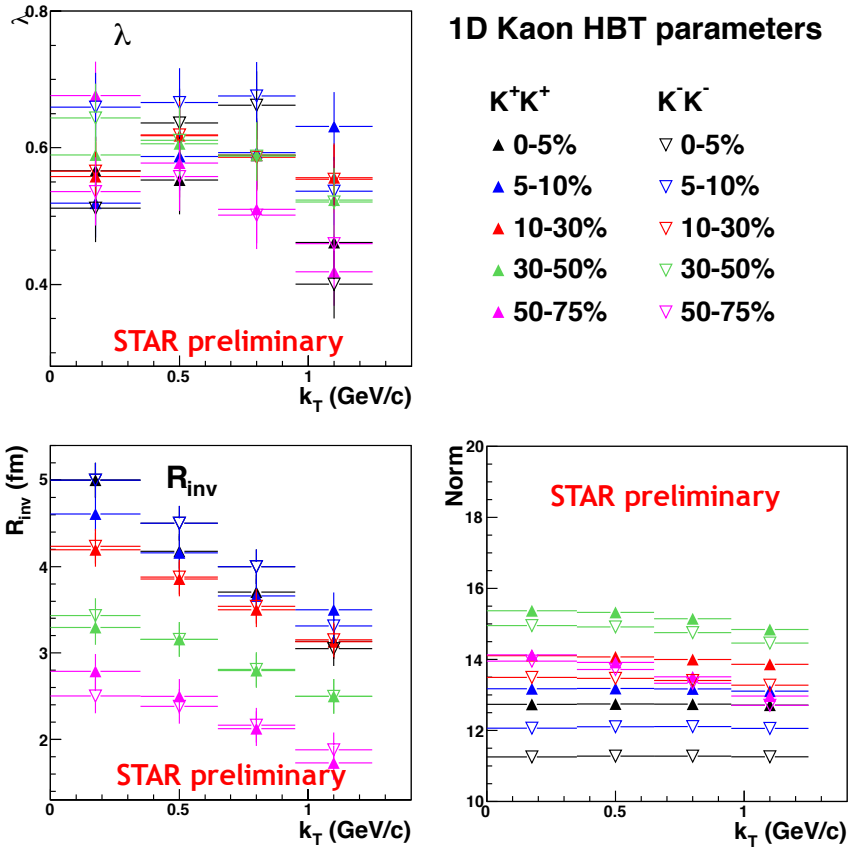
Figure 4. Fit results: λ parameter and source radius R_{inv} as a function of k_T and centrality.

$$CF(q_{inv}) = \left[(1 - \lambda) + \lambda K(q_{inv}) e^{-R_{inv}^2 q_{inv}^2}\right] N, \tag{3}$$

where N is normalization and $K(q_{inv})$ is Coulomb function integrated over source of size R_{inv}. The extracted parameters are shown in Figure 4. As can be seen, the source radii R_{inv} increase with the centrality and decrease with the pair transverse momentum k_T. The errors of fit results are dominated by systematic uncertainties which were estimated by varying the fit ranges. Study of other systematic uncertainties is underway.

6 Comparison of unlike-sign 1D correlation function to Lednicky model

The experimental results of the unlike-sign one-dimensional correlation function can be now compared to the theoretical prediction from Lednicky [7] using a relation:

$$CF(q_{inv}) = \int d^3r S(r, k^*) \left|\psi_{1,2}(r, k^*)\right|^2, \tag{4}$$

where $S(r, k^*)$ is the source function describing emission of two particles at a relative distance r with the relative momentum k^* in the pair rest frame (PRF). The interaction between the two emitted particles is characterized by their wave function $\psi_{1,2}(r, k^*)$.

Similarly, as assumed for eq. (3), the source is described by one-dimensional Gaussian in the PRF with a parameter R_{inv}. Here the individual R_{inv} are those extracted from fitting like-sign correlation

functions (Figure 4). The used FSI model of Lednicky [7] includes the treatment of $\phi(1020)$ resonance in the final state. The model also introduces a generalized form of smoothness approximation which is needed for correct description of the correlation function in the region of the resonance. Since the theoretical function does not include effects contained in the experimental λ parameter, it is scaled for the comparison according to

$$CF = \left(CF^{theor} - 1\right)\lambda + 1, \qquad (5)$$

where λ parameter was obtained from the fit to the like-sign correlation function.

Comparison of unlike-sign one-dimensional correlation functions to model calculations for two collision centralities is shown in Figs. 5 and 6. As can be seen, the model reproduces the overall structure of the observed correlation functions, both at low q_{inv} where the Coulomb and strong interaction in s-wave are present, as well as in the region of $\phi(1020)$ resonance. The agreement in the ϕ region is very good for central collisions, however with decreasing source size the height of the resonance peak is underestimated.
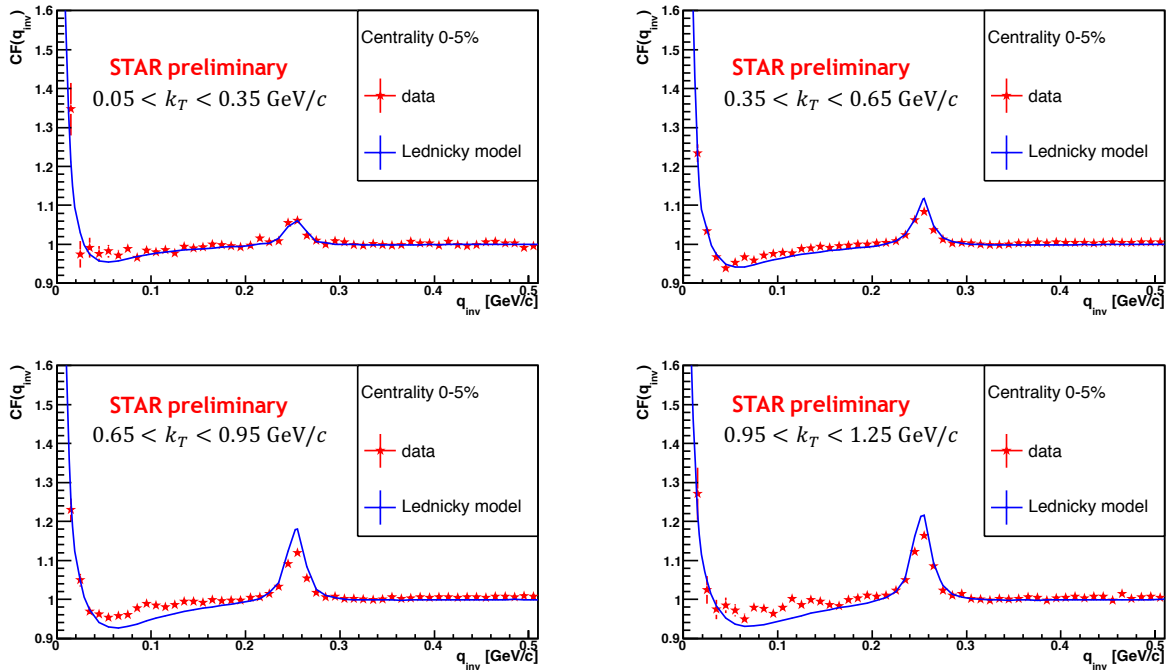
Figure 5. Comparison of experimental K^+K^- correlation functions from Au+Au collisions at $\sqrt{s_{NN}} = 200$ GeV to theoretical calculations for 0-5% centrality for 4 different k_T bins.

7 Summary

In this paper, the preliminary results of a STAR analysis of unlike-sign kaon femtoscopic correlations in Au+Au collisions at $\sqrt{s_{NN}} = 200$ GeV have been presented. The measured K^+K^- correlation function exhibits strong centrality and k_T dependence in the region of $\phi(1020)$ resonance. The obtained correlation function has been compared to a theoretical FSI model with parameters R_{inv}, λ obtained from like-sign correlation functions. The Lednicky FSI model reproduces the correlation function in
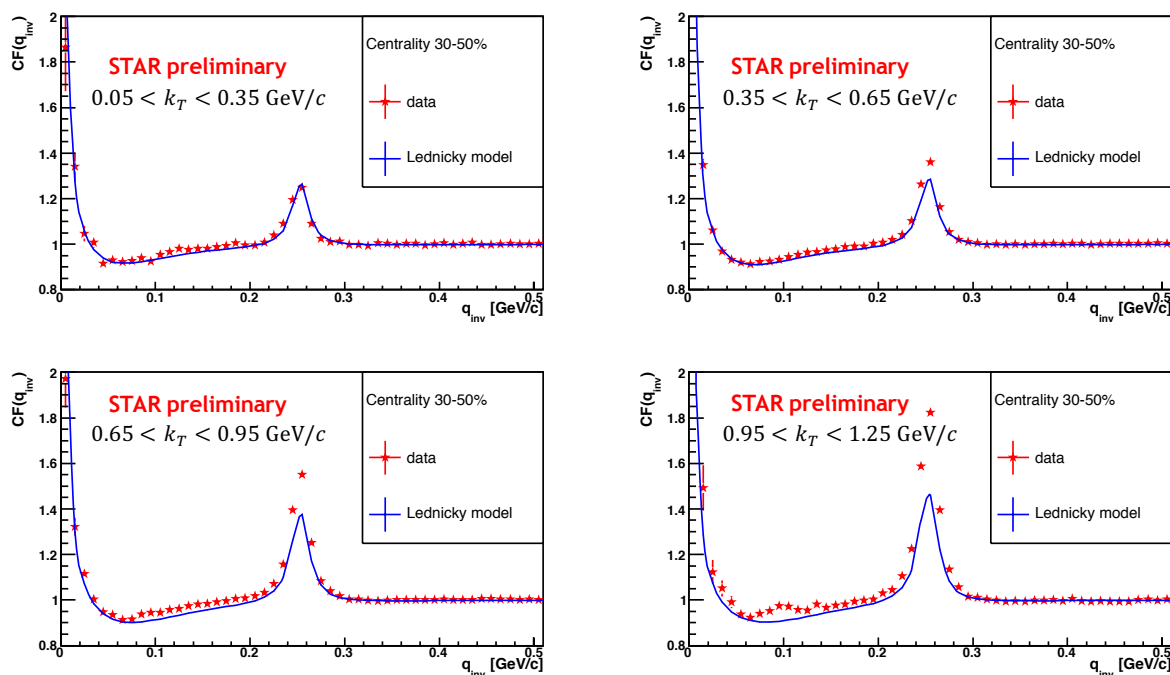
Figure 6. Comparison of experimental K^+K^- correlation functions from Au+Au collisions at $\sqrt{s_{NN}} = 200$ GeV to theoretical calculations for 30-50% centrality for 4 different k_T bins.

central collisions, but underpredicts the strength of correlation in the $\phi(1020)$ region for peripheral collisions.

8 Acknowledgments

References

[1] G. Goldhaber, S. Goldhaber, W.Y. Lee, A. Pais, Phys. Rev. **120**, 300 (1960)

[2] G.I. Kopylov, Phys. Lett. **B50**, 472 (1974)

[3] B.I. Abelev et al. (STAR), Phys. Rev. **C80**, 024905 (2009)

[4] L. Adamczyk et al. (STAR), Phys. Rev. **C88**, 034906 (2013)

[5] L. Adamczyk et al. (STAR), Nature (2015)

[6] L. Adamczyk et al. (STAR), Phys. Rev. Lett. **114**, 022301 (2015)

[7] R. Lednicky, Phys. Part. Nucl. Lett. **8**, 965 (2011)

[8] K.H. Ackermann et al. (STAR), Nucl. Instrum. Meth. **A499**, 624 (2003)

[9] K.H. Ackermann et al. (STAR), Nucl. Phys. **A661**, 681 (1999)

[10] W.J. Llope (STAR), Nucl. Instrum. Meth. **A661**, S110 (2012)

[11] S.V. Akkelin, Yu.M. Sinyukov, Phys. Lett. **B356**, 525 (1995)

Femtoscopy with unlike-sign kaons at STAR in 200 GeV Au+Au collisions*

JINDŘICH LIDRYCH† (FOR THE STAR COLLABORATION)

Faculty of Nuclear Sciences and Physical Engineering
Czech Technical University in Prague
Břehová 7, 115 19 Prague 1

In this paper, a status report of a STAR analysis of unlike-sign kaon femtoscopic correlations in Au+Au collisions at $\sqrt{s_{\mathrm{NN}}} = 200$ GeV is presented. The experimental results are compared to theoretical predictions that include the treatment of $\phi(1020)$ resonance due to final-state interaction.

PACS numbers: PACS numbers come here

1. Introduction

Femtoscopy, measurements of two particle correlations at small relative momenta, is a standard tool to measure the space-time characteristics of the particle emitting source. Nowadays femtoscopic studies span many different particle species and include even non-identical strongly interacting particles [1, 2, 3].

The approach proposed by Lednicky in [4] extends the femtoscopic formalisms to higher relative momenta between the two emitted particles in a system where the final-state interaction (FSI) contains a narrow, near-threshold, resonance. It is predicted that the correlation function will exhibit high sensitivity in the region of the resonance, where the strength of the correlation should scale with the source, r as inverse volume $\sim r^{-3}$. In addition, such measurements are statistically advantageous, since the two-particle spectra fall rapidly at low relative momenta.

The non-identical kaons are a good example of such a system, since they contain a narrow $\phi(1020)$ resonance in the FSI. The $\phi(1020)$ resonance is

characterized by the decay width $\Gamma = 4.3$ MeV and the decay momentum in the rest frame $k^* = 126$ MeV/c.

In this paper there are first presented results on correlation functions of like-sign kaons, which provide information about the source size R_{inv} and the λ parameter. Consequently with these parameters of kaon emission source, the theoretical correlation functions of unlike-sign kaons are calculated by Lednicky model [4] and compared with the experimentally measured ones.

2. Data analysis

The data used for this analysis were collected in Au+Au collisions at $\sqrt{s_{\mathrm{NN}}} = 200$ GeV by the Solenoidal Tracker at RHIC (STAR)[5] in 2011. The most important STAR subdetectors for this analysis are the Time Projection Chamber (TPC) [6] and the Time of Flight (ToF) [7]. The kaons were required to fullfill two main selection criteria. The tracks were required to have $|n\sigma_K| < 3$, where $n\sigma_K$ is a distance from the expected mean $<dE/dx>$ in TPC expressed in terms of standard deviation units σ_K. They were also required to have a signal from the ToF and satisfy a cut on the mass: $0.21 < m^2 < 0.28$ GeV$^2/c^4$.

3. Like-sign 1D correlation function

In this analysis, the correlation functions were constructed for 5 centralities and 4 different bins of transverse pair momentum $k_T = (\vec{p_1} + \vec{p_2})_T /2$. The experimentally measured like-sign correlation function were corrected for misidentification and effects of momentum resolution. The source radii R_{inv} and the λ parameters were obtained from fitting experimental correlation functions with a standard Bowler-Sinyukov form of one dimensional correlation function [8]

$$CF(q_{inv}) = \left[(1-\lambda) + \lambda K\left(q_{inv}\right) e^{-R_{inv}^2 q_{inv}^2} \right] N, \qquad (1)$$

where N is a normalization and $K\left(q_{inv}\right)$ is the Coulomb function integrated over source of size R_{inv}. The correlation function depends on q_{inv} defined as $q_{inv}^2 = -(p_1^\mu - p_2^\mu)^2$, where p_1^μ and p_2^μ are the four-momenta of the first particle and the second particle, respectively. In the pair rest frame $q_{inv} = 2k^*$.

The extracted parameters are shown in Figure 1. As can be seen, the source radii R_{inv} increase with the centrality and decrease with the pair transverse momentum k_T. The errors of fit results are dominated by systematic uncertainties which were estimated by varying the fit ranges. Further study of other systematic uncertainties, such as pair selection cuts, is underway.
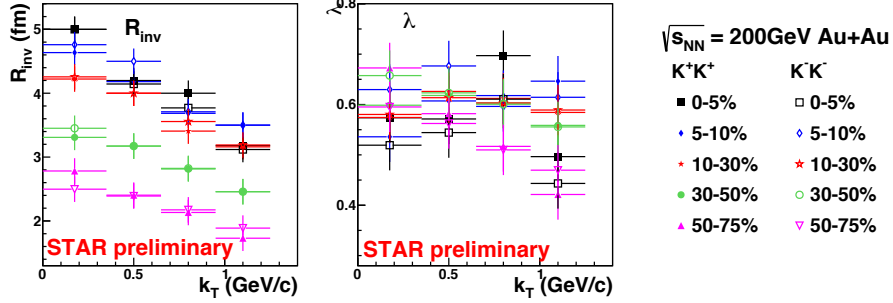
Fig. 1. Fit results of one-dimensional K^+K^+ and K^-K^- correlation functions.

4. Unlike-sign 1D correlation function

Figure 2 shows the STAR preliminary results of K^+K^- correlation functions from Au+Au collisions at $\sqrt{s_{\mathrm{NN}}} = 200$ GeV. While at the low q_{inv}, the attractive Coulomb interaction and strong interaction in s-wave can be observed, in the region of $q_{inv} \sim 0.25\mathrm{GeV}/c$ the strong interaction in p-wave via $\phi(1020)$ resonance is present. As can be seen, the correlation function is sensitive to the source size. In particular, a strong dependence on the collision centrality and on the pair k_T was observed in the resonance region.
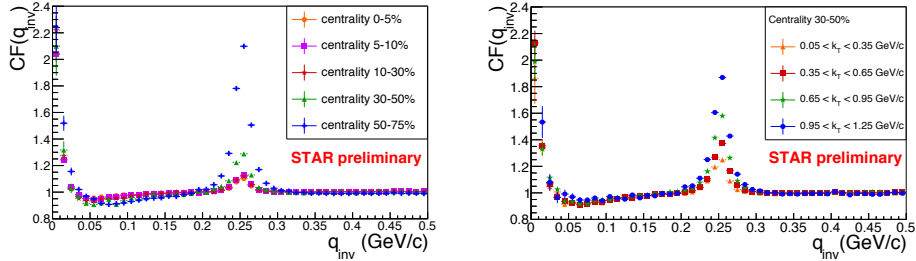
Fig. 2. Left: Centrality dependence of one-dimensional unlike-sign correlation function from Au+Au collisions at $\sqrt{s_{\mathrm{NN}}} = 200$ GeV. Right: k_T dependence of one-dimensional unlike-sign correlation function for centrality 30-50% from Au+Au collisions at $\sqrt{s_{\mathrm{NN}}} = 200$ GeV.

The experimental results of the unlike-sign one-dimensional correlation function were compared to the theoretical prediction from the Lednicky model[4] using a relation:

$$CF(q_{inv}) = \int \mathrm{d}^3 r S(r, k^*) \left| \psi_{1,2}(r, k^*) \right|^2, \qquad (2)$$

where $S(r, k^*)$ is the source function describing emission of two particles at relative distance r with the relative momentum k^* in the pair rest frame (PRF). The interaction between the two emitted particles is characterized by their wave function $\psi_{1,2}(r, k^*)$. The source was parametrized by one-dimensional Gaussian in the pair rest frame with a parameter R_{inv} extracted from fitting like-sign correlation function(Figure 1). The used FSI model of Lednicky [4] includes the treatment of the $\phi(1020)$ resonance in the final state. The model also introduces a generalized form of the smoothness approximation which is needed for correct description of the correlation function in the region of the resonance. Since the theoretical function didn't include effects contained in the experimental λ parameter, it was scaled for the comparison according to $CF = \left(CF^{theor} - 1\right)\lambda + 1$, where λ parameter was also obtained from the fit to the like-sign correlation function. The comparison of the experimental and theoretical calculation is shown in Figure 3.

As can be seen, the model reproduces the overall structure of the observed correlation functions, both at low q_{inv} where the Coulomb and strong interaction in s-wave are present, as well as in the region of $\phi(1020)$ resonance. The agreement in the ϕ region is very good for central collisions, however with decreasing source size the height of the resonance peak is underestimated.

5. Summary

In this paper, preliminary results of STAR analysis of unlike-sign kaon femtoscopic correlations in Au+Au collisions at $\sqrt{s_{\mathrm{NN}}} = 200$ GeV have been presented. The measured K^+K^- correlation function exhibits strong centrality and k_T dependence in the region of $\phi(1020)$ resonance. The obtained correlation function has been compared to a theoretical FSI model with parameters R_{inv}, λ obtained from like-sign correlation functions. The Lednicky FSI model reproduces the correlation function in central collisions, but underpredicts the strength of correlation in the $\phi(1020)$ region for peripheral collisions.

REFERENCES

[1] L. Adamczyk et al. (STAR), Phys. Rev. **C88**, 034906 (2013)

[2] L. Adamczyk et al. (STAR), Nature (2015)

[3] L. Adamczyk et al. (STAR), Phys. Rev. Lett. **114**, 022301 (2015)

[4] R. Lednicky, Phys. Part. Nucl. Lett. **8**, 965 (2011)

[5] K.H. Ackermann et al. (STAR), Nucl. Instrum. Meth. **A499**, 624 (2003)
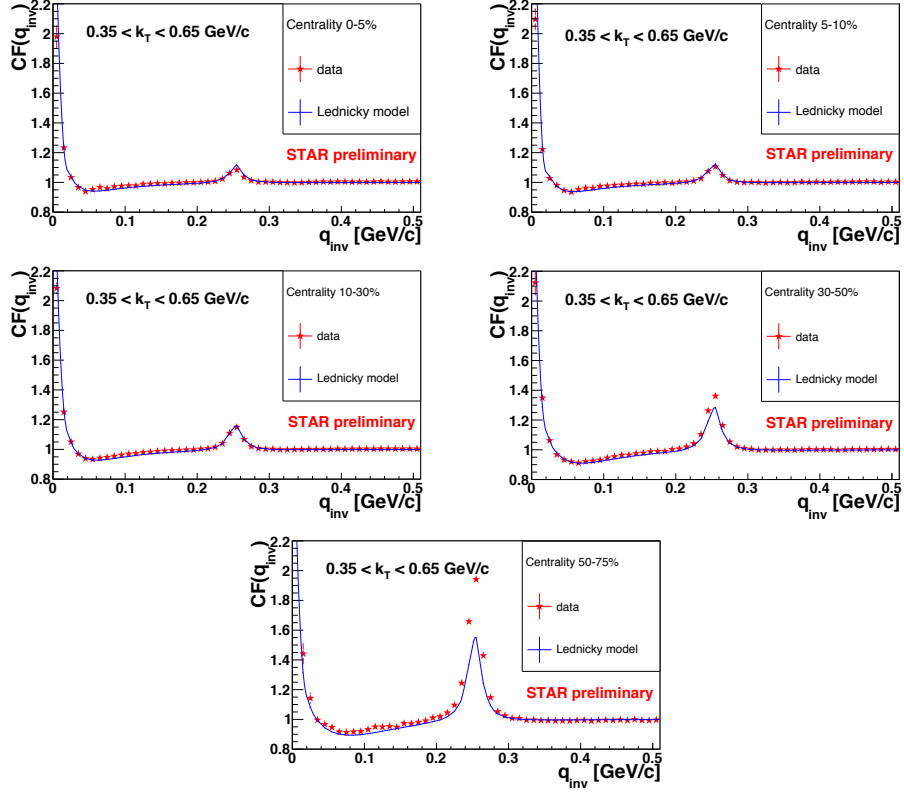
Fig. 3. Comparison of experimental K^+K^- correlation functions from Au+Au collisions at $\sqrt{s_{NN}} = 200$ GeV to theoretical calculations for 5 different centralities for $0.35 < k_T < 0.65$ GeV/c.

[6] K.H. Ackermann et al. (STAR), Nucl. Phys. **A661**, 681 (1999)

[7] W.J. Llope (STAR), Nucl. Instrum. Meth. **A661**, S110 (2012)

[8] M.G. Bowler, Phys. Lett **B270**, 69 (1991)

BIBLIOGRAPHY

[1] David Griffiths. *Introduction to Elementary Particles*. Wiley-VCH Verlag GmbH, 2008.

[2] Roel Aaij et al. Observation of $J/\psi p$ resonances consistent with pentaquark states in $\Lambda\_b^0 \rightarrow J/\psi K^- p$ decays. *Phys. Rev. Lett.*, 115:072001, 2015.

[3] V. M. Abazov et al. Observation of a new $B_s^0 \pi^\pm$ state. 2016.

[4] Serguei Chatrchyan et al. Observation of a new boson at a mass of 125 GeV with the CMS experiment at the LHC. *Phys. Lett.*, B716:30–61, 2012.

[5] Georges Aad et al. Observation of a new particle in the search for the Standard Model Higgs boson with the ATLAS detector at the LHC. *Phys. Lett.*, B716:1–29, 2012.

[6] Wikimedia Commons. Standard model. `http://upload.wikimedia.org/wikipedia/commons/0/00/Standard_Model_of_Elementary_Particles.svg`, [Online 6-March-2014].

[7] David J. Gross and Frank Wilczek. Ultraviolet behavior of non-abelian gauge theories. *Phys. Rev. Lett.*, 30:1343–1346, Jun 1973.

[8] Vardan Khachatryan et al. Measurement of the inclusive 3-jet production differential cross section in proton–proton collisions at 7 TeV and determination of the strong coupling constant in the TeV range. *Eur. Phys. J.*, C75(5):186, 2015.

[9] F. Karsch, E. Laermann, and A. Peikert. Quark mass and flavor dependence of the QCD phase transition. *Nucl.Phys.*, B605:579–599, 2001.

[10] Yasuo Miake Kohsuke Yagi, Tetsuo Hatsuda. *Quark-Gluon Plasma: From Big Bang to Little Bang*. Cambridge University Press, 2008.

[11] J. D. Bjorken. Highly Relativistic Nucleus-Nucleus Collisions: The Central Rapidity Region. *Phys. Rev.*, D27:140–151, 1983.

[12] BNL. Rhic accelerators. `http://www.bnl.gov/rhic/complex.asp`, [Online 6-March-2014].

[13] STAR Collaboration. Studying the phase diagram of qcd matter at rhic. *drupal.star.bnl.gov*, 2014.

[14] Betty Abelev et al. Centrality determination of Pb-Pb collisions at $\sqrt{s_{NN}} = 2.76$ TeV with ALICE. *Phys. Rev.*, C88(4):044909, 2013.

[15] Michael L. Miller, Klaus Reygers, Stephen J. Sanders, and Peter Steinberg. Glauber modeling in high energy nuclear collisions. *Ann. Rev. Nucl. Part. Sci.*, 57:205–243, 2007.

[16] Michael Kliemant, Raghunath Sahoo, Tim Schuster, and Reinhard Stock. Global Properties of Nucleus-Nucleus Collisions. *Lect. Notes Phys.*, 785:23–103, 2010.

[17] Mercedes Lopez Noriega. *Pion Interferometry in AuAu Collisions at a Center of Mass Energy per Nucleon of 200 GeV*. PhD thesis, The Ohio State University, 2004.

[18] Michal Sumbera. Results from STAR Beam Energy Scan Program. *Acta Phys.Polon.Supp.*, 6:429–436, 2013.

[19] Stephen Horvat. Measurement of hadron suppression and study of its connection with vanishing v_3 at low $\sqrt{s_{\mathrm{NN}}}$ in Au+Au collisions with STAR. 2016.

[20] J. W. Cronin, Henry J. Frisch, M. J. Shochet, J. P. Boymond, R. Mermod, P. A. Piroue, and Richard L. Sumner. Production of hadrons with large transverse momentum at 200, 300, and 400 GeV. *Phys. Rev.*, D11:3105–3123, 1975.

[21] B. I. Abelev et al. Measurements of phi meson production in relativistic heavy-ion collisions at RHIC. *Phys. Rev.*, C79:064903, 2009.

[22] Reinhard Stock. Relativistic Nucleus-Nucleus Collisions and the QCD Matter Phase Diagram. 2008.

[23] L. Adamczyk et al. Elliptic flow of identified hadrons in Au+Au collisions at $\sqrt{s_{NN}} = 7.7$-62.4 GeV. *Phys. Rev.*, C88:014902, 2013.

[24] C.Y. Wong. *Introduction to high-energy heavy-ion collsions*. World Scientific Pub Co, 1990.

[25] Agnes Mocsy. Potential Models for Quarkonia. *Eur. Phys. J.*, C61:705–710, 2009.

[26] Brookhaven National Laboratory. Laboratory, brookhaven national. `http://www.star.bnl.gov`, [Online 10-March-2014].

[27] Peter Jacobs and Xin-Nian Wang. Matter in extremis: Ultrarelativistic nuclear collisions at RHIC. *Prog.Part.Nucl.Phys.*, 54:443–534, 2005.

[28] Wolfram Fischer. The rhic run overview. `http://www.agsrhichome.bnl.gov/RHIC/Runs/`, [Online 4-July-2014].

[29] K.H. Ackermann et al. STAR detector overview. *Nucl.Instrum.Meth.*, A499:624–632, 2003.

[30] Spiros Margetis. Heavy Flavor Tracker (HFT): The new silicon vertex detector for the STAR experiment at RHIC. *Nucl.Phys.Proc.Suppl.*, 210-211:227–230, 2011.

[31] A. Shabetai. The hft, a heavy flavor tracker for star. *The European Physical Journal C*, 49(1):169–175, 2007.

[32] M. Anderson, J. Berkovitz, W. Betts, R. Bossingham, F. Bieser, et al. The Star time projection chamber: A Unique tool for studying high multiplicity events at RHIC. *Nucl.Instrum.Meth.*, A499:659–678, 2003.

[33] L. Kotchenda, S. Kozlov, P. Kravtsov, A. Markov, M. Strikhanov, B. Stringfellow, V. Trofimov, R. Wells, and H. Wieman. {STAR} {TPC} gas system. *Nuclear Instruments and Methods in Physics Research Section A: Accelerators, Spectrometers, Detectors and Associated Equipment*, 499(2–3):703 – 712, 2003. The Relativistic Heavy Ion Collider Project: {RHIC} and its Detectors.

[34] H. Bichsel. A method to improve tracking and particle identification in TPCs and silicon detectors. *Nucl.Instrum.Meth.*, A562:154–197, 2006.

[35] David Tlustý. *A Study of Open Charm Production in p+p Collisions at STAR*. PhD thesis, Czech Technical University in Prague, 2014.

[36] F.S. Bieser, H.J. Crawford, J. Engelage, G. Eppley, L.C. Greiner, et al. The STAR trigger. *Nucl.Instrum.Meth.*, A499:766–777, 2003.

[37] W. J. Llope et al. The STAR Vertex Position Detector. *Nucl. Instrum. Meth.*, A759:23–28, 2014.

[38] A. Accardi, J.L. Albacete, M. Anselmino, N. Armesto, E.C. Aschenauer, et al. Electron Ion Collider: The Next QCD Frontier - Understanding the glue that binds us all. 2012.

[39] R. Hanbury Brown and R. Q. Twiss. Correlation between Photons in two Coherent Beams of Light. *Nature*, 177:27–29, 1956.

[40] Robert Hanbury; Richard Q. Twiss Brown. A test of new type of stellar interferometer on sirius. *Nature*, 178(4541):1046–1048, 1956.

[41] Gerson Goldhaber". Influence of bose-einstein statistics on the antiproton-proton annihilation process. *Physical Review*, 120(1):300–312, 1960.

[42] G. I. Kopylov. Like particle correlations as a tool to study the multiple production mechanism. *Phys. Lett.*, B50:472–474, 1974.

[43] E. Fermi. An attempt of a theory of beta radiation. 1. *Z. Phys.*, 88:161–177, 1934.

[44] Michael Annan Lisa, Scott Pratt, Ron Soltz, and Urs Wiedemann. Femtoscopy in relativistic heavy ion collisions. *Ann.Rev.Nucl.Part.Sci.*, 55:357–402, 2005.

[45] R. Lednicky. Femtoscopic correlations and final state resonance formation. *Phys. Part. Nucl. Lett.*, 8:965–968, 2011.

[46] Richard Lednicky. Finite-size effects on two-particle production in continuous and discrete spectrum. *Phys. Part. Nucl.*, 40:307–352, 2009.

[47] L. Adamczyk et al. Freeze-out dynamics via charged kaon femtoscopy in sqrt(sNN) = 200 GeV central Au + Au collisions. *Phys. Rev.*, C88:034906, 02 2013.

[48] Ulrich W. Heinz. How to extract physics from HBT radius parameters. *Nucl.Phys.*, A610:264C–277C, 1996.

[49] Y.F. Wu, Ulrich W. Heinz, B. Tomasik, and U.A. Wiedemann. Yano-Koonin-Podgoretskii parametrization of the HBT correlator: A Numerical study. *Eur.Phys.J.*, C1:599–617, 1998.

[50] R. Lednicky, V.L. Lyuboshits, B. Erazmus, and D. Nouais. How to measure which sort of particles was emitted earlier and which later. *Phys.Lett.*, B373:30–34, 1996.

[51] Adam Kisiel. Nonidentical particle correlations in 130-A-GeV and 200-A-GeV collisions at STAR. *J.Phys.*, G30:S1059–S1064, 2004.

[52] J. Adams et al. Pion kaon correlations in Au+Au collisions at s(NN)**1/2 = 130-GeV. *Phys.Rev.Lett.*, 91:262302, 2003.

[53] I.P. Lokhtin, L.V. Malinina, S.V. Petrushanko, A.M. Snigirev, I. Arsene, et al. Heavy ion event generator HYDJET++ (HYDrodynamics plus JETs). *Comput.Phys.Commun.*, 180:779–799, 2009.

[54] Mikolaj Chojnacki, Adam Kisiel, Wojciech Florkowski, and Wojciech Broniowski. THERMINA-TOR 2: THERMal heavy IoN generATOR 2. *Comput. Phys. Commun.*, 183:746–773, 2012.

[55] Fabrice Retiere and Michael Annan Lisa. Observable implications of geometrical and dynamical aspects of freeze out in heavy ion collisions. *Phys.Rev.*, C70:044907, 2004.

[56] A. Bamberger et al. Probing the Space-time Geometry of Ultrarelativistic Heavy Ion Collisions. *Phys. Lett.*, B203:320–326, 1988.

[57] Michael Annan Lisa and Scott Pratt. Femtoscopically Probing the Freeze-out Configuration in Heavy Ion Collisions. 2008.

[58] Dirk H. Rischke and Miklos Gyulassy. The Time delay signature of quark - gluon plasma formation in relativistic nuclear collisions. *Nucl.Phys.*, A608:479–512, 1996.

[59] L. Adamczyk et al. Beam-energy-dependent two-pion interferometry and the freeze-out eccentric-ity of pions measured in heavy ion collisions at the STAR detector. *Phys. Rev.*, C92(1):014904, 2015.

[60] Roy A. Lacey. Indications for a Critical End Point in the Phase Diagram for Hot and Dense Nuclear Matter. *Phys. Rev. Lett.*, 114(14):142301, 2015.

[61] L. Adamczyk et al. Measurement of Interaction between Antiprotons. *Nature*, 527:345–348, 2015.

[62] J. Pochodzalla et al. Two-particle correlations at small relative momenta for ^{40}induced reactions on ^{197}Au at E/A =60 mev. *Phys. Rev. C*, 35:1695–1719, May 1987.

[63] Mike Lisa. Femtoscopy and hadrochemistry. In *9th Workshop on Particle Correlations and Femtoscopy*, 2013.

[64] Byron K. Jennings, David H. Boal, and Julian C. Shillcock. Two-particle correlation functions in the thermal model and nuclear interferometry descriptions. *Phys. Rev.*, C33:1303–1306, 1986.

[65] S. V. Afanasiev et al. Bose–Einstein correlations of charged kaons in central Pb+Pb collisions at E_{beam} =158 GeV per nucleon. *Phys. Lett.*, B557:157–166, 2003.

[66] Petr Chaloupka. Femtoscopy with multi-strange baryons at RHIC. *Phys.Part.Nucl.Lett.*, 8:973–976, 2011.

[67] P. Chaloupka, M. Sumbera, and L.V. Malinina. pi Xi correlations: Model comparison and Xi*(1530) puzzle. *Acta Phys.Polon.*, B40:1185–1192, 2009.

[68] Z. Chajecki, T.D. Gutierrez, M.A. Lisa, and M. Lopez-Noriega. AA versus PP (and dA): A Puzzling scaling in NBT and RHIC. 2005.

[69] Petr Chaloupka. *Femtoscopy with multi-strange baryons at RHIC*. PhD thesis, Charles University in Prague, 2010.

[70] Christopher Daniel Anson. *Energy dependet Hanbury Brown - Twiss interferometry and the freeze-out eccentricity of heavy ion collisions at STAR.* PhD thesis, The Ohio State University, 2014.

[71] Adam Kisiel, editor. *CorrFit: a program to fit arbitrary two-particle correlation functions*, volume 49(Supplement 2). Nukleonika, 2004.

[72] M. G. Bowler. Coulomb corrections to Bose-Einstein correlations have been greatly exaggerated. *Phys. Lett.*, B270:69–74, 1991.

[73] L. Ahle et al. System, centrality, and transverse mass dependence of two-pion correlation radii in heavy ion collisions at $11.6a$ and $14.6a$GeV$/c$. *Phys. Rev. C*, 66:054906, Nov 2002.

[74] Hanna Zbroszczyk. *Studies of Baryon-Baryon Correlations in Relativistic Nuclear Collisions Registered at the STAR Experiment.* PhD thesis, Warsaw University of Technology, 2008.

[75] K. Nakamura et al. Review of particle physics. *J.Phys.*, G37:075021, 2010.

[76] A. Adare et al. Systematic study of charged-pion and kaon femtoscopy in Au + Au collisions at $\sqrt{s_{NN}}$=200 GeV. *Phys. Rev.*, C92(3):034914, 2015.

[77] S. S. Adler et al. Identified charged particle spectra and yields in Au+Au collisions at S(NN)**1/2 = 200-GeV. *Phys. Rev.*, C69:034909, 2004.

[78] J. Adams et al. Pion interferometry in Au+Au collisions at S(NN)**(1/2) = 200-GeV. *Phys.Rev.*, C71:044906, 2005.

[79] J. Beringer et al. Review of particle physics*. *Phys. Rev. D*, 86:010001, Jul 2012.

[80] Hanna Zbroszczyk. Two-particle correlations using therminator model for bes program. presentation on ICNFP 2015.

[81] L. Adamczyk et al. $\Lambda\Lambda$ Correlation Function in Au+Au collisions at $\sqrt{s_{NN}}$ = 200 GeV. *Phys. Rev. Lett.*, 114(2):022301, 2015.

[82] Fu-Quiang Wang. Residual correlation in two proton interferometry from Lambda proton strong interactions. *Phys.Rev.*, C60:067901, 1999.

[83] Jaroslav Adam et al. One-dimensional pion, kaon, and proton femtoscopy in Pb-Pb collisions at $\sqrt{s_{NN}}$ =2.76 TeV. *Phys. Rev.*, C92(5):054908, 2015.